Double Helicity Asymmetry in Particle Cluster Production from Polarized p+p Collisions at $\sqrt{s} = 200$ GeV

Kenichi Nakano

Thesis submitted to the Department of Physics in partial fulfillment of the requirements for the degree of Doctor of Science at Tokyo Institute of Technology

February, 2008

Abstract

In this thesis a new method and result for the study of gluon spin in the proton using particle clusters from jets in proton-proton collisions are presented. The proton spin is composed of the spins and the orbital angular momenta of quarks and gluons in the proton. The understanding of the proton spin structure is one of the most important subjects in the particle and hadron physics. In 1988 the EMC experiment revealed that the contribution of the quark spin ($1/2\Delta\Sigma$) to the proton spin is $(12 \pm 9 \pm 14)\%$. Many deep inelastic lepton scattering (DIS) experiments have been carried out to precisely measure the $1/2\Delta\Sigma$, and recent analyses conclude that it is only 30%.

High-energy proton-proton collision is also an important method as gluon-gluon scattering, gluon-quark scattering etc. take place. I started a new method to study the gluon spin in the proton using particle clusters from jets. I developed this method and analyzed the data for the first time. This thesis reports the double helicity asymmetry (A_{LL}) of particle clusters from jet production process in longitudinally polarized proton-proton collisions at $\sqrt{s} = 200$ GeV. A_{LL} is defined as the difference in cross section between two beam-helicity patterns; the same ($++$ or $--$) and the opposite ($+-$ or $-+$). It is sensitive to the gluon spin in the proton (Δg). The Δg can have a large contribution to the proton spin.

The Relativistic Heavy Ion Collider (RHIC) is the first collider capable of polarized proton-proton collisions. In 2005 the PHENIX experiment at RHIC accumulated, with a high-energy ($\gtrsim 1.4$ GeV) photon trigger, collision data about 3.8 pb^{-1} in integrated luminosity with average beam polarizations $\langle P \rangle = 49\%$. The PHENIX Central Arm consists of two arms which are positioned almost back-to-back on their azimuth and each of which covers a pseudo-rapidity $|\eta| < 0.35$ and 90-degree azimuthal angle. I performed an energy calibration of every module of electromagnetic calorimeters (EMCal) in the Central Arm and an development of the high-energy-photon trigger. Photons and charged particles in jets were measured with the Central Arm. Measured particles were clustered with a seed-cone algorithm to obtain the sum of p_T of the particles in a cluster ($p_T^{\rm cone}$). The relation between $p_T^{\rm jet}$ and $p_T^{\rm cone}$ was evaluated with the PYTHIA event generator and the GEANT detector simulator. To confirm the reproducibility of the simulation, event structures and cone production rate were measured.

The A_{LL} of particle clusters was measured at $4 < p_T^{\rm cone} < 12$ GeV/c and a mid-rapidity $|\eta| < 0.35$. The main systematic errors are the p_T scale uncertainty of 10% and the beam polarization uncertainty of 9.4%. Particle clusters at the measured $p_T^{\rm cone}$ range are mainly produced from gluons with the momentum fraction $0.02 < x < 0.3$ according to the PYTHIA simulation. The measured A_{LL} was compared with the predictions that assumed various $\Delta g(x)$ distributions. The present result imposed the limit $-1.1 < \int_{0.02}^{0.3} dx \Delta g^{GRSV}(x, Q^2 = 1) < 0.4$ at 2σ level or $\int_{0.02}^{0.3} dx \Delta g^{GRSV}(x, Q^2 = 1) < 0.5$ at 3σ level, and thus excluded the large-Δg scenarios in the GRSV parameterization.

Contents

1 Introduction **4**

2 Physics of the proton structure and jet production **7**
2.1 Proton structure 7
2.1.1 Quark-parton model and parton distribution function . 7
2.1.2 Polarized parton distribution function 10
2.1.3 Sum rules and proton spin problem 14
2.1.4 $\Delta g(x)$ measurement with DIS 20
2.1.5 $\Delta g(x)$ measurement with SIDIS 24
2.1.6 $\Delta g(x)$ measurement with proton-proton collisions . . . 24
2.2 Jet production in proton-proton collisions 31
2.2.1 Jet cone and clustering procedure 31
2.2.2 Cross section 36
2.2.3 Double helicity asymmetry 37

3 Experimental Setup **41**
3.1 Accelerator 41
3.1.1 Polarized proton source 41
3.1.2 RHIC 44
3.1.3 Beam luminosity 44
3.1.4 Beam polarization 45
3.2 PHENIX detector overview 48
3.3 Beam-beam counter (BBC) 53
3.4 Zero degree calorimeter (ZDC) 54
3.5 Electromagnetic calorimeter (EMCal) 54
3.6 Charged particle tracking 60
3.7 Data acquisition (DAQ) system 65
3.7.1 DAQ outline 65
3.7.2 Triggers 68
3.8 Simulation settings 72
3.8.1 PYTHIA event generator 72

3.8.2 Underlying event and Multi-Parton Interaction 72
3.8.3 GEANT detector simulator 73

4 Analysis Methods **75**
4.1 Outline 75
4.2 Run selection 76
4.3 Quality assurance and calibration of detectors 76
4.3.1 EMCal 76
4.3.2 Tracking detectors 83
4.3.3 Run dependence of the summed transverse momentum 93
4.4 Particle Clustering with Cone Method 93
4.4.1 Particle selection 93
4.4.2 Cluster finding algorithm 96
4.4.3 Remaining hadron contribution 97
4.4.4 $p_T^{\rm cone}$ distribution 97
4.5 Simulation Study 97
4.5.1 Relating cone to jet 97
4.5.2 Bias of cone measurement 99
4.6 Event structure 103
4.6.1 Multiplicity 103
4.6.2 Transverse momentum density 103
4.6.3 Thrust distribution in PHENIX Central Arm 103
4.7 Cone production rate 105
4.7.1 Evaluation method 105
4.7.2 Luminosity in measurement 107
4.7.3 Trigger efficiency and acceptance correction in simulation 108
4.7.4 Systematic error estimation 109
4.8 Double helicity asymmetry 111
4.8.1 Evaluation method 111
4.8.2 Check on systematic errors 115
4.8.3 Calculation of predicted asymmetry 115
4.9 Statistical overlap with π^0 measurement 123

5 Results and discussions **125**
5.1 Event structure 125
5.1.1 Multiplicity 125
5.1.2 Transverse momentum density 125
5.1.3 Thrust distribution in PHENIX Central Arm 129
5.2 Cone production rate 129
5.3 Single helicity asymmetry A_L 133
5.4 Double helicity asymmetry A_{LL} 133

5.5 Constraint on Δg 136
5.5.1 Probed x_{gluon} range 136
5.5.2 χ^2 between measurement and calculation 136
5.5.3 Comparison with SIDIS results 139
5.5.4 Systematic uncertainty on theory calculation 139

6 Conclusion **143**

Chapter 1

Introduction

The motivation of this research is to understand the spin structure of the proton, particularly the polarized gluon distribution function

$$\Delta g(x) \equiv g^+(x) - g^-(x) \tag{1.1}$$

where x is the Bjorken scaling variable and $g^{+(-)}(x)$ means the probability of finding gluons with the spin parallel (anti-parallel) to the proton spin and with the momentum fraction x of the proton momentum. The integral $\Delta g = \int_0^1 dx \Delta g(x)$ represents the total spin of gluons in the proton.

The contribution of the quark spin to the proton spin

$$\frac{1}{2}\Delta\Sigma \equiv \frac{1}{2}\sum_f \int_0^1 dx \Delta q_f(x) \equiv \frac{1}{2}\sum_f \int_0^1 dx (q_f^+(x) - q_f^-(x)) \tag{1.2}$$

was measured by the EMC experiment at CERN in 1988, and was revealed to be only $(12 \pm 9 \pm 14)\%$[1][2]. The EMC experiment extended the x range down to very small region, which enabled a precision measurement compared to the earlier SLAC experiments[3]. In a theoretical interpretation[4] proposed just after the EMC experiment, the apparent smallness of $\frac{1}{2}\Delta\Sigma$ was attributed to large gluon spin polarization Δg ($\sim$4) in the proton due to the triangle anomaly. However, it then means that the large Δg needs to be mostly compensated by a large orbital angular momentum to make the proton spin 1/2. After the EMC experiment many deep inelastic scattering (DIS) experiments have measured Δq even more precisely. The recent result of the HERMES analysis[5] reported that

$$\Delta\Sigma = 0.330 \pm 0.011(\text{theo.}) \pm 0.025(\text{exp.}) \pm 0.028(\text{evol.}) \tag{1.3}$$

at $Q^2 \sim 5$ GeV^2, which is only $\sim$30% of the proton spin. It indicates that the large amount of proton spin should be carried by the remaining components;

the spin of gluons (Δg) and/or the orbital angular momenta of quarks and gluons ($L_{q,g}$).

$$\frac{1}{2}_{proton} = \frac{1}{2}\sum_{f} \Delta q_f + \Delta g + L_q + L_g \tag{1.4}$$

The understanding of the proton spin structure is one of the most important subjects in the particle and hadron physics of today.

DIS with lepton beams are mainly sensitive to the quark distribution $\Delta q_f(x)$ because of the electromagnetic interaction ($lq \rightarrow lq$). They are partly sensitive to the gluon distribution $\Delta g(x)$ via the Q^2-depending variation of the $\Delta q_f(x)$. Therefore the gluon contribution Δg has been obtained from DIS data as well. Several analyses have estimated the Δg to be non-zero, ~ 0.3 at $Q^2 \sim 1$ GeV^2, but zero or much larger values are still allowed within the uncertainty of the analyses.

The longitudinally-polarized proton-proton collision is suited for the measurement of the Δg because gluon-involved scatterings, such as $qg \rightarrow qg$ or $gg \rightarrow gg$, dominate in the cross section at high energy. The double helicity asymmetry (A_{LL}), which is the asymmetry in cross section between two beam helicity patterns

$$A_{LL} \equiv \frac{\sigma_{++} - \sigma_{+-}}{\sigma_{++} + \sigma_{+-}}, \tag{1.5}$$

is measured because many systematic errors cancel out in A_{LL} and thus a high precision can be achieved. In a gluon-gluon s-channel scattering ($gg \rightarrow g^* \rightarrow gg$), for example, the spins of two initial-state gluons have to be anti-parallel with each other to make a valid spin ($S_z = 0$) of the virtual gluon g^*. Such spin conservation, or helicity conservation in other processes, makes spin-dependent asymmetry in gluon-gluon scattering cross section. This asymmetry selects one spin state (parallel or anti-parallel to the proton spin) of gluons in polarized proton, and thus the spin-dependent distribution can be extracted from polarized proton-proton collisions.

The PHENIX experiment is being carried out using the Relativistic Heavy Ion Collider (RHIC) at Brookhaven National Laboratory. One of the goals of the PHENIX experiment is the determination of $\Delta g(x)$. The PHENIX experiment mainly focuses on single-particle productions, and results on π^0 production measurement have been published[6]. This thesis reports a measurement of jet production process, which is measured as a cluster of particles that have collinear momenta. These two measurements have different types of systematic uncertainties and thus one can provide a systematic check for the other. Jet measurement can reach larger statistics at high-p_T region and have smaller ambiguities in the treatment of the jet fragmentation process than single particle measurements. Subprocess fractions of gg, qg, $q\bar{q}$

scatterings etc. are different for π^0 inclusive measurement and jet (particle cluster) measurement. Jet measurement is in fact more sensitive to qg scattering which we like to detect. The reason is that a particle cluster has a wider transverse distribution around jet axis when it is generated from gluon. When it is generated from quarks it is narrower. As a result, the particle cluster from quark is enhanced when measured with a finite cone region. The fraction of qg scattering is larger than gg scattering in wide p_T range in the measurement of particle cluster. This is why I started and developed this new method. The analysis technique and the result presented in this thesis open a new possibility for proton spin studies in proton-proton collisions.

In Chapter 2, major topics of the proton spin structure and jet production are introduced. In Chapter 3, experimental setups including the RHIC accelerator and the PHENIX detector are explained. In Chapter 4, analysis methods such as data selections, simulation studies and A_{LL} measurement are described. In Chapter 5, results and discussions of this measurement are shown.

Chapter 2

Physics of the proton structure and jet production

2.1 Proton structure

2.1.1 Quark-parton model and parton distribution function

The structure of proton has been investigated with lepton-proton deep inelastic scattering (DIS),

$$e(k) + p(P) \rightarrow e(k') + X \tag{2.1}$$

as schematically shown in Fig. 2.1. The kinematic variables listed in Tab. 2.1 are commonly used. The cross section for lepton-proton DIS can be expressed with the proton structure function, $F_1(x, Q^2)$ and $F_2(x, Q^2)$, in laboratory

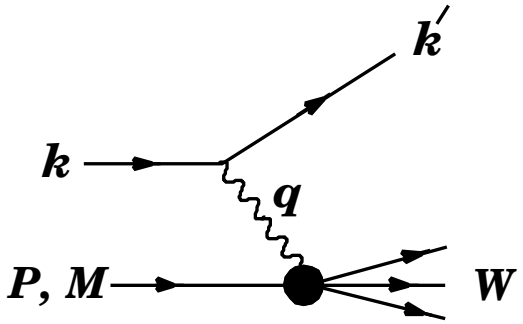

Figure 2.1: Schematic drawing of DIS.

Table 2.1: Kinematic variables in DIS.

$k = (E, \boldsymbol{k})$, $k' = (E', \boldsymbol{k}')$	4-momenta of the initial- and final-state leptons
$P \overset{lab}{=} (M, \mathbf{0})$	4-momentum of the initial target proton
$q = \boldsymbol{k} - \boldsymbol{k}'$	4-momentum of the virtual photon
$Q^2 \equiv -q^2$	Negative squared 4-momentum transfer
$\nu \equiv \frac{P\cdot q}{M} \overset{lab}{=} E - E'$	Energy of the virtual photon
$x = \frac{Q^2}{2P\cdot q} = \frac{Q^2}{2M\nu}$	Bjorken scaling variable
$y \equiv \frac{P\cdot q}{P\cdot k} \overset{lab}{=} \frac{\nu}{E}$	Fractional energy of the virtual photon
$W^2 = (P+q)^2$	the mass squared of the proton-virtual photon system
$s = (k+P)^2$	the center-of-mass energy squared of the lepton-proton system
M	proton mass

frame as

$$\frac{d^2\sigma}{d\Omega dk'} = \frac{\alpha^2}{4k^2 \sin^4 \frac{\theta}{4}} \left(\frac{m_p}{P\cdot q} F_2(x, Q^2) \cos^2 \frac{\theta}{2} + \frac{2}{m_p} F_1(x, Q^2) \sin^2 \frac{\theta}{2} \right) \tag{2.2}$$

where θ is the lepton scattering angle and Ω is the solid angle of scattered lepton detection. The scaling variable x has been proposed by Bjorken[7]. It represents at large Q^2 the ratio of parton momentum to the proton momentum,

$$x = \frac{p_{\text{parton}}}{P_{\text{proton}}} \tag{2.3}$$

The structure function $F_2(x, Q^2)$ depends only on x and not on Q^2 in good approximation. This x scaling has been experimentally observed in SLAC data[8].

It is well established that the structure of the proton in high-energy (large Q^2) interactions can be described with the quark-parton model, in which all partons are assumed to be independent of each other. On the other hand, partons cannot be observed directly and are confined in hadrons. This phenomenon is called "color confinement" and indicates a strong coupling between quarks. These two behaviors can be consistently explained with the asymptotic freedom of non-Abelian gauge theory, which was discovered by Gross, Wilczek and Politzer in 1973[9][10][11][12]. The Q^2 dependence of the

strong coupling constant α_s at leading order is

$$\alpha_s(Q^2) = \frac{4\pi}{\beta_1 \ln(Q^2/\lambda_{QCD}^2)} \ , \quad \beta_1 = \frac{33 - 2n_f}{3} \tag{2.4}$$

where n_f is the number of flavors that can be virtually produced at a given Q^2, and $\lambda_{QCD} \approx 250$ MeV/c is the QCD scale. As seen in the equation, $\alpha_s(Q^2)$ decreases as Q^2 increases. Because of the smallness of $\alpha_s(Q^2)$ at large Q^2 ($\gg \lambda_{QCD}$), a hard-scattered parton can be regarded free, and the cross section for parton scattering is calculable using perturbative expansion[13].

The cross section for lepton-proton DIS can be factorized to the product of the parton distribution in the proton and the cross section for lepton-parton scattering. The proton internal structure is represented with the parton distribution function (PDF, $f(x)$). $f(x)$ means the probability of finding partons with a certain x. Often $q(x)$ and $g(x)$ are used as the $f(x)$ of quarks and gluons, respectively, and also $u(x)$, $\bar{u}(x)$, $d(x)$, etc. instead of $f(x)$ of each quark flavor.

Many DIS experiments with electron, muon or neutrino beam have measured the structure function of the proton and the neutron (with deuteron target), $F_2^p(x, Q^2)$ and $F_2^n(x, Q^2)$, which are well summarized in [14]. In the quark-parton model the structure function can be written as

$$F_2(x, Q^2) = x \cdot \sum_f e_f^2 \left(q_f(x, Q^2) + \bar{q}_f(x, Q^2) \right) \tag{2.5}$$

in the leading order, and the quark distribution functions can be extracted by globally analyzing all experimental data. Also the gluon distribution $g(x)$ can be determined with DIS data via the scaling violation (Q^2 dependence) of the $F_2(x, Q^2)$, which appears in higher-order calculation due to gluon radiation;

$$F_2(x, Q^2) = x \sum_q e_q^2 \Big\{ q(x, Q^2) + \frac{\alpha_s(Q^2)}{2\pi} \Big(C_q(x, \alpha_s) \otimes q(x, Q^2) \tag{2.6}$$

$$+ \frac{1}{N_f} C_g(x, \alpha_s) \otimes g(x, Q^2) \Big) \Big\} \tag{2.7}$$

The convolution $C_f(x, \alpha_s) \otimes f(x, Q^2)$ is defined as

$$C_f(x, \alpha_s) \otimes f(x, Q^2) \equiv \int_x^1 \frac{dy}{y} C(\frac{x}{y}, \alpha_s) f(y, Q^2) \tag{2.8}$$

where $f(y, Q^2)$ is the distribution density of parton f with a momentum fraction y, and $C(\frac{x}{y}, \alpha_s)$ is the probability that a quark q with a momentum fraction x is produced from a parton f with a momentum fraction y.

$C_f(x, \alpha_s)$ is called "coefficient function". In addition, global PDF analyses usually include jet production cross section in hadron-hadron collisions in order to improve the precision of $g(x)$. Figure 2.2 summarizes the PDFs determined by

- the ZEUS-JETS fits[15], which used inclusive DIS cross section, inclusive jet cross section and dijet cross section in e-p collisions by the ZEUS experiment,
- the ZEUS-S fit[16], which used inclusive DIS cross section in e-p collisions by the ZEUS experiment and fixed-target DIS cross section,
- the MRST2001 fit[17] and the CTEQ6.1M fit[18], which used inclusive DIS data, inclusive jet cross section in proton-antiproton collisions, etc.

All analyses have determined the PDFs with a good consistency.

The Q^2 dependence of the distribution functions is described by the DGLAP evolution equation[19][20][21] that has the schematic form of

$$\frac{\partial f_a}{\partial \ln Q^2} \sim \frac{\alpha_s(Q^2)}{2\pi} \sum_b P_{ab} \otimes f_b \tag{2.9}$$

where f_b is the distribution density of parton b, and P_{ab} is the probability that a parton a is produced from a parton b via $q \to qg$, $g \to q\bar{q}$ or $g \to gg$ splittings. Figure 2.3 shows the Q^2 evolution of $\int dx g(x)$ in the GRV98 PDF set[22]. Because the Q^2 evolution is rapid at lower x, the $\int_{10^{-4}}^{1} dx g(x)$ has a stronger Q^2 dependence than $\int_{0.02}^{0.3} dx g(x)$.

2.1.2 Polarized parton distribution function

The polarized (spin dependent) distribution functions of partons, $\Delta q(x)$ and $\Delta g(x)$, are defined as

$$\Delta q(x) \equiv q^+(x) - q^-(x) \tag{2.10}$$
$$\Delta g(x) \equiv g^+(x) - g^-(x) \tag{2.11}$$

where $q^+(x)$ ($q^-(x)$) is the probability of finding quarks which have a spin parallel (anti-parallel) to that of proton.

Many DIS experiments have measured the spin-dependent structure function of the proton and deuteron ($g_1^p(x, Q^2)$ and $g_1^d(x, Q^2)$), although the total amount of the experimental data is much less than $F_2(x, Q^2)$. Figure 2.4 shows the $g_1^p(x)$ and $g_1^d(x)$ measured by HERMES, E143, E155, SMC and

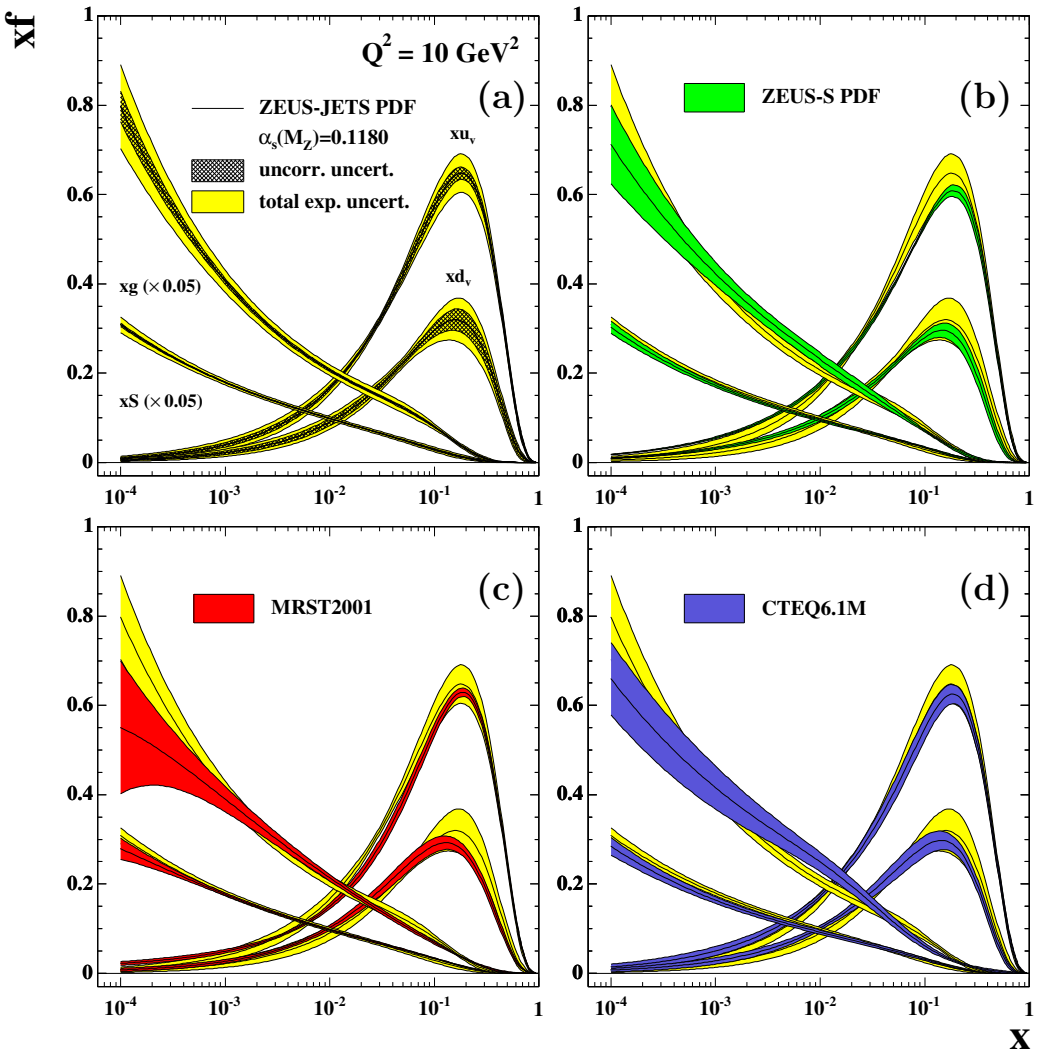

Figure 2.2: Unpolarized parton distribution functions (PDFs) determined by the ZEUS-JETS fit[15] (**Top left**), the ZEUS-S fit[16] (**Top right**), the MRST2001 fit[17] (**Bottom left**), and the CTEQ6.1M fit[18] (**Bottom right**). The PDFs by the ZEUS-JETS fit are drawn in all the plots for comparison.

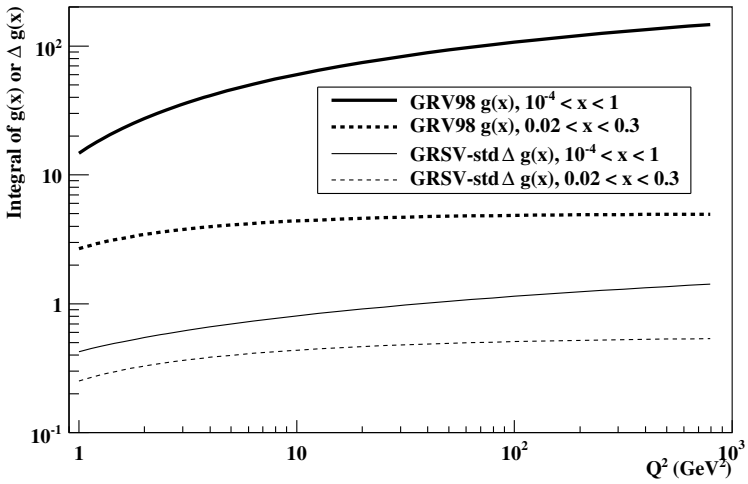

Figure 2.3: The Q^2 evolution of the unpolarized gluon distribution integral $\int dx g(x)$ and the polarized gluon distribution integral $\int dx \Delta g(x)$. Two integral ranges are sampled; a wide one ($10^{-4} < x < 1$) and a narrow one ($0.02 < x < 0.3$).

COMPASS experiments. The structure function of the neutron ($g_1^n(x)$) relates to the $g_1^p(x)$ and $g_1^d(x)$ as

$$g_1^d = \frac{1}{2}(g_1^p + g_1^n)\left(1 - \frac{3}{2}\omega_D\right) \tag{2.12}$$

where $\omega_D = 0.05 \pm 0.01$ takes into account the D-state admixture to the deuteron wave function. In the quark-parton model the $g_1(x, Q^2)$ can be written as

$$g_1(x, Q^2) = \frac{1}{2}\sum_f e_f^2 \left(\Delta q_f(x, Q^2) + \Delta \bar{q}_f(x, Q^2)\right) \tag{2.13}$$

in the leading order. The current $g_1(x, Q^2)$ data were however not sufficient to decompose the $g_1(x, Q^2)$ into the $\Delta f(x)$ of each flavor, particularly into the contributions from valence and sea quarks. The flavor decomposition has been achieved by the use of Semi-Inclusive measurement of DIS (SIDIS)[23][24]. It detects not only scattered leptons but also produced hadrons, whose flavor is correlated with the flavor of struck quarks.

The first moments of $\Delta q(x)$ and $\Delta g(x)$, namely $\int_0^1 dx x^{n-1} \Delta f(x)$ with

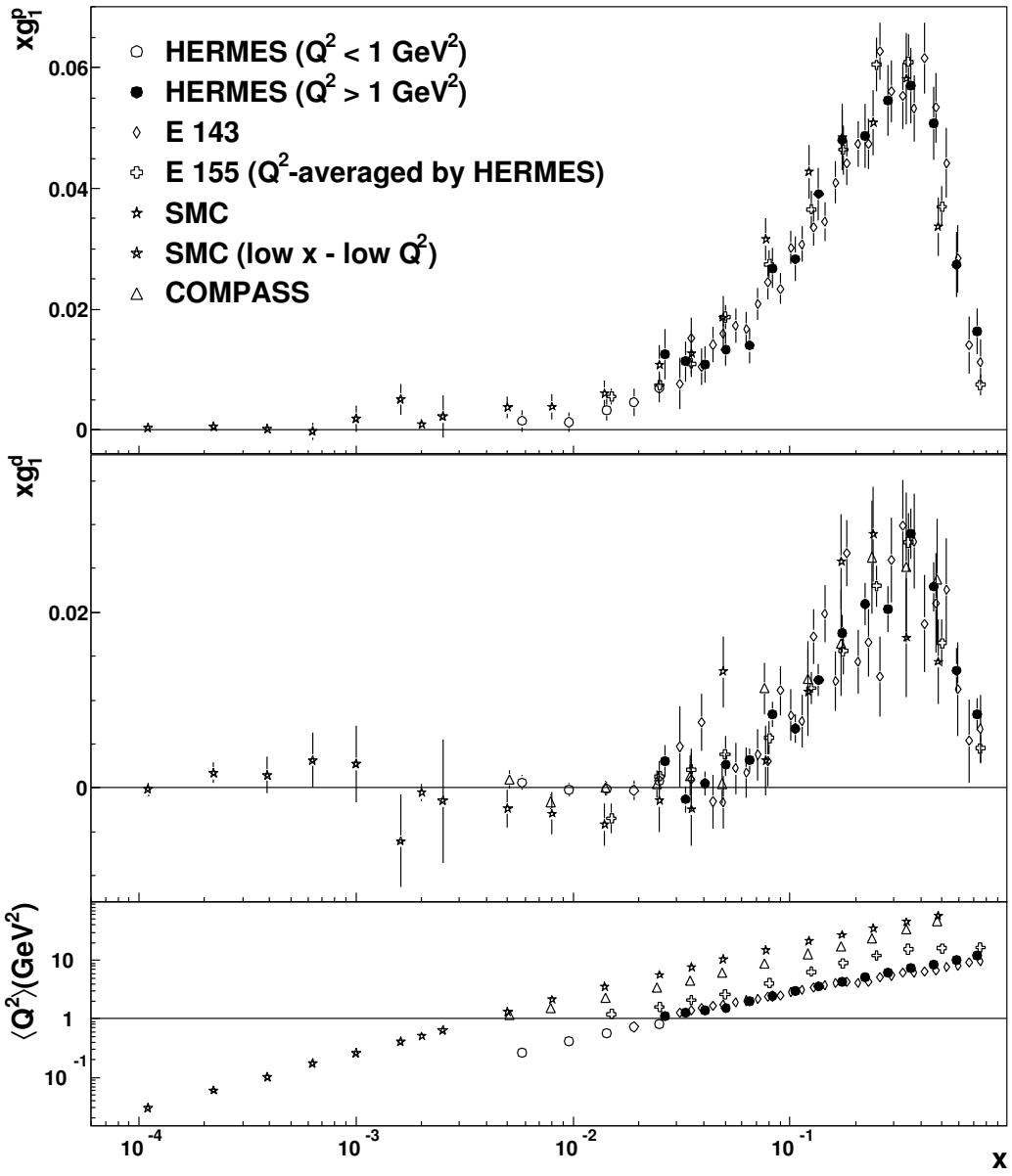

Figure 2.4: The structure function g_1 of the proton and deuteron. The bottom plot shows the mean value of Q^2 for each g_1^p or g_1^p point. ([5])

$n = 1$, mean the total spin of quarks and gluons in the proton,

$$\frac{1}{2}\Delta q \equiv \frac{1}{2}\int_0^1 dx \Delta q(x) = \frac{1}{2}\int_0^1 dx \left(q^+(x) - q^-(x)\right) \tag{2.14}$$

$$\Delta g \equiv \int_0^1 dx \Delta g(x) = \int_0^1 dx \left(g^+(x) - g^-(x)\right) \tag{2.15}$$

2.1.3 Sum rules and proton spin problem

Sum rules about the spin independent or dependent proton structure have been proposed by theories based on the quark-parton model. They have been tested by experiments to examine the validity of the quark-parton model.

Momentum sum rule

The total amount of quark momentum in the proton is given by the parton number density ($q(x)$) multiplied by the momentum fraction (x) as

$$S_{\rm quark}(Q^2) = \int_0^1 dx x\{u(x,Q^2) + \bar{u}(x,Q^2) + d(x,Q^2) + \bar{d}(x,Q^2) + s(x,Q^2) + \bar{s}(x,Q^2)\} \tag{2.16}$$

It can be represented by the proton and neutron structure functions with neutrino beam, $F_2^{\nu p}$ and $F_2^{\nu n}$, as

$$\int_0^1 dx\{F_2^{\nu p}(x,Q^2) + F_2^{\nu n}(x,Q^2)\} = 2S_{\rm quark}(Q^2) \tag{2.17}$$

In the naive quark-parton model, $S_{\rm quark}$ should be one, but actually the momentum carried by gluons ($S_{\rm gluon}(Q^2) = \int dx x g(x,Q^2)$) contributes to the proton momentum as

$$S_{\rm mom} = S_{\rm quark}(Q^2) + S_{\rm gluon}(Q^2) = 1 \tag{2.18}$$

The momentum sum rule cannot be tested accurately because $g(x,Q^2)$ is only determined indirectly. It is rather used to give a constraint on $g(x,Q^2)$. A global analysis of DIS data[25] shows $S_{\rm quark}(Q^2) \sim 0.5$ at $Q^2 \gtrsim 100$ GeV^2, which suggests $S_{\rm gluon}(Q^2) \sim 0.5$.

Gross-Llewellyn-Smith sum rule

The number of valence quarks in the proton must be three;

$$\int_0^1 dx \left\{u(x,Q^2) - \bar{u}(x,Q^2) + d(x,Q^2) - \bar{d}(x,Q^2)\right\} = 3 \tag{2.19}$$

The left side can be represented by the proton structure functions with neutrino and anti-neutrino beams, $F_3^{\nu p}$ and $F_3^{\bar{\nu} p}$. The Gross-Llewellyn-Smith sum rule[26] is

$$\begin{aligned} S_{\rm GLS}(Q^2) &= \frac{1}{2}\int_0^1 dx\{F_3^{\nu p}(x,Q^2) + F_3^{\bar{\nu} p}(x,Q^2)\} \\ &= 3\left\{1 - \frac{\alpha_s(Q^2)}{\pi} - 3.58\left(\frac{\alpha_s(Q^2)}{\pi}\right)^2 - 20.22\left(\frac{\alpha_s(Q^2)}{\pi}\right)^3\right\} \end{aligned} \tag{2.20}$$

where the polynomial of $\frac{\alpha_s(Q^2)}{\pi}$ is a QCD radiative correction with the number of flavors $N_f = 3$[27].

A measurement by the CCFR collaboration[28]

$$S_{\rm GLS}(Q^2 = 3\ {\rm GeV}^2) = 2.50 \pm 0.018({\rm stat}) \pm 0.078({\rm syst}) \tag{2.21}$$

agrees with the theoretical value of 2.66 ± 0.04.

Adler sum rule

The Adler sum rule[29] relates the proton structure functions with neutrino and anti-neutrino beams, $F_1^{\nu p}$ and $F_1^{\bar{\nu} p}$, to the difference between the number of u valence quarks and the number of d valence quarks in the proton;

$$\begin{aligned} S_{\rm A} &= \int_0^1 dx\{F_1^{\bar{\nu p}(x,Q^2)} - F_1^{\nu p}(x,Q^2)\} \\ &= \int_0^1 dx\left[\{u(x,Q^2) - \bar{u}(x,Q^2)\} - \{d(x,Q^2) - \bar{d}(x,Q^2)\}\right] = 1 \end{aligned} \tag{2.22}$$

It needs no QCD radiative correction because it can be derived from the commutator of conserved currents. The QCD evolution in the integral of $u - \bar{u}$ is exactly cancelled by that of $d - \bar{d}$.

A measurement by the WA25 experiment[30]

$$S_{\rm A} = 1.08 \pm 0.08({\rm stat}) \pm 0.18({\rm syst}) \tag{2.23}$$

agrees with the theoretical expectation although the experimental uncertainty is rather large.

Gottfried sum rule

The difference of the proton and neutron structure functions can be represented as

$$\begin{aligned} F_2^{ep}(x,Q^2) - F_2^{en}(x,Q^2) =& \frac{x}{3}\left[\{u(x,Q^2)+\bar{u}(x,Q^2)\} - \{d(x,Q^2)+\bar{d}(x,Q^2)\}\right] \\ =& \frac{x}{3}\left[\{u(x,Q^2)-\bar{u}(x,Q^2)\} - \{d(x,Q^2)-\bar{d}(x,Q^2)\}\right] \\ & - \frac{2x}{3}\left\{\bar{d}(x,Q^2)-\bar{u}(x,Q^2)\right\} \end{aligned} \tag{2.24}$$

The Gottfried sum rule assumes $\bar{u} = \bar{d}$ and is

$$S_{\rm G} = \int_0^1 \frac{dx}{x}\left\{F_2^{ep}(x,Q^2) - F_2^{en}(x,Q^2)\right\} = \frac{1}{3} \tag{2.25}$$

The New Muon Collaboration (NMC) reported the first evidence of a violation of the Gottfried sum rule[31][32]; $S_{\rm G}$ integrated over the range of $0.004 < x < 0.8$ is 0.2281 ± 0.0065(stat) at $Q^2 = 4$ GeV^2. It indicates a non-zero ($\sim$0.15) $\bar{d} - \bar{u}$. Since the NMC measurement, the non-zero $\bar{d} - \bar{u}$ and also its x dependence have been measured by Drell-Yan experiments, NA51[33] and E866/NuSea[34]. The theoretical understanding of the violation of the Gottfried sum rule has not been established yet. One possible source is the pion cloud of the nucleon, namely the $\bar{d}$ dominance in pions virtually produced via $p \to n\pi^+$[35].

Bjorken sum rule

The Bjorken sum rule[36] assumes the SU(2) isospin symmetry and is

$$\begin{aligned} S_{\rm Bj} &= \int_0^1 dx\{g_1^p(x,Q^2) - g_1^n(x,Q^2)\} \\ &= \frac{g_A}{6}\left\{1 - \frac{\alpha_s(Q^2)}{\pi} - 3.58\left(\frac{\alpha_s(Q^2)}{\pi}\right)^2 - 20.22\left(\frac{\alpha_s(Q^2)}{\pi}\right)^3\right\} \end{aligned} \tag{2.26}$$

where $g_A = 1.26$ is the isovector axial charge of the nucleon which is measured in neutron β decay. The polynomial of $\frac{\alpha_s(Q^2)}{\pi}$ is the QCD radiative correction just like in the Gross-Llewellyn-Smith sum rule. Because this sum rule has been derived from current algebra, it provides a very fundamental test of the structure of QCD.

A recent measurement by the E155 experiment[37]

$$S_{\rm Bj} = 0.176 \pm 0.003(\text{stat}) \pm 0.007(\text{syst}) \tag{2.27}$$

at $Q^2 = 5$ GeV^2 agrees with the theoretical value of 0.182 ± 0.005.

Ellis-Jaffe sum rule and proton spin problem

The integral of $g_1^p(x, Q^2)$ over x can be written as

$$\begin{aligned} S_p &= \int_0^1 dx g_1^p(x, Q^2) \\ &= \int_0^1 dx \left\{ \frac{4}{18}\Delta u(x, Q^2) + \frac{1}{18}\Delta d(x, Q^2) + \frac{1}{18}\Delta s(x, Q^2) \right\} \\ &= \frac{4}{18}\Delta u + \frac{1}{18}\Delta d + \frac{1}{18}\Delta s \end{aligned} \tag{2.28}$$

when the contribution of gluons to g_1^p is neglected. Under the assumption of SU(3) flavor symmetry, the first moments of polarized u, d and s distributions can be expressed with the singlet (a_0), triplet (a_3) and octet (a_8) axial charges as

$$a_0 = \Delta u + \Delta d + \Delta s \tag{2.29}$$

$$a_3 = \Delta u - \Delta d \tag{2.30}$$

$$a_8 = \Delta u + \Delta d - 2\Delta s \tag{2.31}$$

where $a_3 = g_A$, and $a_8 = 0.57 \pm 0.06$ is measured in hyperon β decay. Therefore S_p becomes

$$S_p = \frac{a_0}{9} + \frac{a_3}{12} + \frac{a_8}{36} \tag{2.32}$$

Since a_0 has not been directly measured by any experiments, s quark polarization is neglected ($\Delta s = 0$) so that $a_0 = a_8$. The Ellis-Jaffe sum rule[38] corrected for the QCD radiation[40] is

$$S_p(Q^2) = \frac{a_3}{12}\left\{1 - \frac{\alpha_s(Q^2)}{\pi}\right\} + \frac{5a_8}{36}\left\{1 - \frac{7}{15}\frac{\alpha_s(Q^2)}{\pi}\right\} \tag{2.33}$$

With the values of g_A and Δq_8 quoted above, S_p at $Q^2 = 10$ GeV^2 is expected to be 0.167 ± 0.008.

S_p was measured by the EMC experiment at CERN in 1988, and was revealed to be $0.114 \pm 0.012 \pm 0.026$[2]. It is clearly inconsistent with the Ellis-Jaffe sum rule. Earlier SLAC measurements did not detect this deviation because the covered x range was only down to 0.1 and therefore the error was large. This inconsistency indicates that at least one of the assumptions is wrong; rather large contributions of s quark or gluons to g_1^p, or SU(3) flavor asymmetry. Altarelli and Ross[4] show that the contribution of the gluon spin to g_1^p can be large even at large Q^2 due to the triangle anomaly;

$$a_0 = 2\sqrt{\frac{2}{3}}\left(\Delta u + \Delta d + \Delta s - \frac{3\alpha_s}{4\pi}\Delta g\right). \tag{2.34}$$

The Ellis-Jaffe sum rule can hold if Δg is quite large (~ 5), although it needs a large opposite contribution of orbital angular momenta in order to conserve the total proton spin and there is a different theoretical interpretation of the contribution of the gluon spin to g_1^p[39].

The proton spin can be expressed with angular momenta of its constituents, namely spins and orbital angular momenta of quarks and gluons;

$$\frac{1}{2} = \frac{1}{2}\sum_f \Delta q_f + \Delta g + L_q + L_g \tag{2.35}$$

where f is a flavor of quarks (u, d, s, $\bar{u}$, $\bar{d}$, and $\bar{s}$). The contribution of the quark spin $\frac{1}{2}\sum_f \Delta q_f$ is equal to $\frac{1}{2}a_0$. After the EMC experiment many experiments have measured S_p even more precisely. The recent result of the HERMES analysis[5] showed

$$\sum_f \Delta q_f = 0.330 \pm 0.011(\text{theo.}) \pm 0.025(\text{exp.}) \pm 0.028(\text{evol.}) \tag{2.36}$$

at $Q^2 \sim 5$ GeV^2, which is only $\sim$30% of the proton spin.

Ji sum rule

Ji sum rule[41][42][43] formulates a gauge invariant decomposition of the nucleon spin into the contributions of quark helicity, quark orbital angular momentum and gluon angular momentum. It also introduces generalized parton distributions (GPDs; $H(x,\xi,t)$, $E(x,\xi,t)$, $\tilde{H}(x,\xi,t)$ and $\tilde{E}(x,\xi,t)$), which contain the information on the nucleon structure represented by both the nucleon form factors and the parton distribution functions.

The QCD angular momentum operator ($\vec{J}_{\text{QCD}}$) can be separated into gauge-invariant quark and gluon parts; $\vec{J}_{\text{QCD}} = \vec{J}_q + \vec{J}_g$. Using energy-momentum tensor $T^{\mu\nu}_{q,g}$, $\vec{J}_q$ and $\vec{J}_g$ can be written as

$$J^i_{q,g} = \frac{1}{2}\epsilon^{ijk}\int d^3x (T^{0k}_{q,g}x^j - T^{0j}_{q,g}x^k) \tag{2.37}$$

and using QCD equations of motion and superpotentials,

$$\begin{aligned}\vec{J}_q &= \int d^3x \psi^\dagger[\vec{\gamma}\gamma_5 + (\vec{x}\times i\vec{D})]\psi \\ \vec{J}_g &= \int d^3x (\vec{x}\times(\vec{E}\times\vec{B}))\end{aligned} \tag{2.38}$$

In $\vec{J}_q$, $\vec{\gamma}\gamma_5$ means a quark helicity contribution and $(\vec{x}\times i\vec{D})$ a quark orbital contribution. These two are separated in this gauge-invariant expression.

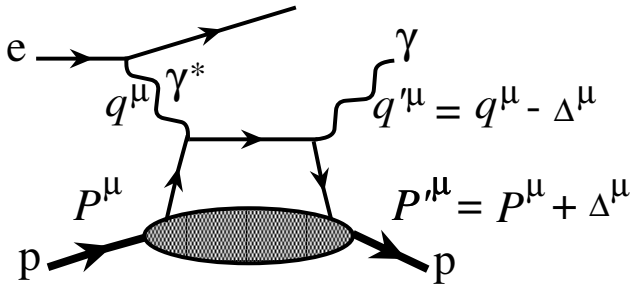

Figure 2.5: Handbag diagram of Deeply Virtual Compton Scattering (DVCS), $ep \to ep\gamma$.

On the other hand, in $\vec{J}_g$, two contributions cannot be separated because the spin space of gluons coincides with the ordinary space and time.

One possible process that can probe $\vec{J}_q$ is Deeply Virtual Compton Scattering (DVCS), which is illustrated in Fig. 2.5. Momentum vectors of initial-state proton, final-state proton, virtual photon and final-state photon are represented by P^μ, P'^μ, q^μ and q'^μ, respectively. The momentum transfer from photon to proton is represented by Δ^μ. When momentum vectors are expanded in terms of two light-like vectors, $p^\mu = \Lambda(1,0,0,1)$ and $n^\mu = (1,0,0,-1)/(2\Lambda)$, where Λ is an arbitrary constant, the amplitude of the $\gamma^* p \to \gamma p$ part can be written as

$$\begin{aligned} T^{\mu\nu}(P,q,\Delta) = {} & \frac{1}{2}(g^{\mu\nu} - p^\mu n^\nu - p^\nu n^\mu) \int_{-1}^{1} dx \left(\frac{1}{x - \xi/2 + i\epsilon} + \frac{1}{x + \xi/2 - i\epsilon} \right) \\ & \times \left[H(x,\xi,\Delta^2) \bar{U}(P') \not{n} U(P) + E(x,\xi,\Delta^2) \bar{U}(P') \frac{i\sigma^{\alpha\beta} n_\alpha \Delta_\beta}{2M} U(P) \right] \\ & + \frac{i}{2} \epsilon^{\mu\nu\alpha\beta} p_\alpha n_\beta \int_{-1}^{1} dx \left(\frac{1}{x - \xi/2 + i\epsilon} - \frac{1}{x + \xi/2 - i\epsilon} \right) \\ & \times \left[\tilde{H}(x,\xi,\Delta^2) \bar{U}(P') \not{n} \gamma_5 U(P) + \tilde{E}(x,\xi,\Delta^2) \frac{\Delta \cdot n}{2M} \bar{U}(P') \gamma_5 U(P) \right] \end{aligned} \tag{2.39}$$

where the negative x in the integral corresponds to anti-quarks with a momentum fraction $|x|$; ξ means the change of the momentum fraction x of a scattered quark ($x + \xi/2 \xrightarrow{scatt.} x - \xi/2$); H, $\tilde{H}$, E and $\tilde{E}$ are off-forward parton distributions. These distributions can be connected to the usual form

factors;

$$\int_{-1}^{1} dx H(x,\xi,\Delta^2) = F_1(\Delta^2)$$
$$\int_{-1}^{1} dx E(x,\xi,\Delta^2) = F_2(\Delta^2)$$
$$\int_{-1}^{1} dx \tilde{H}(x,\xi,\Delta^2) = G_A(\Delta^2)$$
$$\int_{-1}^{1} dx \tilde{E}(x,\xi,\Delta^2) = G_P(\Delta^2) \tag{2.40}$$

They become the usual parton distribution functions at the forward limit ($\Delta^\mu \to 0$);

$$H(x,\xi,\Delta^\mu \to 0) = q(x) \quad , \quad \tilde{H}(x,\xi,\Delta^\mu \to 0) = \Delta q(x) \tag{2.41}$$

The contribution of the quark angular momentum to the proton spin (J_q) can be expressed with the second moment of GPDs at the forward limit ($\Delta^\mu \to 0$) as

$$J_q = \int_{-1}^{1} dx x[H(x,\xi,\Delta^\mu \to 0) + E(x,\xi,\Delta^\mu \to 0)] \tag{2.42}$$

2.1.4 $\Delta g(x)$ measurement with DIS

$\Delta g(x)$ can be determined with polarized DIS data via the scaling violation (Q^2 dependence) of the structure function $g_1(x, Q^2)$. In 2000 the GRSV group (Gluck, Reya, Stratmann and Vogelsang) evaluated polarized PDFs including $\Delta g(x)$ with polarized DIS data in a NLO pQCD framework[44]. It assumed the SU(3)$_f$ symmetry and the functional forms of $\Delta f(x, {\mu_0}^2)$ as

$$\Delta u(x,{\mu_0}^2) = N_u x^{\alpha_u}(1-x)^{\beta_u} u(x,{\mu_0}^2)_{\rm GRV}$$
$$\Delta d(x,{\mu_0}^2) = N_d x^{\alpha_d}(1-x)^{\beta_d} d(x,{\mu_0}^2)_{\rm GRV}$$
$$\Delta \bar{q}(x,{\mu_0}^2) = N_{\bar{q}} x^{\alpha_{\bar{q}}}(1-x)^{\beta_{\bar{q}}} \bar{q}(x,{\mu_0}^2)_{\rm GRV}$$
$$\Delta g(x,{\mu_0}^2) = N_g x^{\alpha_g}(1-x)^{\beta_g} g(x,{\mu_0}^2)_{\rm GRV} \tag{2.43}$$

where ${\mu_0}^2 = 0.4$ GeV^2 is the initial scale where the functional forms are defined as above; $u(x,{\mu_0}^2)_{\rm GRV}$ etc. are the unpolarized PDF of the GRV98[22]. Figure 2.6 shows polarized PDFs $\Delta u(x)$, $\Delta d(x)$, $\Delta \bar{q}(x)$ and $\Delta g(x)$ that have been evaluated by the GRSV analysis. The polarized valence-quark distribution functions are well determined.

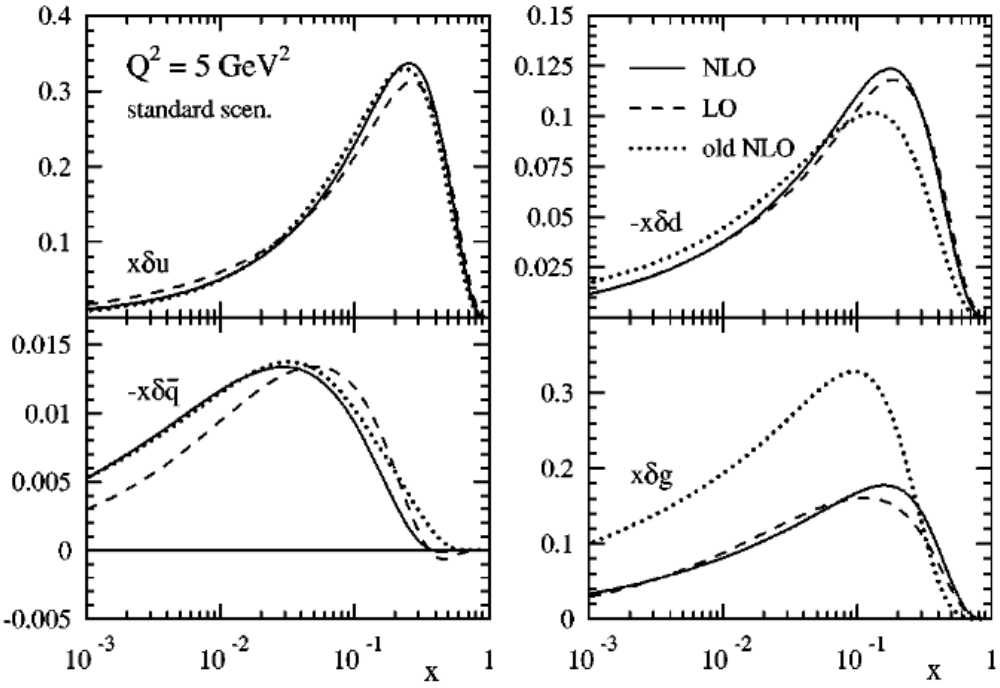

Figure 2.6: Polarized PDFs determined by the GRSV analysis[44].

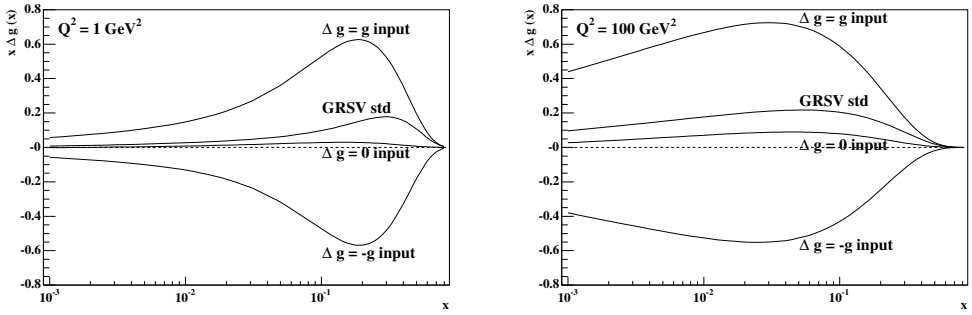

Figure 2.7: Q^2 dependence of $\Delta g(x)$ determined by the GRSV analysis[44].

Figure 2.7 shows four distributions of $\Delta g(x)$ at $Q^2 = 1$ and 100 GeV^2; one is the optimal distribution in the GRSV analysis (named "GRSV std"), and the other three are the distributions that are defined as

$$\begin{aligned} \Delta g(x, {\mu_0}^2) &= g(x, {\mu_0}^2)_{\rm GRV} \\ \Delta g(x, {\mu_0}^2) &= 0 \\ \Delta g(x, {\mu_0}^2) &= -g(x, {\mu_0}^2)_{\rm GRV} \end{aligned} \tag{2.44}$$

named "$\Delta g = g$ input", "$\Delta g = 0$ input" and "$\Delta g = -g$ input", respectively. The "$\Delta g = g$ input" and "$\Delta g = -g$ input" scenarios mean an extremely large gluon polarization in the proton, but are not inconsistent with the DIS data within their uncertainties and thus have not been excluded by the GRSV analysis. Figure 2.3 shows the Q^2 evolution of the integral of the GRSV-std gluon distribution as well as the unpolarized one.

The BB (Blumlein and Bottcher)[45] and the AAC (Asymmetry Analysis Collaboration)[46] are newer global analyses that adopted newer experimental data, another parameterization and/or another error estimation method. Figure 2.8 shows the polarized PDFs determined by the BB analysis with 1σ error bands drawn as the shaded areas. The PDFs by the GRSV and AAC analyses are also drawn for comparison. The errors of the three analyses on $\Delta g(x)$ are roughly same. Note that the definition of "1σ error" in the AAC analysis is different from others; it assigns the error to the polarized gluon distribution using χ^2 increase of 12.647 since 11 parameters are involved in the fit. All these analyses which used inclusive DIS data provide only a rough constraint on $\Delta g(x)$. It suggests positive $\Delta g(x)$ though not conclusive.

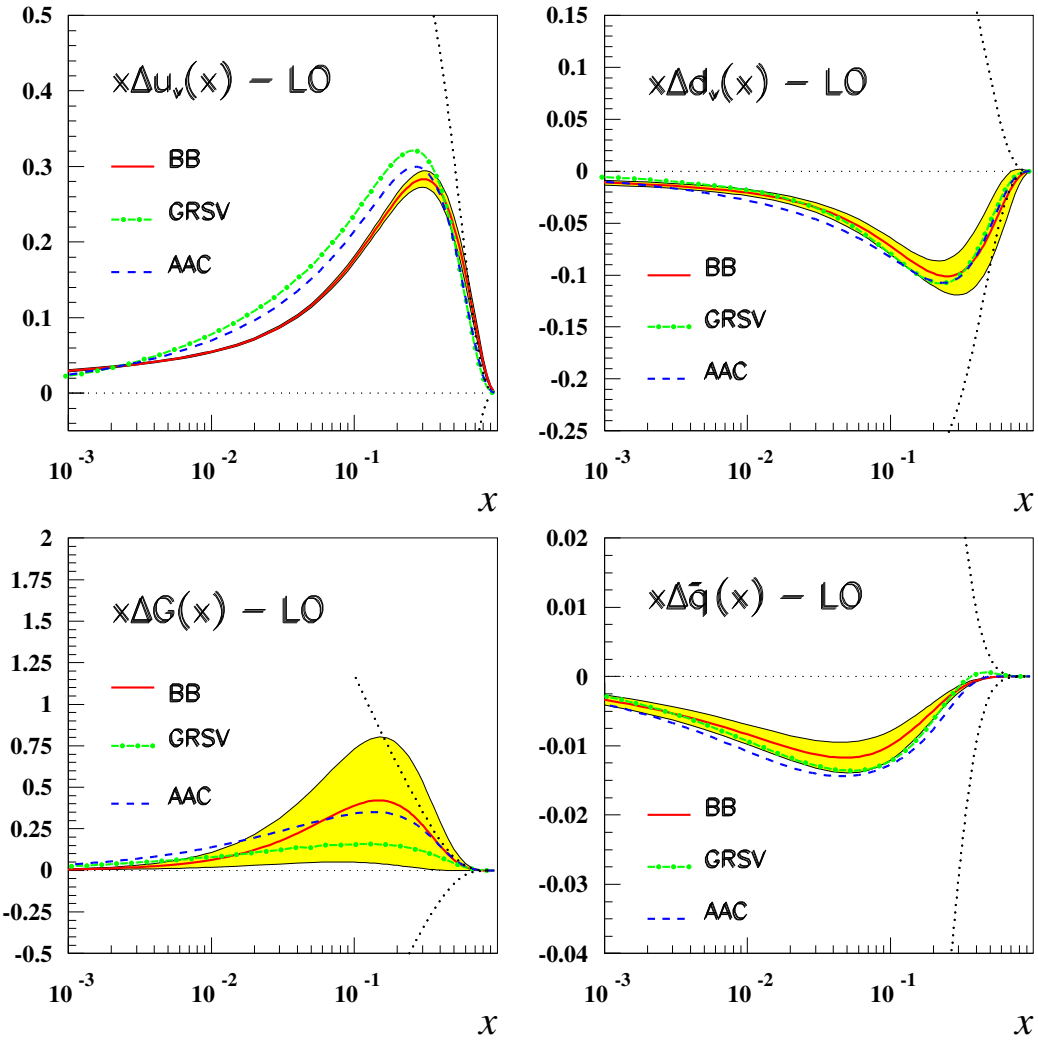

Figure 2.8: Polarized PDFs at the scale $Q^2 = 4$ GeV^2 determined by the BB NLO Scenario-I analysis. The shaded areas represent fully correlated 1σ error bands. Also polarized PDFs by the GRSV and AAC analyses are drawn for comparison. The dotted lines are unpolarized PDFs ($\pm f(x)$) and indicate the positivity limit, $|\Delta f(x)| < f(x)$. ([45])

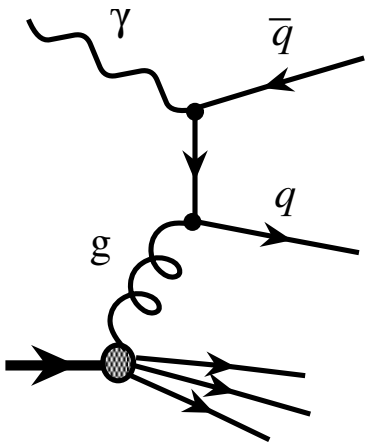

Figure 2.9: The process of virtual photon-gluon fusion.

2.1.5 $\Delta g(x)$ measurement with SIDIS

Δg can be measured with Semi-Inclusive DIS (SIDIS) data via the process of virtual photon-gluon fusion, $g\gamma^* \to q\bar{q}$, illustrated in Fig. 2.9. When the $q\bar{q}$ pair in the final state is a $c\bar{c}$ pair, this process can be clearly identified by reconstructing D mesons, although the statistics is limited. When the $q\bar{q}$ pair is a light quark pair and becomes two jets, this process is characterized by the two jets having large transverse momentum (p_T), where p_T is the momentum component perpendicular to the direction of the virtual photon. In the latter case, there are several background processes whose detection rate is similar to that of the signal process; the QCD Compton ($q\gamma^* \to qg$ instead of $g\gamma^* \to q\bar{q}$) and the Vector Meson Dominance process (interaction with the hadronic structure of the virtual photon). The subtraction of the background processes have been studied mainly with the PYTHIA event generator. The HERMES experiment published a first result in 2000[47], and the HERMES and COMPASS experiments are carrying out further analyses with updated data. Figure 2.10 shows preliminary results of the SIDIS measurement. All measurements indicate small Δg at measured region $x \sim 0.1$.

2.1.6 $\Delta g(x)$ measurement with proton-proton collisions

Longitudinally polarized proton-proton collisions are the powerful tool to access to $\Delta g(x)$, since gluon in the proton can directly scatter via strong interaction. The main reactions to probe $\Delta g(x)$ are

- direct photon production ($\vec{p}\vec{p} \to \gamma X$),

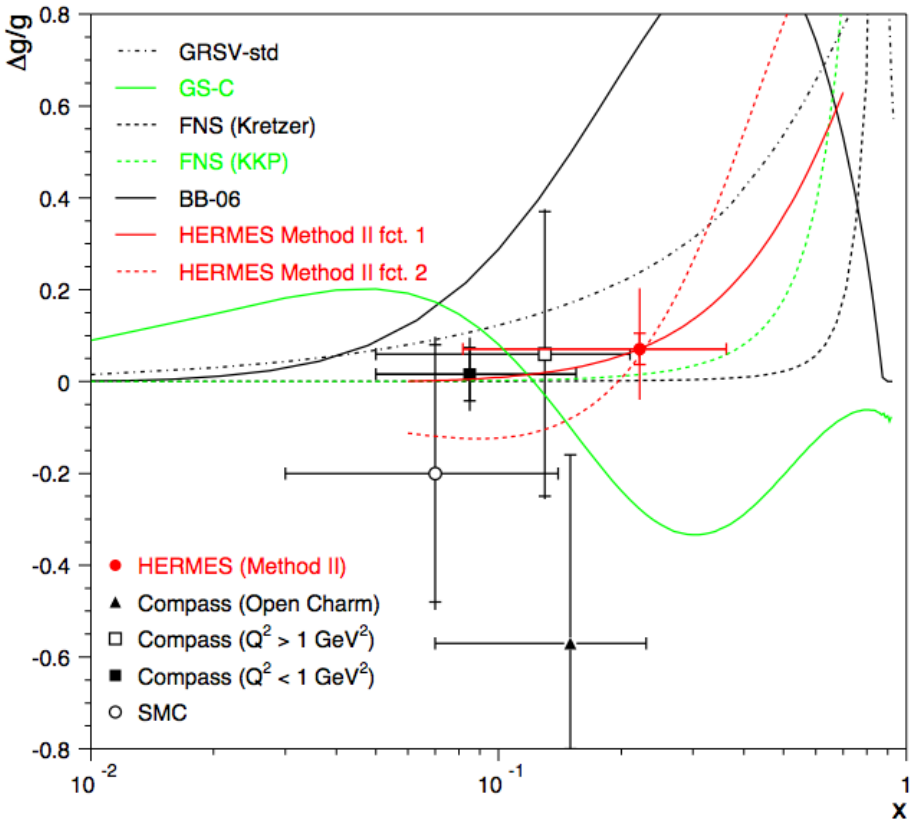

Figure 2.10: Preliminary results of the gluon polarization evaluated with the virtual photon and gluon fusion process in SIDIS. The length of a vertical error bar represents the quadratic sum of statistical and systematic errors, and the small tick on the vertical error bar represents the size of the statistical error.

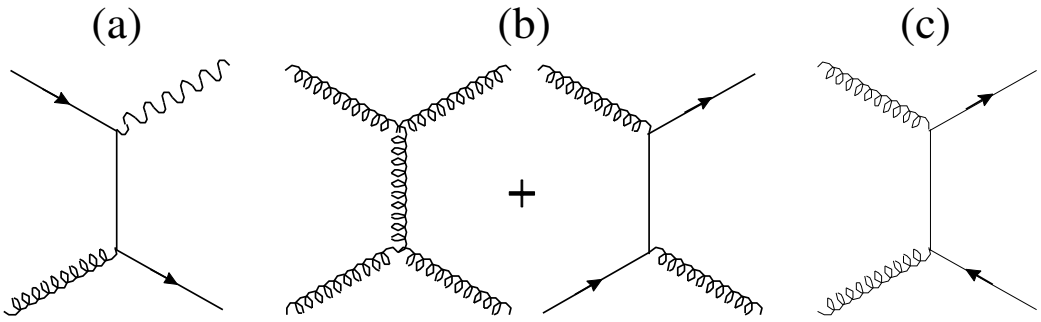

Figure 2.11: Examples of lowest-order Feynman diagrams for elementary processes with gluons in the initial state in pp collisions; (a) quark-gluon Compton process for prompt-photon production, (b) gluon-gluon and gluon-quark scattering for jet production, and (c) gluon-gluon fusion for heavy quark pair production. ([48])

- jet production ($\vec{p}\vec{p} \rightarrow jetX$), and
- heavy flavor pair production ($\vec{p}\vec{p} \rightarrow c\bar{c}X, b\bar{b}X$).

Figure 2.11 shows the lowest-order Feynman diagram for each process.

Direct photons are produced via $qg \rightarrow \gamma q$ and $q\bar{q} \rightarrow \gamma g$. The quark-gluon Compton process ($qg \rightarrow \gamma q$) is favored in proton-proton collisions as opposed to proton-antiproton collisions. Direct photons are promptly produced from parton-parton scattering and are measured without any conversion or decay. Therefore the measurement of direct photons can determine Δg precisely.

Jets are produced via gg scattering (including $gg \rightarrow gg$, $gg \rightarrow q_k\bar{q}_k$, where the subscript denotes quark flavor), qg scattering ($q_ig \rightarrow q_ig$) and qq scattering ($q_iq_j \rightarrow q_iq_j$, $q_i\bar{q}_i \rightarrow q_k\bar{q}_k$, $q_i\bar{q}_i \rightarrow gg$). There are two approaches to measure the jet production process for the Δg determination;

- measuring all produced particles as a jet, and
- measuring only leading hadrons such as π^0 or $\pi^{\pm}$ in a jet.

The advantage of jet production is its large cross section, which is roughly 100 times larger than that of the direct photon production.

Heavy flavor pairs are produced via $gg \rightarrow q\bar{q}$ to form D, B, or J/Ψ mesons and are detected with μ^+, μ^-, e^+, and/or e^-. The heavy flavor measurement can probe the low x region because even at small p_T the heavy quark mass assures large Q^2 where the theory calculation can safely use the perturbative expansion.

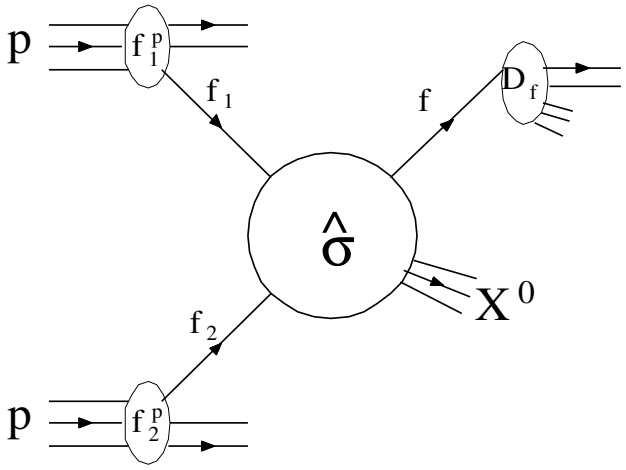

Figure 2.12: Diagram of π^0 production in proton-proton collision[48].

Unpolarized cross section

The unpolarized cross section for inclusive pion production ($pp \to \pi X$), as an example, illustrated in Fig. 2.12, can be written as

$$\sigma^{pp\to\pi X} = \sum_{f_1,f_2,f} \int dx_1 dx_2 dz f_1(x_1,\mu^2) f_2(x_1,\mu^2) \times \hat{\sigma}^{f_1 f_2 \to f X'}(x_1 p_1, x_2 p_2, p_\pi/z, \mu) D_f^\pi(z,\mu^2) \qquad (2.45)$$

where f_1 and f_2 are q_f or g. The equation is factorized into three elements; 1) parton distribution function (f_1, f_2), 2) parton-parton scattering cross section ($\hat{\sigma}^{f_1 f_2 \to f X'}$), and 3) fragmentation function (D_f^π). The fragmentation function represents the finding probability of a particle (π in this case) with a momentum fraction of z in the parton f.

Polarized cross section and double helicity asymmetry

The polarized cross section for inclusive pion production is defined as

$$\begin{aligned}\Delta\sigma^{pp\to\pi X} \equiv & \frac{1}{4}\left[\sigma_{++}^{pp\to\pi X} - \sigma_{+-}^{pp\to\pi X} - \sigma_{-+}^{pp\to\pi X} + \sigma_{--}^{pp\to\pi X}\right] \\ = & \sum_{f_1,f_2,f}\int dx_1 dx_2 dz \Delta f_1(x_1,\mu^2)\Delta f_2(x_1,\mu^2) \\ & \times \Delta\hat{\sigma}^{f_1 f_2\to fX'}(x_1 p_1, x_2 p_2, p_\pi/z, \mu) D_f^\pi(z,\mu^2)\end{aligned} \tag{2.46}$$

$$\Delta\hat{\sigma}^{f_1 f_2\to fX'} \equiv \frac{1}{4}\left[\hat{\sigma}_{++}^{f_1 f_2\to fX'} - \hat{\sigma}_{+-}^{f_1 f_2\to fX'} - \hat{\sigma}_{-+}^{f_1 f_2\to fX'} + \hat{\sigma}_{--}^{f_1 f_2\to fX'}\right] \tag{2.47}$$

where "+" and "−" denote the helicity of proton or parton, and $\Delta\hat{\sigma}^{f_1 f_2\to fX'}$ is polarized parton-parton cross section. The parton-parton cross section is well predicted by perturbative Quantum-Chromo Dynamics (pQCD), and the fragmentation function has been determined with electron-positron collision experiments and lepton-nucleon DIS experiments. Therefore, the polarized parton distribution function can be extracted from the polarized cross section of the pion production.

The double helicity asymmetry (A_{LL}) is defined as

$$A_{LL} \equiv \frac{\Delta\sigma}{\sigma} \tag{2.48}$$

We usually measure A_{LL} instead of the absolute value of $\Delta\sigma$ itself to access the information on Δg, because many systematic errors cancel out between the denominator σ and the numerator $\Delta\sigma$ and thus a precise measurement can be achieved. The A_{LL} of pion production is derived from Eq. 2.45 and Eq. 2.46 as

$$A_{LL} = \frac{\sum_{f_1,f_2,f}\int dx_1 dx_2 dz \cdot \Delta f_1 \cdot \Delta f_2 \cdot \hat{\sigma}^{f_1 f_2\to fX'} \cdot \hat{a}_{LL}^{f_1 f_2\to fX'} \cdot D_f^\pi}{\sum_{f_1,f_2,f}\int dx_1 dx_2 dz \cdot f_1 \cdot f_2 \cdot \hat{\sigma}^{f_1 f_2\to fX'} \cdot D_f^\pi} \tag{2.49}$$

where $\hat{a}_{LL}^{f_1 f_2\to fX'}$ is the spin-dependent asymmetry for the parton-parton scattering,

$$\hat{a}_{LL}^{f_1 f_2\to fX'} \equiv \frac{\Delta\hat{\sigma}^{f_1 f_2\to fX'}}{\hat{\sigma}^{f_1 f_2\to fX'}} \tag{2.50}$$

and is called "analyzing power" because the non-zero $\hat{a}_{LL}$ makes A_{LL} sensitive to Δf. Table 2.2 shows the lowest-order unpolarized and polarized partonic cross sections that are related to jet production process. Figure 2.13 shows the lowest-order analyzing powers as functions of the partonic scattering angle in center-of-mass system. At mid-rapidity ($\theta \sim 0$) the $gg \to gg$ subprocess, which dominates in the jet production process, has large $\hat{a}_{LL}$.

Table 2.2: The lowest-order unpolarized cross sections and analyzing powers that are related to jet production process[49]. Subscript i or j ($i \neq j$) specifies a quark flavor. s, t and u are Mandelstam variables of parton-parton scattering.

Subprocess	Unpolarized cross section	Analyzing power $\hat{a}_{LL}$
$q_i q_j \to q_i q_j$	$\frac{4\pi\alpha_s^2}{9s^2}\frac{s^2+u^2}{t^2}$	$\frac{s^2-u^2}{s^2+u^2}$
$q_i \bar{q}_i \to q_j \bar{q}_j$	$\frac{4\pi\alpha_s^2}{9s^2}\frac{t^2+u^2}{s^2}$	-1
$q_i \bar{q}_i \to q_i \bar{q}_i$	$\frac{4\pi\alpha_s^2}{9s^2}\left[\frac{s^2+u^2}{t^2}+\frac{t^2+u^2}{s^2}-\frac{2}{3}\frac{u^2}{st}\right]$	$\frac{\frac{s^2-u^2}{t^2}-\frac{t^2+u^2}{s^2}+\frac{2}{3}\frac{u^2}{st}}{\frac{s^2+u^2}{t^2}+\frac{t^2+u^2}{s^2}-\frac{2}{3}\frac{u^2}{st}}$
$q_i q_i \to q_i q_i$	$\frac{4\pi\alpha_s^2}{9s^2}\left[\frac{s^2+u^2}{t^2}+\frac{s^2+t^2}{u^2}-\frac{2}{3}\frac{s^2}{ut}\right]$	$\frac{\frac{s^2-u^2}{t^2}+\frac{s^2-t^2}{u^2}-\frac{2}{3}\frac{s^2}{ut}}{\frac{s^2+u^2}{t^2}+\frac{s^2+t^2}{u^2}-\frac{2}{3}\frac{s^2}{ut}}$
$q_i \bar{q}_i \to gg$	$\frac{32\pi\alpha_s^2}{27s^2}\left[\frac{u}{t}+\frac{t}{u}-\frac{9}{4}\frac{t^2+u^2}{s^2}\right]$	-1
$q_i g \to q_i g$	$\frac{4\pi\alpha_s^2}{9s^2}\left[-\frac{u}{s}-\frac{s}{u}+\frac{9}{4}\frac{s^2+u^2}{t^2}\right]$	$\frac{s^2-u^2}{s^2+u^2}$
$gg \to q_i \bar{q}_i$	$\frac{\pi\alpha_s^2}{6s^2}\left[\frac{u}{t}+\frac{t}{u}-\frac{9}{4}\frac{t^2+u^2}{s^2}\right]$	-1
$gg \to gg$	$\frac{9\pi\alpha_s^2}{2s^2}\left[3-\frac{tu}{s^2}-\frac{su}{t^2}-\frac{st}{u^2}\right]$	$\frac{-3+\frac{2s^2}{ut}+\frac{ut}{s^2}}{3-\frac{tu}{s^2}-\frac{su}{t^2}-\frac{st}{u^2}}$

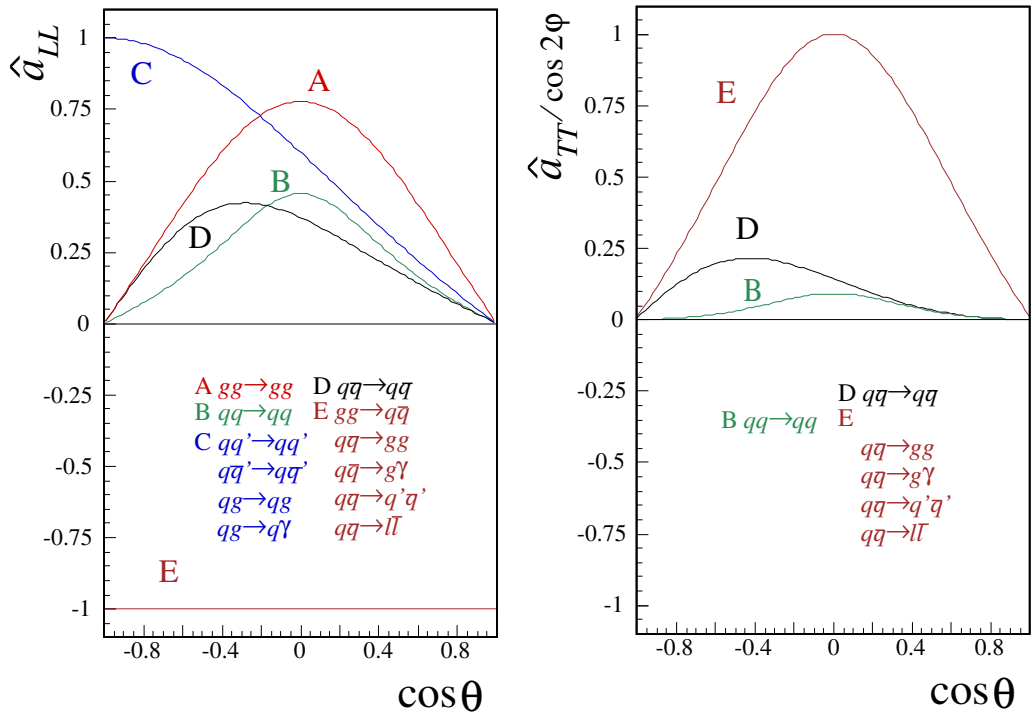

Figure 2.13: Lowest-order analyzing powers[49] for various reactions relevant to RHIC, as functions of the partonic scattering angle in center-of-mass system, θ. Left: longitudinal polarization, right: transverse polarization (a factor $\cos(2\phi)$ has been taken out, where ϕ is the azimuthal angle of one produced particle).

Sensitivity of A_{LL} to $\Delta g(x)$

The A_{LL} in jet production is contributed from three subprocesses, gg, qg and qq scatterings. The qq subprocess can make a non-zero A_{LL}, but such A_{LL} is not sensitive to $\Delta g(x)$ but only to $\Delta q(x)$. Therefore, when the fraction of gg and qg subprocesses are larger, the A_{LL} becomes more sensitive to $\Delta g(x)$. The gg subprocess always makes a positive A_{LL} with positive or negative $\Delta g(x)$ because $A_{LL} \sim \Delta g(x) \times \Delta g(x)$. Therefore the qg subprocess has an advantage in determining the sign of $\Delta g(x)$.

Figure 2.14 shows the fraction of gg, qg and qq subprocesses in unpolarized jet, particle cluster and π^0 production processes as functions of p_T. The "particle cluster" is a jet core that is measured by this analysis, and the definition is described later. The π^0 is a particle produced in the jet fragmentation. Therefore the p_T of a particle cluster and a π^0 in an event is a fraction of a jet in the event. A relation $p_T^{\rm jet} \sim p_T^{\rm particle\ cluster}/0.8 \sim p_T^{\pi 0}/0.5$ holds on average, although the ratios largely fluctuate event-by-event. All production processes are dominated by qg or gg subprocess in the p_T range shown. As stated in Chapter 1, the measurement of particle cluster is more sensitive to qg subprocess than the measurement of inclusive π^0. Thus, it is suited to determine the sign of $\Delta g(x)$.

2.2 Jet production in proton-proton collisions

2.2.1 Jet cone and clustering procedure

Jet is a group of particles fragmented from a scattered parton as illustrated in Fig. 2.15. The fragmentation is caused by the confinement of a parton by strong color interaction. The phenomenon of jet production was discovered in 1975 at SLAC with $e^+e^- \to q\bar{q}$ reaction[50]. The momenta of particles in a jet have almost the same direction as that of the original parton, but are spread a little within the principle of uncertainty. The transverse component of the momentum of each particle against the jet direction is independent of the jet momentum itself and the mean value is almost constant;

$$\langle j_T \rangle \sim 300 \text{ MeV}/c \tag{2.51}$$

Figure 2.16 shows energy flow in ϕ-η (transverse) plane measured in proton-antiproton collisions by CDF Collaboration[51]. ϕ is the azimuthal angle around the proton beam axis. η is the pseudo-rapidity which is defined with the polar angle from the proton beam axis (θ) as

$$\eta \equiv -\ln\left(\tan\frac{\theta}{2}\right) \tag{2.52}$$

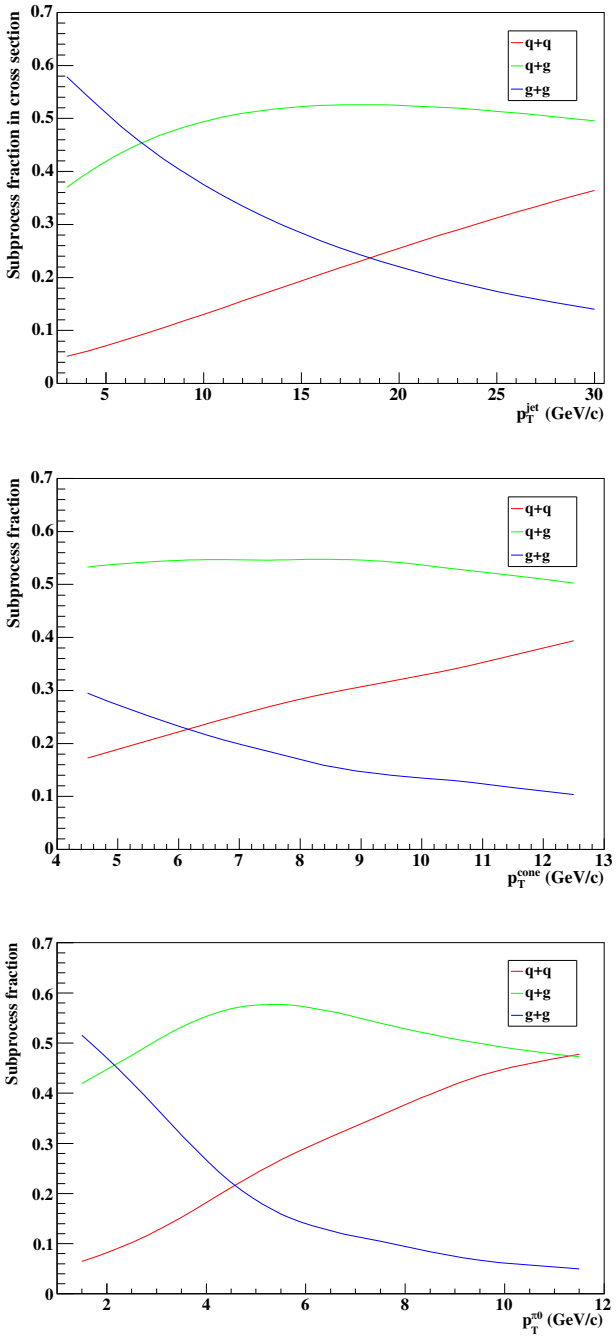

Figure 2.14: Subprocess fractions in unpolarized jet (**Top**), particle cluster (**Middle**) and π^0 (**Bottom**) production processes as functions of p_T. The first was evaluated with a pQCD NLO calculation, and the others with a PYTHIA event generator. Detailed information on the processes is described later.

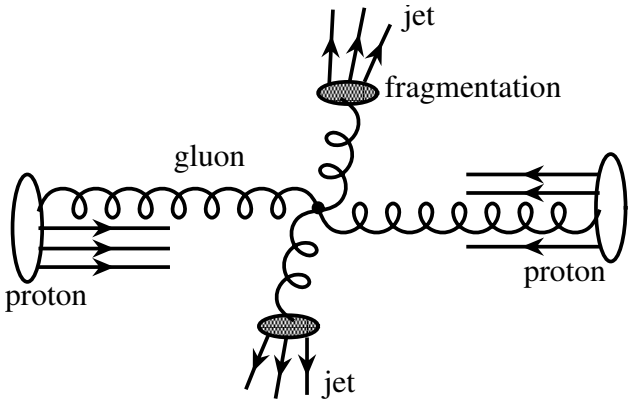

Figure 2.15: Diagram of jet production in proton-proton collision (through gluon-gluon scattering in this case).

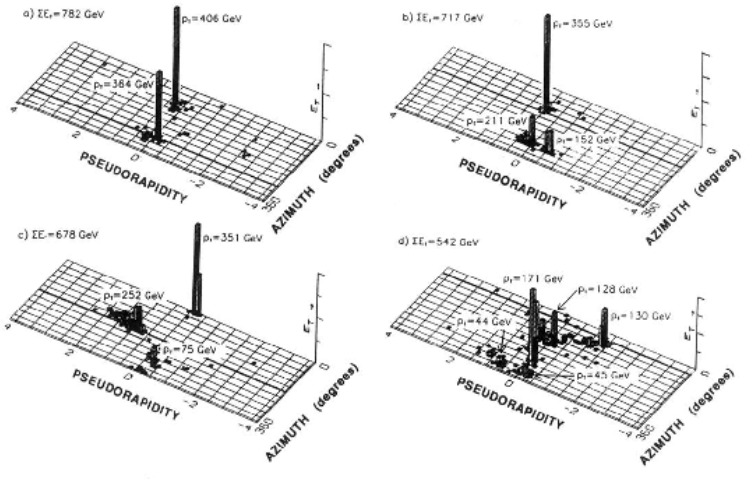

Figure 2.16: Energy flow in the transverse plane for the three events containing the highest total transverse energies [(a)-(c)] observed in the CDF high-$\sum E_T$ data sample, and (d) an example of an event with a complicated jet topology. ([51])

Figure 2.17 shows transverse energy flow etc. in jets measured in proton-antiproton collisions by UA1 Collaboration[52].

To find jets in one proton-proton collision event, a cone algorithm is usually adopted. The distance between a cone axis (η^C, ϕ^C) and the momentum direction of a particle (η^i, ϕ^i) is defined as

$$R^i = \sqrt{(\eta^i - \eta^C)^2 + (\phi^i - \phi^C)^2}, \tag{2.53}$$

and particles with a R^i less than the cone radius R^C are included in the cone to form a jet. The size of the R^C is usually 0.4 to 0.7, which collects about 90% of p_T of a jet on average. Some cone algorithms are described below.

Snowmass algorithm

The Snowmass algorithm was proposed at the Snowmass Workshop[53] in 1990. Momenta of all particles are used as a seed of the cone axis. Particles inside the cone are gathered, and the transverse energy ($E_T^C = E^C \sin\theta^C$) and the centroid $(\bar{\eta}^C, \bar{\phi}^C)$ of the particles in the cone are defined as

$$E_T^C = \sum_{i \in C} E_T^i \ , \quad \bar{\eta}^C = \sum_{i \in C} E_T^i \eta^i / E_T^C \ , \quad \bar{\phi}^C = \sum_{i \in C} E_T^i \phi^i / E_T^C. \tag{2.54}$$

The cone position is replaced with the centroid and the procedure above is iterated until $\eta^C = \bar{\eta}^C$ and $\phi^C = \bar{\phi}^C$ are satisfied.

Due to the use of seed, the algorithm is sensitive to the infrared singularity and the collinear singularity which appear in higher-order pQCD calculations. An example of the sensitivities are illustrated in Fig. 2.18. The algorithm without seed can be realized by, for example, checking whether every possible combination of 2, $3 \ldots N$ particles in one event is in a stable cone or not. But in reality it takes too long calculation time $\mathcal{O}(N2^N)$ to be applied on experimental data.

Midpoint algorithm

The midpoint algorithm[54] has been developed by the CDF experiment based on the Snowmass algorithm. It adds a midpoint between two stable cones that are found with the Snowmass algorithm, and checks whether a cone at the midpoint can be a newly stable cone or not. It avoids most of the infrared sensitivity with rather a short calculation time.

SISCone algorithm

The SISCone (Seedless Infrared Safe Cone) algorithm[55][56] has been proposed recently in 2007. It doesn't use a seed and tries to identify all distinct

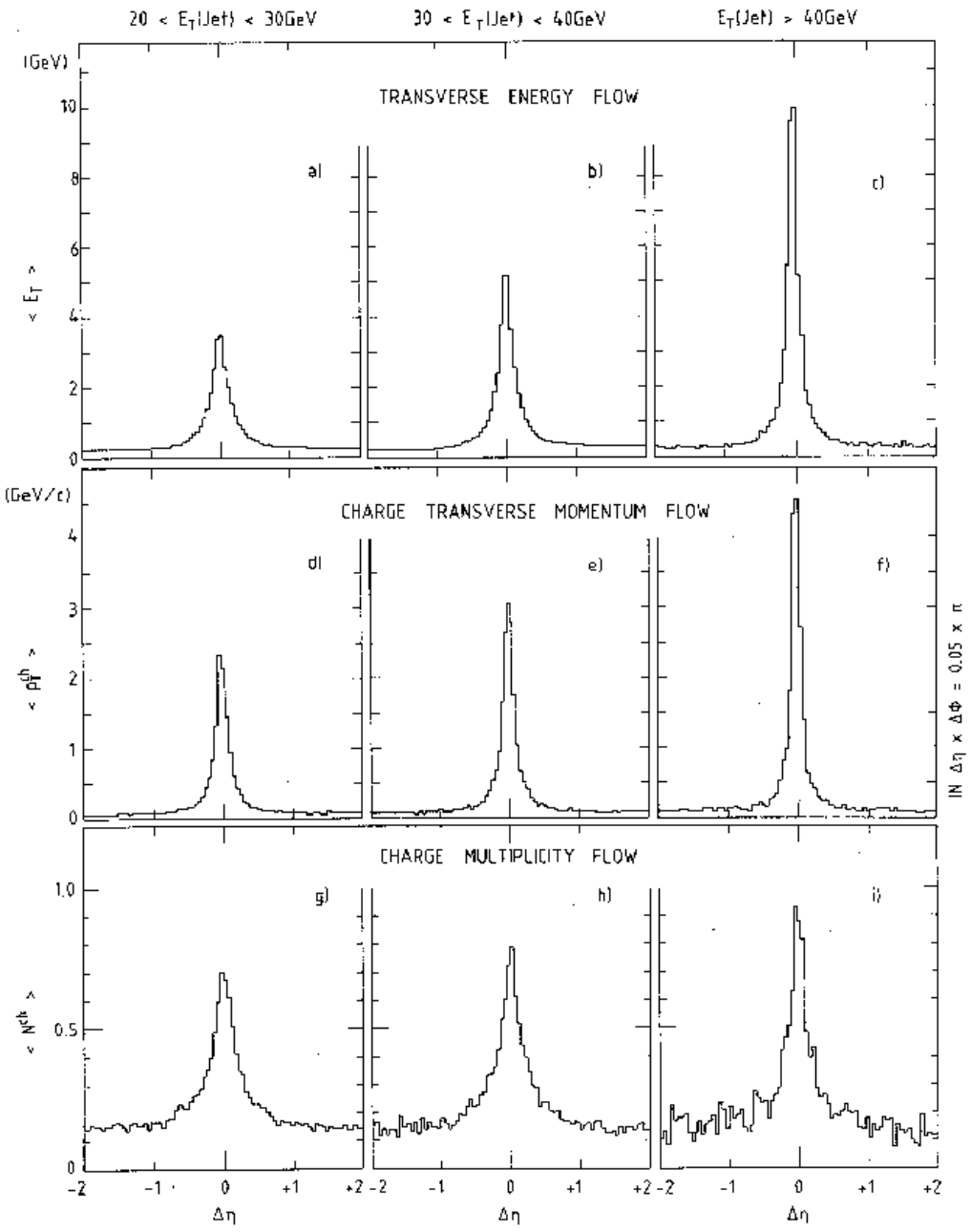

Figure 2.17: (a)-(c): Transverse energy flow as function of $\Delta\eta$, i.e. pseudo-rapidity distance from the jet axis, for 3 slices of jet E_T. The bin width is $d\Delta\eta = 0.05$, azimuthal integration is taken within $\Delta\phi = \pm 90^o$. (d)-(f): Charged transverse momentum flow as function of $\Delta\eta$. (g)-(i): Charged multiplicity flow as function of $\Delta\eta$. ([52])

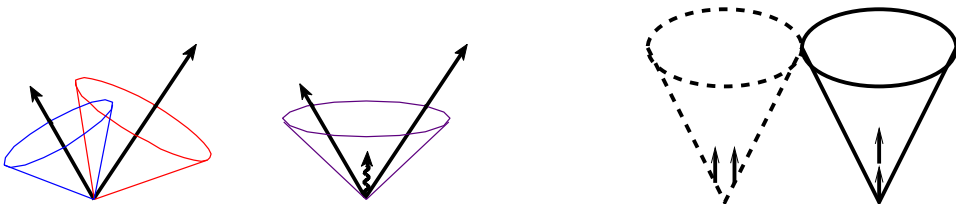

Figure 2.18: **Left**: An illustration of infrared sensitivity in a seed-cone algorithm. The presence of soft radiation between two jets causes a merging of the jets. **Right**: An illustration of collinear sensitivity in a seed-cone algorithm. The collinear splitting causes a disappearance of a seed particle and then a jet[54].

cones, where the "distinct" cone means that it contains its own set of particles. It can be performed with a reasonable calculation time $\mathcal{O}(Nn\ln n)$, where N is the number of particles in an event and n is the typical number of particles in a cone. It is infrared safe because of its seedlessness.

2.2.2 Cross section

The jet cross section has a form similar to Eq. 2.45 except the fragmentation function.

$$\sigma^{pp\to jetX} = \sum_{f_1,f_2,f} \int dx_1 dx_2 f_1(x_1,\mu^2) f_2(x_1,\mu^2) \hat{\sigma}^{f_1 f_2 \to fX'}(x_1 p_1, x_2 p_2, p_{jet}, \mu) \tag{2.55}$$

A calculation of the jet cross section under the condition of the PHENIX experiment ($\sqrt{s} = 200$ GeV, $|\eta| < 0.35$, $R = 1$) has been done by W. Vogelsang in next-leading-order (NLO) pQCD with the Small Cone Approximation (SCA)[57][58]. The jet cross section can be written at the next leading order as

$$\begin{aligned}\frac{d\sigma}{dp_T^{\rm jet} d\eta^{\rm jet}} = \frac{2p_T^{\rm jet}}{S} \sum_{a,b} \int_{VW}^{V} \frac{dv}{v(1-v)} \int_{VW/v}^{1} \frac{dw}{w} f_a(x_a,\mu_F) f_b(x_b,\mu_F) \\ \times \left[\frac{d\hat{\sigma}^{(0)}_{ab\to jetX}(s,v)}{dv} \delta(1-w) + \frac{\alpha_s(\mu_R)}{\pi} \frac{d\hat{\sigma}^{(1)}_{ab\to jetX}(s,v,w,\mu_F,\mu_R;\delta)}{dvdw} \right]\end{aligned} \tag{2.56}$$

where $\delta = R/\cosh(\eta_{\rm jet})$ is the half-aperture of cone; $d\hat{\sigma}^{(0)}_{ab\to jetX}$ and $d\hat{\sigma}^{(1)}_{ab\to jetX}$ are LO and NLO partonic cross sections; V and W are dimensionless kine-

matic variables defined as

$$V \equiv 1 - \frac{p_T^{\rm jet}}{\sqrt{S}} \exp(\eta^{\rm jet}) \ , \quad W \equiv \frac{(p_T^{\rm jet})^2}{SV(1-V)} \tag{2.57}$$

with the proton c.m.s. energy squared $S = (P_a + P_b)^2$; v etc. are parton-level kinematic variables defined as

$$v \equiv 1 + \frac{t}{s} \ , \quad w \equiv \frac{-u}{s+t} \ , \quad s \equiv (p_a + p_b)^2 \ , \quad t \equiv (p_a - P_{\rm jet})^2 \ , \quad u \equiv (p_b - P_{\rm jet})^2 \tag{2.58}$$

where $P_{\rm jet}$ is the four-momentum of jet; x_a and x_b are the Bjorken-x variables and are given by

$$x_a = \frac{VW}{vw} \ , \quad x_b = \frac{1-V}{1-v}; \tag{2.59}$$

f_a and f_b are the PDFs; μ_R and μ_F are the renormalization and factorization scales. Under the SCA, where only collinear final state radiation can contribute to $d\hat{\sigma}^{(1)}_{ab\to jetX}$, the $2 \to 3$ matrix elements factorize into $2 \to 2$ ones and LO splitting functions, and thus the calculation dramatically simplifies and can be done largely analytically.

Figure 2.19 shows the unpolarized jet cross section at a pseudo-rapidity $|\eta| < 0.35$ with a cone radius $R = 1$, which was calculated at NLO under the SCA. The fraction of gg, qg, and qq subprocesses in the jet cross section is shown at the top of Fig. 2.14. At mid-rapidity the gg and qg subprocesses are dominant. The validity of the SCA has been checked by comparing the cross section in the SCA with that in a full Monte-Carlo approach at $5 < p_T^{\rm jet} < 27$ GeV/c and $R = 0.4, 0.7, 1.0$. At the $p_T^{\rm jet}$ range, the ratio $d\sigma$(SCA)/$d\sigma$(full MC) is $\sim$1 for $R = 0.4$, 0.90 to 0.95 for $R = 0.7$ and 0.80 to 0.85 for $R = 1.0$.

2.2.3 Double helicity asymmetry

The jet A_{LL} can be written in analogue to Eq. 2.49 as

$$A_{LL} = \frac{\sum_{f_1,f_2,f} \int dx_1 dx_2 \cdot \Delta f_1 \cdot \Delta f_2 \cdot \hat{\sigma}^{f_1 f_2 \to f X'} \cdot \hat{a}_{LL}^{f_1 f_2 \to f X'}}{\sum_{f_1,f_2,f} \int dx_1 dx_2 \cdot f_1 \cdot f_2 \cdot \hat{\sigma}^{f_1 f_2 \to f X'}} \tag{2.60}$$

A jet A_{LL} calculation under the condition of the PHENIX experiment has been done also based on the SCA[58]. Figure 2.20 shows the jet A_{LL} with four assumed $\Delta g(x)$. Jets at mid-rapidity are produced mainly via gg and qg subprocesses, and each subprocess has a different magnitude of A_{LL} as shown in Fig. 2.21.

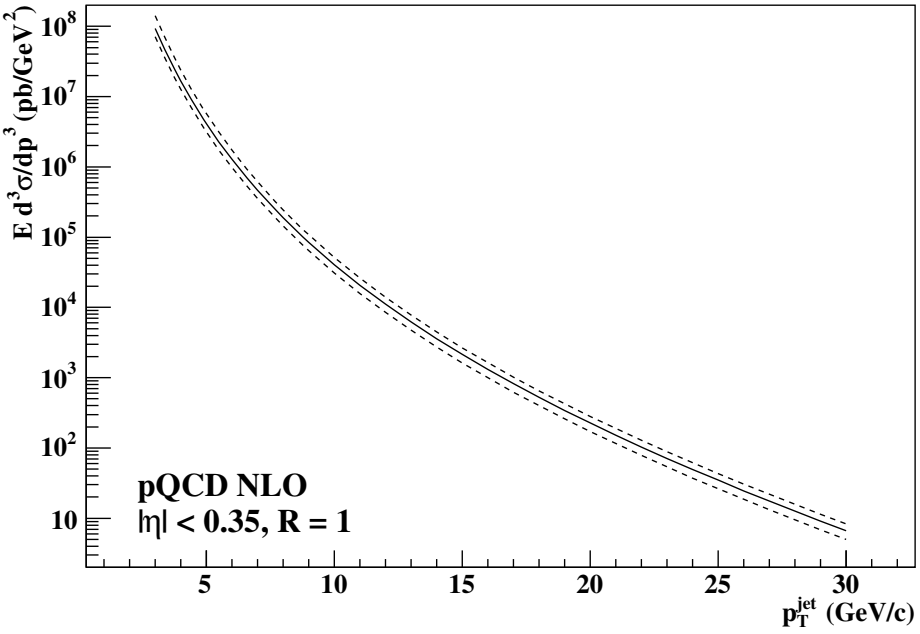

Figure 2.19: Unpolarized jet cross section at a pseudo-rapidity $|\eta| < 0.35$ with a cone radius $R = 1$. It was calculated at NLO under the SCA with three factorization scales, $\mu = p_T$ (**Solid line**), $2p_T$ (**Lower dashed line**) and $p_T/2$ (**Upper dashed line**).

As well as the unpolarized cross section, the validity of the SCA has been checked by comparing the polarized cross section in the SCA with that in a full MC approach at $5 < p_T^{\rm jet} < 27$ GeV/c and $R = 0.4, 0.7, 1.0$. At the $p_T^{\rm jet}$ range, the ratio $d\Delta\sigma$(SCA)/$d\Delta\sigma$(full MC) is 1.0 to 1.1 for $R = 0.4$, 0.90 to 1.0 for $R = 0.7$ and 0.85 to 0.90 for $R = 1.0$. Then, the ratio A_{LL}(SCA)/A_{LL}(full MC) is $\sim$1.1 at $p_T^{\rm jet} = 5$ GeV/c and $\sim$1.0 at $p_T^{\rm jet} = 27$ GeV/c for the three cone sizes.

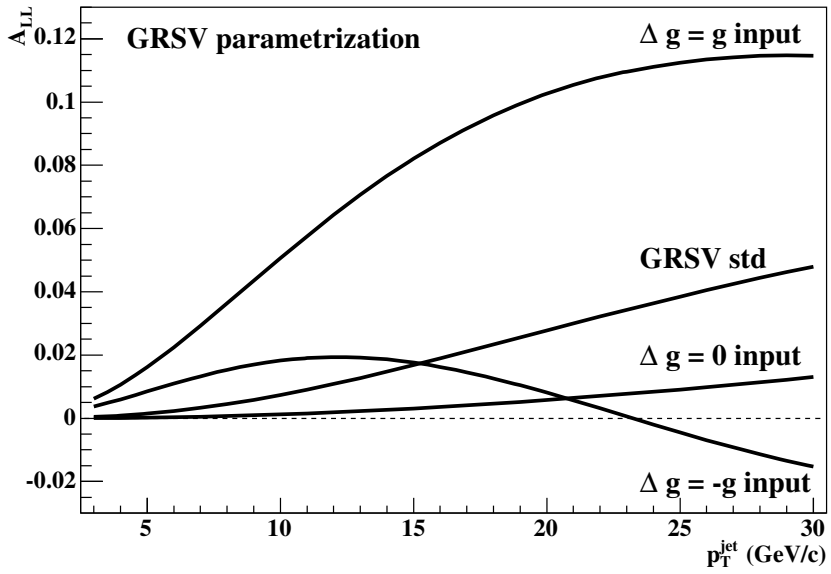

Figure 2.20: A_{LL} of jet production at the pseudo-rapidity $|\eta| < 0.35$ with a cone size of $R = 1.0$. It was calculated at NLO under the SCA.

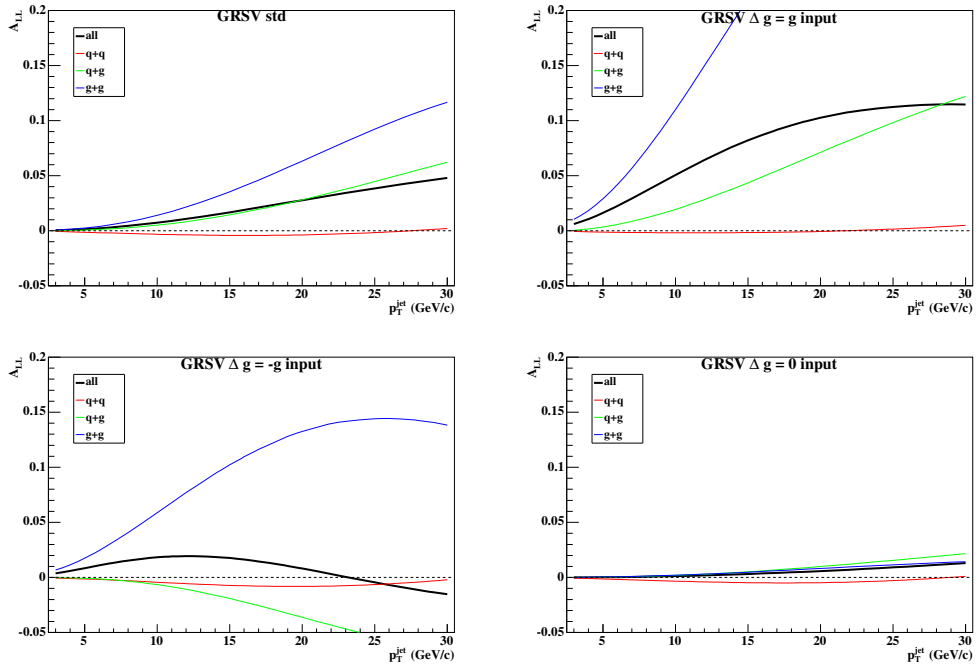

Figure 2.21: A_{LL} of gg, qg, and qq subprocesses with four $\Delta g(x)$ scenarios.

Chapter 3

Experimental Setup

3.1 Accelerator

The Relativistic Heavy Ion Collider (RHIC) at Brookhaven National Laboratory is a unique machine for polarized proton-proton collision. Figure 3.1 shows the schematic layout of the RHIC accelerator complex which is relevant to polarized proton-proton collisions. The RHIC Spin Collaboration aims to investigate the characteristics of the proton spin structure using polarized proton-proton collisions. Polarized protons are generated at a polarized ion source and are accelerated via RFQ, Linac, AGS and RHIC up to $\sqrt{s} = 200$ GeV or 500 GeV. Two experiments, the PHENIX and the STAR, are now being carried out at RHIC.

3.1.1 Polarized proton source

The RHIC utilizes an Optically Pumped Polarized Ion Source (OPPIS)[59]. Figure 3.2 is the general layout of the BNL OPPIS. In a strong magnetic field a left-circulated laser pumps up an electron of Rb atoms to the higher Zeeman-split state and makes electrons of Rb atoms polarized. H^+ ions are injected into the Rb gases in the direction parallel to the magnetic field and picks up polarized electron of Rb atoms to form H^0s. The electron polarization transfers to the protons by the Sona type diabatic (slow) transition in the zero-magnetic-field space. H^0s pass through a Na gas volume where a strong magnetic field is applied in the direction anti-parallel to the first magnetic field, to strip electrons and form H^-s. The direction of the H^- polarizations can be reversed by changing the direction of the magnetic fields. A polarization of $\sim 90\%$ has been achieved in 2007.

The polarized H^- beams are accelerated by a Radio Frequency Quadrapole (RFQ) accelerator up to 75 keV, by a Linac up to 200 MeV and by a Booster

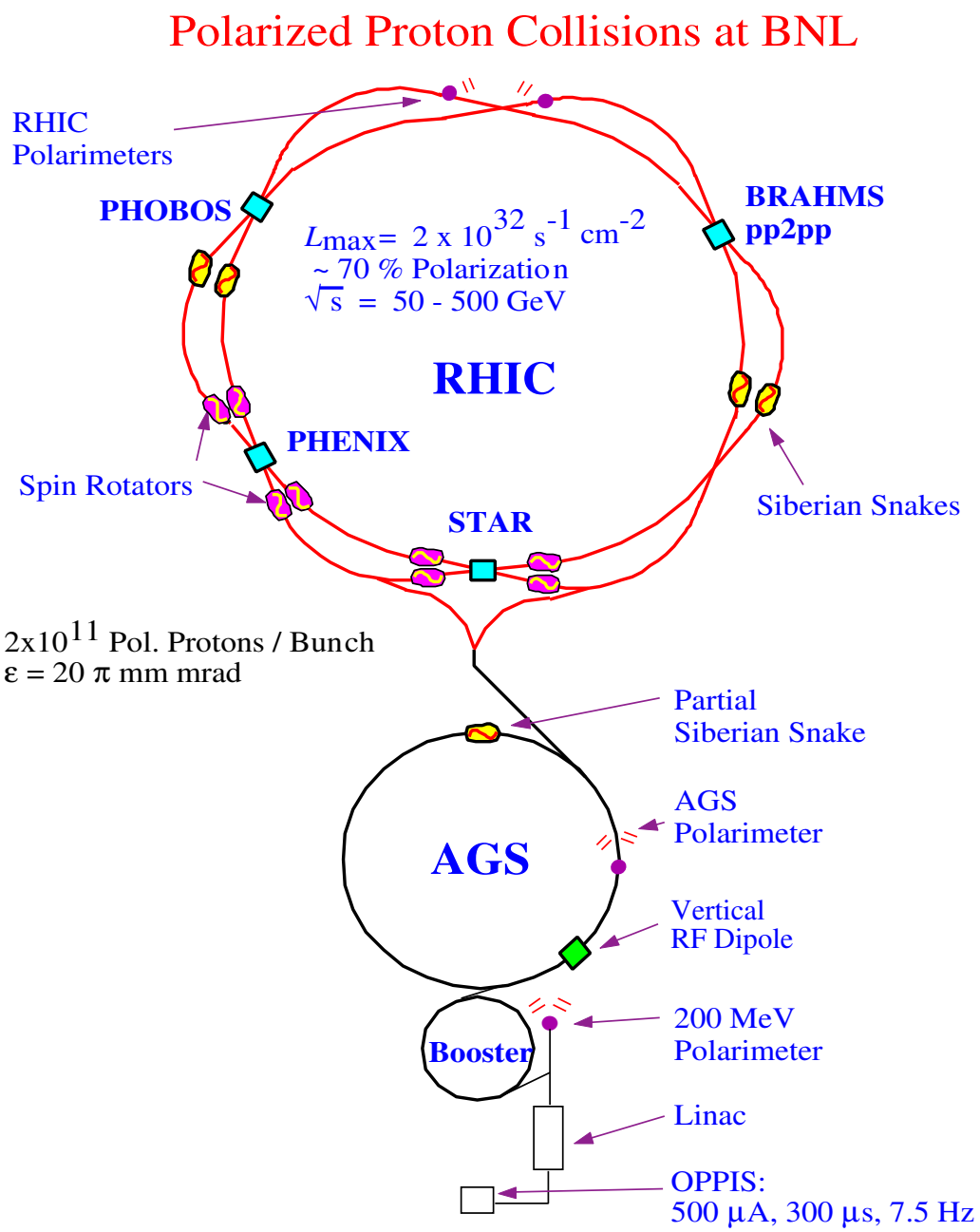

Figure 3.1: Schematic layout of the RHIC accelerator complex which is relevant to polarized proton-proton collisions[48].

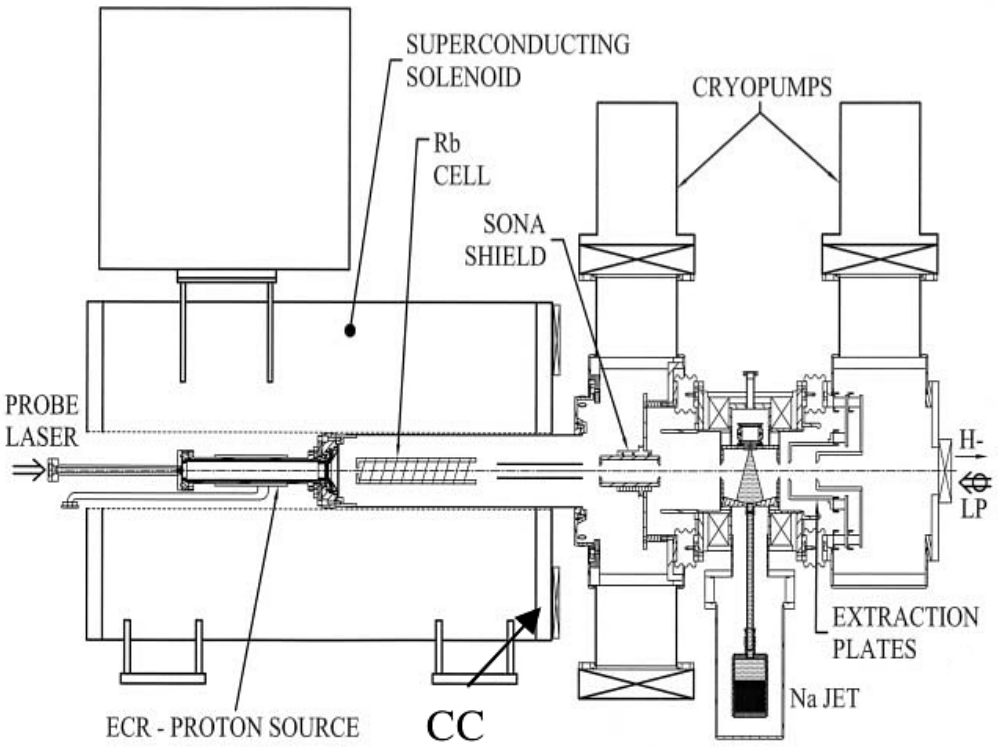

Figure 3.2: The general layout of the BNL OPPIS[60].

up to a kinetic energy of 1.52 GeV. They are strip-injected into the AGS synchrotron and are accelerated up to 24.2 GeV. In the Booster, AGS and RHIC the direction of the proton polarization is vertical.

3.1.2 RHIC

The RHIC is composed of two separate beam pipes called "blue ring" and "yellow ring", in which ions circulate clockwise and counterclockwise, respectively. The circumference of the RHIC is 3.83 km. Polarized protons in the AGS are slow-extracted by a kicker magnet and are injected first into the blue ring and then the yellow ring. The beams are accelerated up to 100 GeV. There are six beam interaction points called "2 o'clock", "4 o'clock" ... "12 o'clock". The PHENIX experiment and the STAR experiment are located at the 8 o'clock and the 6 o'clock, respectively. The number of bunches stored in RHIC at a time is 120 and the interval between the bunches is 31.9 cm or 106 ns. The number of bunches that are actually filled with ions was typically 55 at the beginning of year 2005 and 111 at the end of 2005 and in 2006. A set of beam injection, acceleration, store and dump is called a "fill". The polarization directions of the filled bunches are made different in each fill so that all four polarization patterns in a collision ($++$, $+-$, $-+$ and $--$) take place. Four polarization orders, such as $++--++--\cdots$ for blue-ring bunches and $+-+-+-+-\cdots$ for yellow-ring bunches, are used in each fill to avoid possible bunch-dependent systematic errors. One fill lasts typically 4$\sim$8 hours.

3.1.3 Beam luminosity

The luminosity of two colliding beams, whose beam profiles are assumed to be Gaussian, is given by

$$L = \frac{f_{rev} N_B N_Y}{2\pi \sigma_x \sigma_y} \tag{3.1}$$

$$\sigma_x = \sqrt{\sigma_{xB}^2 + \sigma_{xY}^2} \tag{3.2}$$

$$\sigma_y = \sqrt{\sigma_{yB}^2 + \sigma_{yY}^2} \tag{3.3}$$

where f_{rev} is the frequency of the beam revolution (78 kHz), namely the frequency of the crossing of each bunch pair; N_B and N_Y are the numbers of ions stored in the blue and yellow rings, respectively; σ_x and σ_y are the width in x and y direction of collisions between the two beams. They are represented with the widths of the blue beam (σ_{xB}, σ_{yB}) and the yellow beam

(σ_{xB}, σ_{yB}) at the collision point. The luminosity is obtained by measuring all the values as described below.

The number of ions (N_1 and N_2) are measured with two types of equipments; the Direct Current Current Transformer (DCCT) and the Wall Current Monitor (WCM). The DCCT is a high-permeability copper toroidal coil and has been installed in both the blue and yellow rings near the 2 o'clock interaction point. It measures the electric current induced in itself by the beam current and can precisely determine the integral of beam current during $\sim$1 sec with an accuracy of $\approx 0.2\%$. Due to the long integral time, it doesn't distinguish bunched and debunched ions. The WCM is a large-RLC circuit placed between two adjacent insulated barrels of the beam pipe and has been installed in both the blue and yellow rings near the 2 o'clock interaction point. It measures, with a sampling time of $\sim$0.25 nsec, the voltage across the circuit that is caused by an image charge dragged by the beam current on the beam pipe. It is not as precise as the DCCT but can distinguish bunched and debunched ions because of its short sampling time. A possible contribution of debunched ions is checked with the comparison between the two measurements.

The widths of the beams (σ_{xB} etc.) are measured with the Vernier scan method[61]. When the offset (dx) of two colliding beams in x direction become non-zero, the luminosity varies as

$$L(dx) = \frac{f_{rev} N_B N_Y \exp\left(-dx^2/2\sigma_x^2\right)}{2\pi\sigma_x\sigma_y^2} \tag{3.4}$$

First, any trigger in the PHENIX DAQ needs to be selected, whose trigger rate is proportional to $L(dx)$. Then the trigger rates are measured as a function of dx, while the RHIC control room moves the x position of one beam stepwise. Since the efficiency of the trigger doesn't depend on dx, the width of the trigger rate distribution is equal to σ_x.

3.1.4 Beam polarization

The evolution of the spin direction of polarized protons in an external magnetic field such as what exists in a circular accelerator is governed by the Thomas-BMT equation,

$$\frac{d\boldsymbol{P}}{dt} = -\frac{e}{\gamma m}\left[G\gamma\boldsymbol{B}_\perp + (1+G)\boldsymbol{B}_\parallel\right] \times \boldsymbol{P} \tag{3.5}$$

where $\boldsymbol{P}$ is polarization vector expressed in the frame that moves with the proton, $G = 1.7928$ is the anomalous magnetic moment of the proton, and

$\gamma = E/m$. This expression is similar to the Lorentz force equation that governs the evolution of the orbital motion in an external magnetic field,

$$\frac{d\boldsymbol{v}}{dt} = -\frac{e}{\gamma m}\boldsymbol{B}_{\perp} \times \boldsymbol{v}. \tag{3.6}$$

The spin rotates $G\gamma$ times faster than the orbital motion. Thus $G\gamma$ is called spin tune ν_{sp} since it means the number of spin precessions per orbital rotation.

There are many sources of depolarization during acceleration. Any depolarization is caused by small horizontal magnetic fields, which move spin away from the stable vertical direction. Two main sources are an imperfection resonance and an intrinsic resonance. The imperfection resonance is due to horizontal fields caused by magnet errors and misalignments and arises when $\nu_{sp} = n$, where n is an integer. The intrinsic resonance is due to horizontal focusing fields (it is intrinsic to stable acceleration) and arises when $\nu_{sp} = kP \pm \nu_y$, where k is an integer, P is the super-periodicity (= 12 for AGS and = 3 for RHIC), which is given by the number of identical periods of the accelerator, and ν_y is the vertical betatron tune (= 8.75 for AGS and = 29.23 for RHIC). When a polarized beam is accelerated through an resonance, the final polarization is given by

$$\frac{P_f}{P_i} = 2\exp\left(-\frac{\pi\left|\epsilon\right|^2}{2\alpha}\right) - 1, \tag{3.7}$$

where P_i and P_f are the polarization before and after the resonance crossing, ϵ is the resonance strength[62][63] obtained from the spin rotation of the driving fields and is shown in Fig. 3.3, and α is the change of the spin tune per radian of the orbit angle. At RHIC, the depolarization resonances are avoided using spin rotation magnets called "Siberian Snake". The Siberian Snake rotates the spin by 180° around the horizontal axis. It makes the stable spin direction unperturbed at all time as long as the spin rotation from the Siberian Snake is much larger than that from the resonance driving fields. At AGS, two Siberian Snakes that rotates the spin partially (not 180°) are adopted.

Spin rotators are placed upstream and downstream of the collision points for both the blue and yellow beams. They make it possible to collide protons with longitudinal polarization as well as transverse polarization.

The beam polarization at RHIC is measured using two polarimeters at the 12 o'clock; the pC polarimeter and the H-jet polarimeter. The pC polarimeter utilizes the left-right asymmetry in the cross section of polarized proton-carbon scattering ($\vec{p}C \to \vec{p}C$) at the Coulomb Nuclear Interference

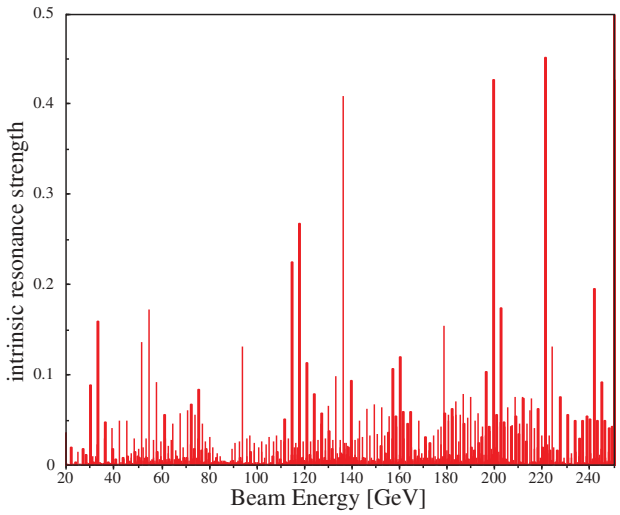

Figure 3.3: RHIC intrinsic spin resonance strength as a function of beam energy[62].

kinematic region ($0.001 \lesssim |t| \lesssim 0.01(\mathrm{GeV}/c)^2$)[64]. The polarized proton is the beam stored in RHIC, and the carbon is a ribbon of a $\sim$5 μm width and a $\sim$5 μg/cm^2 thickness and is inserted into the RHIC beams during polarization measurements. Since the carbon is a solid target, the scattering rate is large enough to precisely measure the asymmetry in a few minutes and thus the beam polarization is usually measured two or three times per fill using the pC polarimeter. But the systematic error of the polarization measurement is 20% mainly due to an uncertainty on the measurement of recoil carbon energy. The H-jet polarimeter utilizes the left-right asymmetry in the cross section of polarized proton-proton scattering ($\vec{p}p \to \vec{p}p$) at the CNI region[65]. The (unpolarized) proton target is a hydrogen-gas jet (H-jet) that is sprayed downward across the RHIC beams all the time. The scattering rate is too small to determine a beam polarization fill-by-fill. The H-jet is also polarized and its polarization is measured with a 2% accuracy with a Breit-Labi polarimeter placed downstream of the H-jet. The systematic errors in the left-right asymmetry for the determination of the proton beam polarization (ϵ_L^{beam}) and the H-jet polarization (ϵ_L^{target}) cancel out since the detector used is common. Therefore the beam polarization can be determined precisely as

$$P_{beam} = \frac{\epsilon_L^{beam}}{\epsilon_L^{target}} \cdot P_{target} \tag{3.8}$$

At present a 5% accuracy has been achieved.

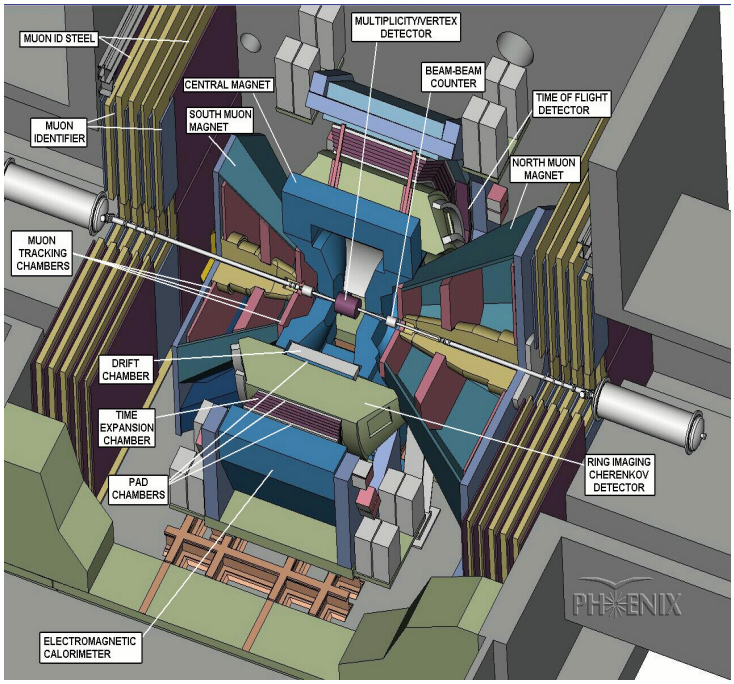

Figure 3.4: The schematic drawing of PHENIX detector.

The polarizations of the blue and yellow beams measured with the CNI polarimeter and the pattern of spin directions of all bunches are provided by the RHIC control room for all experiments during collisions via a hardware called "Common Device (CDEV)".

3.2 PHENIX detector overview

The PHENIX detector[66] can be grouped into three parts; the Inner Detectors, the Central Arms and the Muon Arms. Figure 3.4 is a schematic drawing and Fig. 3.5 is cross sections in the beam view and the side view. Figure 3.6 shows the magnetic field lines formed by four magnets called Central Magnet Inner (CMI), Central Magnet Outer (CMO), Muon Magnet North (MMN) and Muon Magnet South (MMS).

The Inner Detectors include the Beam-Beam Counters (BBC) and the Zero-Degree Calorimeters (ZDC). The BBC measures the number of charged particles in forward and backward regions to determine collision time, collision z-vertex, and beam luminosity. The ZDC measures neutrons in forward and backward regions and is used as a local polarimeter, which assures that

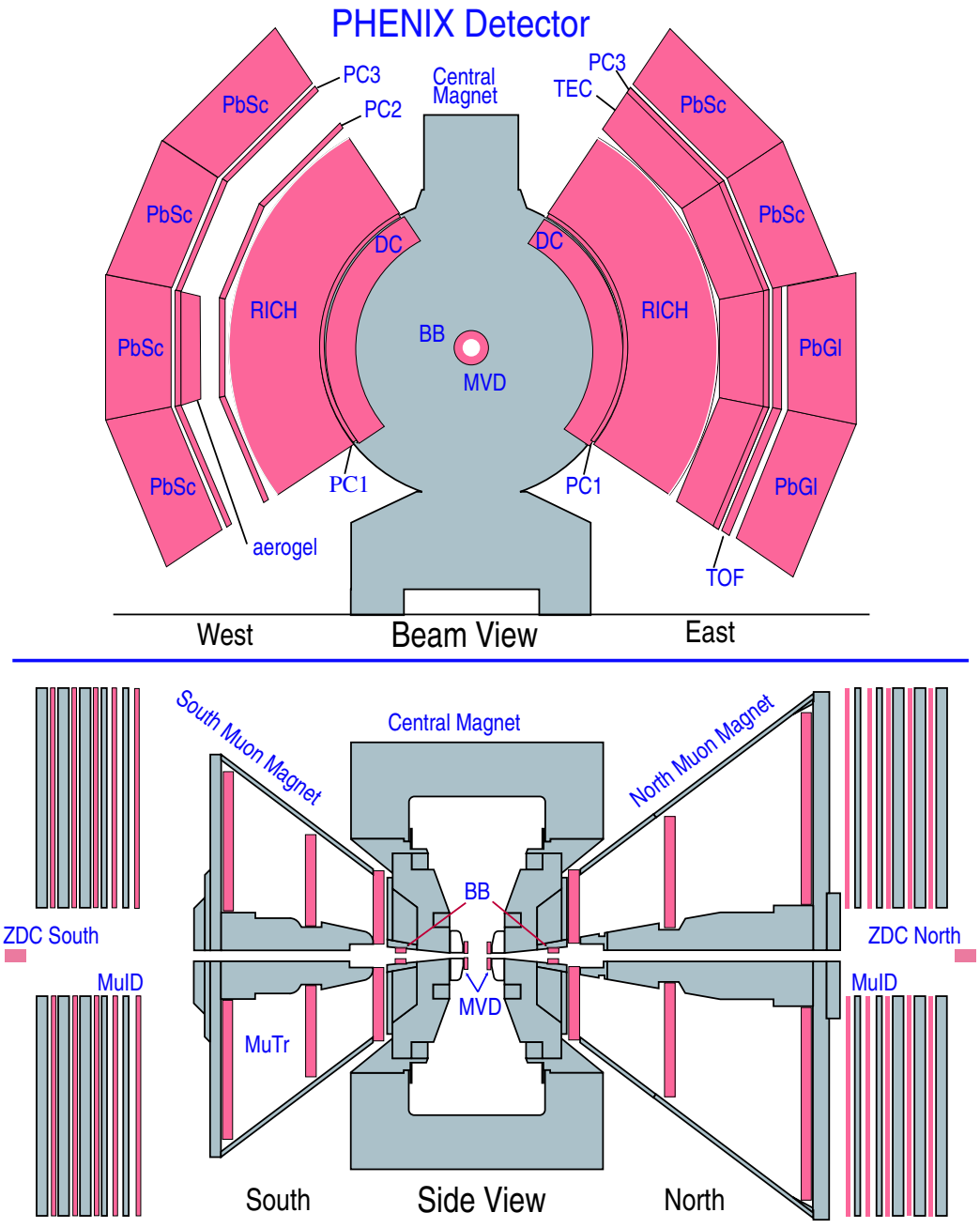

Figure 3.5: The cross sections of PHENIX detector.

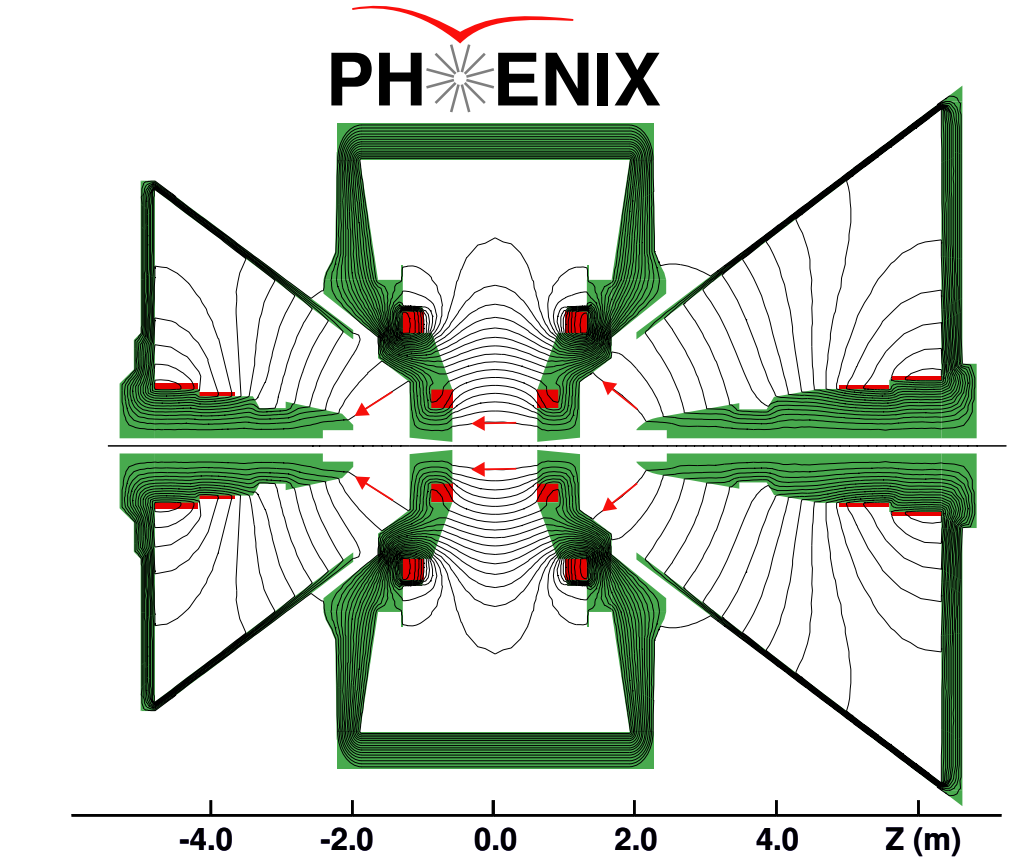

Figure 3.6: The PHENIX magnetic fields.

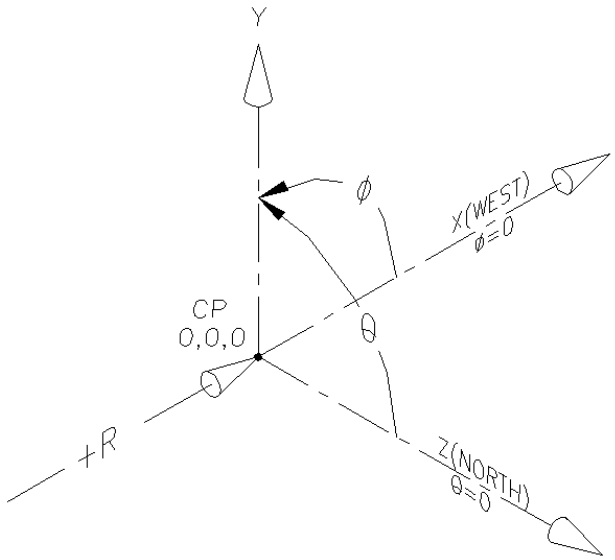

Figure 3.7: The PHENIX coordinate system.

the beam polarization is correctly longitudinal or transverse at the interaction region by observing the left-right asymmetry in the $\vec{p}+p \rightarrow \text{neutron}+X$ scattering cross section[67].

The Central Arms have a tracking system and an Electro-Magnetic Calorimeter (EMCal). The tracking system consists of Pad Chambers (PC), Drift Chambers (DC), Ring-Imaging Cherenkov (RICH) detectors, etc. The PC and DC measure the track information of charged particles, and the RICH and other detectors are used for identifying the type of charged particles. The EMCal measures the position and energy of photons and electrons.

The Muon Arms have the Muon Trackers (MuTr) and the Muon Identifiers (MuID). The MuTr consists of three multi-plane drift chambers, and the MuID consists of alternating layers of steel absorbers and Iarocci-type streamer tubes.

Fig. 3.5 shows the PHENIX coordinate system. The z axis is along the beam direction. The x and y axes are in horizontal and vertical directions, respectively. $+x$, $+y$ and $+z$ directions point to the West Arm, the top and the North Arm, respectively.

Table 3.1 summarizes the coverage of the main PHENIX detector subsystems. In the subsections below, subsystems used in this analysis are explained in detail. Particularly I have performed two experimental tasks related to the EMCal of the Central Arms. One is an energy calibration of every EMCal module using π^0 invariant mass peak. It checked that each EMCal mod-

Table 3.1: Coverage of the main PHENIX Detector Subsystems. $\Delta\eta$ is the pseudo-rapidity coverage, and $\Delta\phi$ is the azimuthal angle coverage.

Element	$\Delta\eta$	$\Delta\phi$
Magnet: central (CM)	± 0.35	360^o
muon (MMS)	$-1.1 \sim -2.2$	360^o
muon (MMN)	$1.1 \sim 2.4$	360^o
Beam-beam (BBC)	$\pm(3.1 \sim 3.9)$	360^o
ZDC	± 2 mrad	360^o
Drift chambers (DC)	± 0.35	$90^o \times 2$
Pad chambers (PC)	± 0.35	$90^o \times 2$
TEC	± 0.35	$90^o \times 2$
RICH	± 0.35	$90^o \times 2$
ToF	± 0.35	$45^o \times 2$
T0	± 0.35	$45^o \times 2$
PbSc EMCal (East)	± 0.35	45^o
PbSc EMCal (West)	± 0.35	90^o
PbGl EMCal (East)	± 0.35	45^o
Muon tracker (South)	$-1.15 \sim -2.25$	360^o
Muon tracker (North)	$1.15 \sim 2.44$	360^o
Muon identifier (South)	$-1.15 \sim -2.25$	360^o
Muon identifier (North)	$1.15 \sim 2.44$	360^o

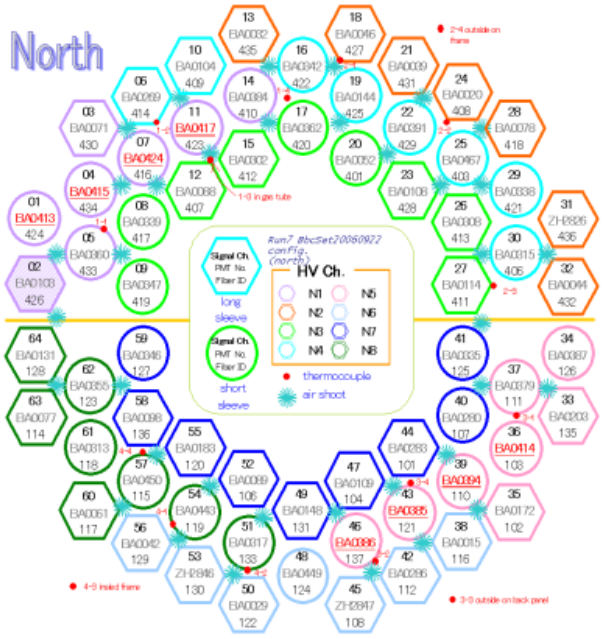

Figure 3.8: The arrangement of detection modules in BBC North.

ule had a expected gain and also adjusted a tower-to-tower gain fluctuation. The methods and results of the energy calibration is described in the chapter "Analysis Methods". The other is a development of ERT, which is a high-energy-photon trigger of the EMCal. Pedestal levels of each trigger module are different, and thus are measured module-by-module in order to achieve a uniform trigger-energy threshold. I have developed a fast program that measured a pedestal level of every trigger modules. It enabled us to adjust the pedestal levels frequently enough.

3.3 Beam-beam counter (BBC)

The BBC is two identical sets of counters placed at both the north and south sides of the collision point[68]. The distance between the collision point and the BBC is 144 cm. Each counter is composed of 64 one-inch diameter mesh-dynode PMTs (Hamamatsu R6178) equipped with 3 cm quartz as a Cherenkov radiator. Figure 3.8 shows the arrangement of the pairs of the quartz and the PMT in the BBC North. The outer and inner diameters are 30 cm and 10 cm, respectively, and it covers a pseudo-rapidity of $3.0 < |\eta| < 3.9$ over the full azimuth. The gain of each PMT is adjusted using a MIP

(minimum ionizing particle) peak in pulse height distribution. During data taking, timing drifts of each element are monitored and calibrated using a laser signal.

The BBC measures the number of charged particles in forward and backward regions to determine the collision time, collision z-vertex, and beam luminosity. The hit timing (T_N and T_S) of each BBC is defined as the average of hit times of all the modules in each side. The time (T_0) and z-vertex (z_{BBC}) of a collision is then determined as

$$T_0 = \frac{T_S + T_N}{2} - \frac{L}{c} \tag{3.9}$$

$$z_{BBC} = \frac{c(T_S - T_N)}{2} \tag{3.10}$$

where $L = 144$ cm is the distance between collision point and the BBC. The resolutions of T_0 and z_{BBC} in proton-proton collisions are ~ 20 ps and $2 \sim 3$ cm, respectively.

3.4 Zero degree calorimeter (ZDC)

The ZDC is two sets of hadronic calorimeters placed at the north and south sides of the collision points with a distance of 18 m[69]. Figure 3.9 shows the mechanical design of a ZDC module, and three modules per side are placed along the beam direction. It covers a 10 cm $\times$ 10 cm area perpendicular to the beam direction, which corresponds to 2.8 mrad when viewed from the collision point. It consists of alternating layers of tungsten absorbers and sampling fibers, and has 150 radiation length and 5.1 interaction length. Before the ZDC, a DX dipole magnet is located to bend the beams in RHIC. Therefore charged particles are swept out by the magnetic fields. A counter made of plastic scintillator is placed in front of the ZDC to veto charged particles coming from the collision point.

The Shower Maximum Detector (SMD) is inserted between the first and second ZDC modules to determine the hit position of neutrons. It consists of 16 scintillator hodoscopes; eight in vertical and eight in horizontal. The position of an incident neutron is evaluated as the centroid of deposit energies in the hodoscopes.

3.5 Electromagnetic calorimeter (EMCal)

The EMCal system is located at a 5 m distance from the beam pipe to measure the position and energy of mainly photons and electrons[70]. The

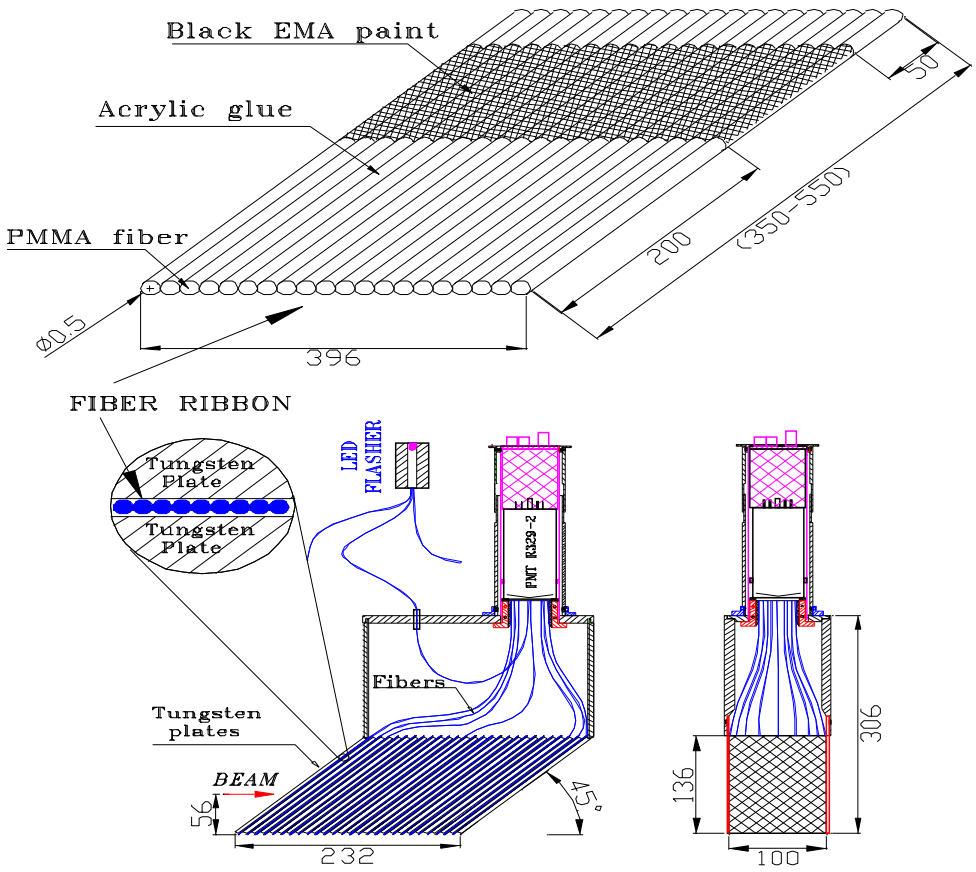

Figure 3.9: Mechanical design of the production Tungsten Modules. Dimensions shown are in mm. ([69])

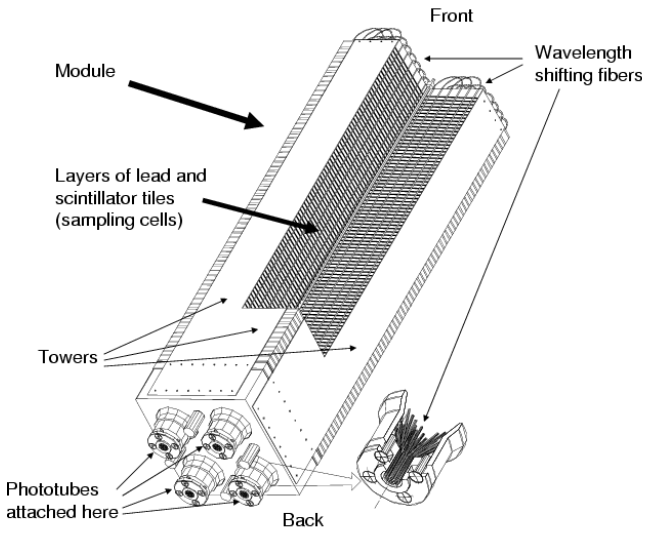

Figure 3.10: The construction of the PbSc module.

system consists of four sectors in each of the East and West Arms, and each sector has a size of 2×4 m^2. The system is composed of two-type towers; one is PbSc used in all the four sectors in the West Arms (called W0, W1, W2 and W3 from bottom to top) and two upper sectors in the East Arms (called E2 and E3 from bottom to top), and the other is PbGl used in two lower sectors in the East Arms (called E0 and E1 from bottom to top).

The **PbSc** is a sampling calorimeter read out by PMT. It consists of alternating layers of lead absorbers and scintillators. A tower of the PbSc has a size of 5.535×5.535×37.5 cm^3 (see Fig. 3.10) and a 18 radiation length. It consists of 66 cells of a 0.15 cm Pb and a 0.41 cm scintillator. 36 wavelength-shifting fibers penetrates all cells, where each fiber is loop-backed at the front of the tower so that it penetrates all cells twice, and guide light signals to the PMT. The Moliere radius is $\sim$ 30 mm. One sector is composed of 72×36 towers. The resolutions of energy (σ_E) and position (σ_x) are given by

$$\frac{\sigma_E}{E}(\%) = \frac{8.1}{\sqrt{E(\mathrm{GeV})}} \oplus 2.1 \tag{3.11}$$

$$\sigma_x(E,\theta)(mm) = \sigma_x^0(E) \oplus \Delta \sin(\theta) \tag{3.12}$$

$$\sigma_x^0(E)(mm) = 1.55 \oplus \frac{5.7}{\sqrt{E(\mathrm{GeV})}} \tag{3.13}$$

where θ is the incident angle of photons against the detector surface and Δ is the radiation length. The energy resolution is shown in Fig. 3.11.

The **PbGl** is a homogeneous calorimeter made of lead-glass Cherenkov radiator read out by PMT. A tower of the PbGl has a size of $4\times4\times40$ cm^3 and a 14.4 radiation length. The Moliere radius is 37 mm. One sector is composed of 96×48 towers. The resolutions of energy (σ_E) and position (σ_x) have been measured with electron test beams and are given by

$$\frac{\sigma_E}{E}(\%) = \frac{5.9}{\sqrt{E(\mathrm{GeV})}} \oplus 0.8 \tag{3.14}$$

$$\sigma_x(E,\theta)(mm) = \sigma_x^0(E) \oplus \Delta\sin(\theta) \tag{3.15}$$

$$\sigma_x^0(E)(mm) = 0.2 \oplus \frac{8.4}{\sqrt{E(\mathrm{GeV})}} \tag{3.16}$$

where θ is the incident angle of photons against the detector surface and Δ is the radiation length. The energy resolution is shown in Fig. 3.11.

Energies deposited by photons over some towers are clustered to reconstruct the energies of the original photons using a method below, which is almost common to the PbSc and PbGl. Only towers whose detected energy is above a threshold are used in the clustering. The energy thresholds of the PbSc and PbGl tower are 10 MeV and 14 MeV, respectively. Neighboring towers that have an energy above the threshold are gathered to form a first-level cluster, which may be made by more than one photons. In the first-level cluster, local maxima (in space) of deposited energies are found, and the first-level cluster is divided into the number of the local maxima. The energy deposited in a tower between the local maxima is shared according to the breakdown of the deposited energy that is predicted from the energies of the local maxima and the shape of the electromagnetic shower. The energy of a PbGl cluster is the energy sum of all towers in the cluster. The energy of a PbSc cluster is the energy sum of "core" towers in the cluster, where the "core" tower means the towers where the deposit energy predicted from the tower energy at cluster center is >2% of the measured cluster energy. The ratio of core energy to total energy is 91.8% on average and weakly depends on energy. The energy of a cluster is corrected for incident angle and energy non-linearity based on the studies with test beam experiments and GEANT simulations. The energy non-linearity is caused by energy leakage and, only for the PbSc, light attenuation in the wave-length-shifting fiber. Figure 3.12 shows the correction functions for these effects.

The shape of a cluster, namely the spacial distribution of tower energies in a cluster, is parameterized into a value "photon probability", which represents the probability that the cluster is made by a photon. It is a confidence

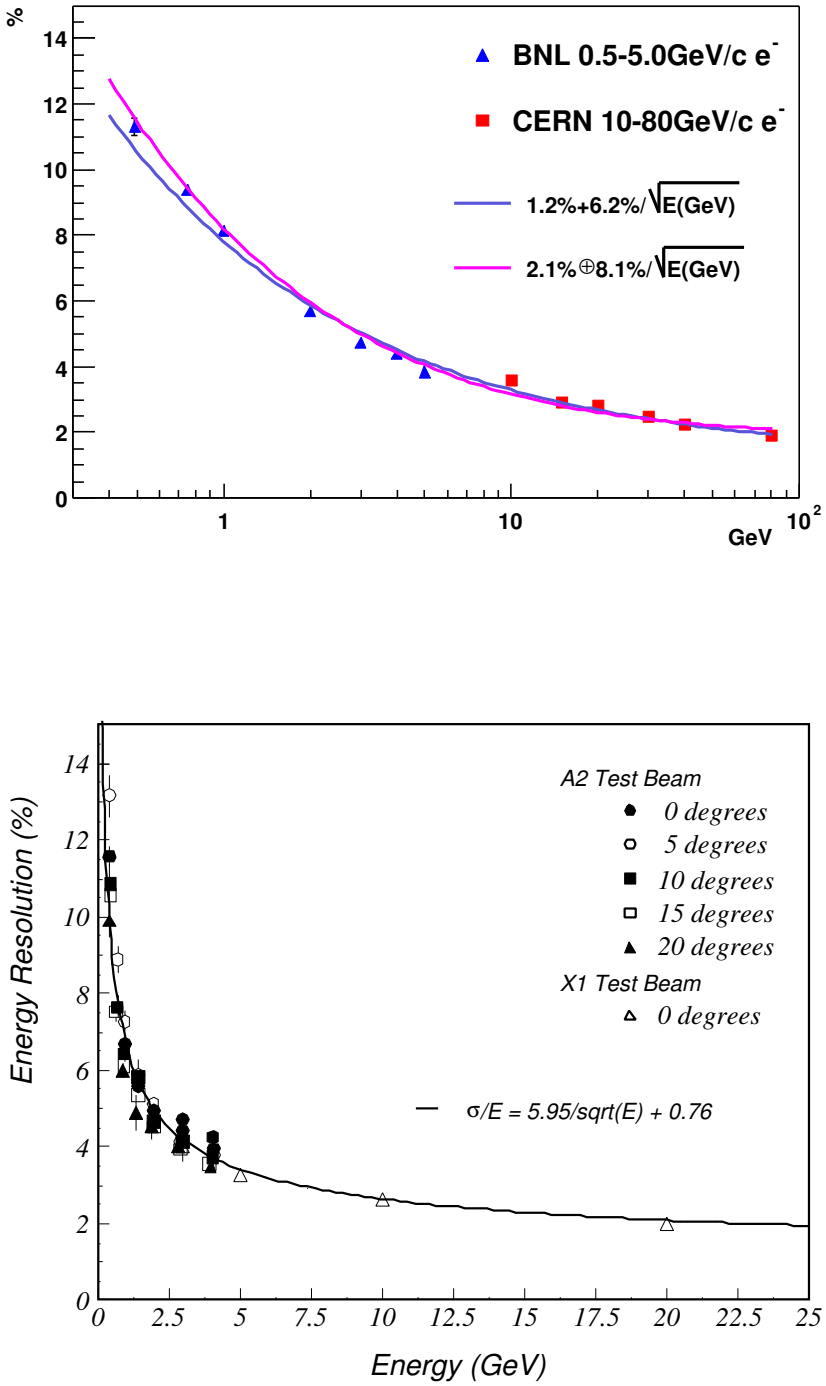

Figure 3.11: EMCal energy resolution (**Top**: PbSc, **Bottom**: PbGl) measured with test beam experiments.

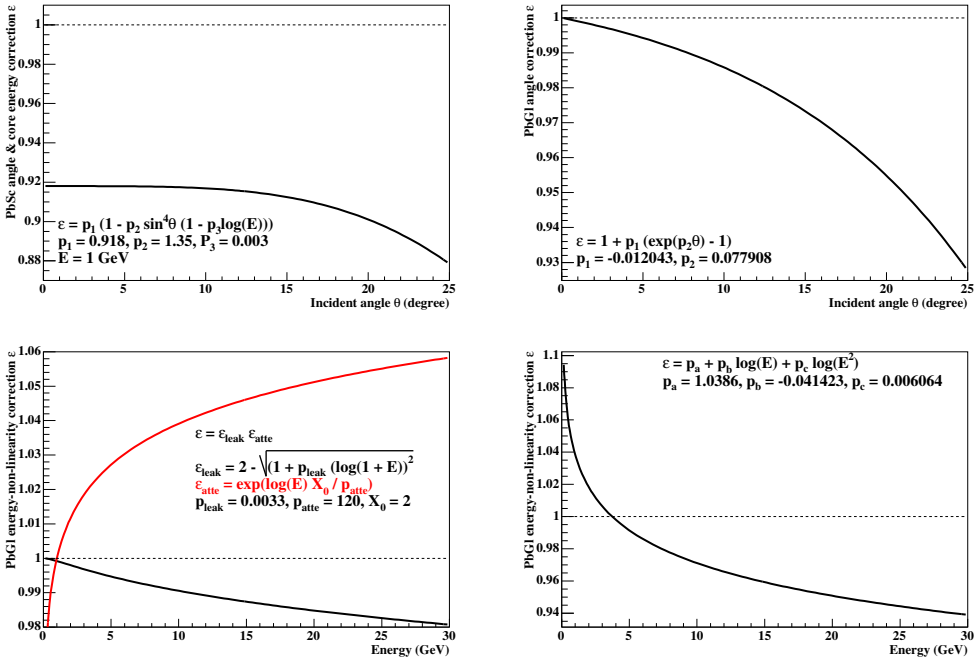

Figure 3.12: EMCal energy correction. The angle dependence is corrected as $E' = E/\epsilon_{angle}$, and then the non-linearity is corrected as $E'' = E'/\epsilon_{nonl}$. The horizontal axis in the bottom two plots is the energy that has already been corrected for the angle dependence. The correction for the angle dependence of the PbSc includes the ratio of core energy to total energy, 91.8%.

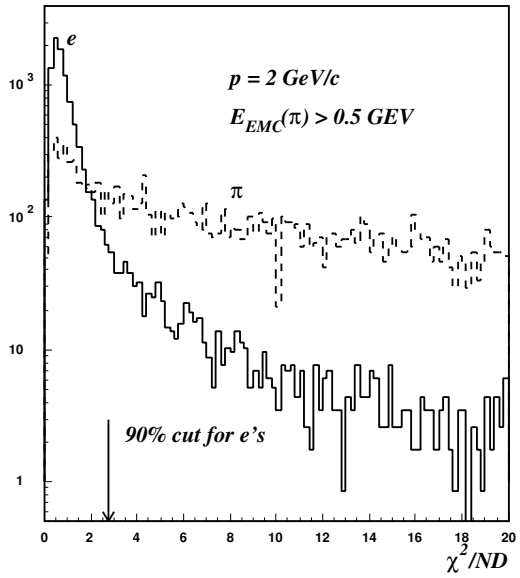

Figure 3.13: χ^2 distribution for showers induced by 2 GeV/c electrons and pions in the PbSc-type calorimeter.

level evaluated with

$$\chi^2 = \sum_i \frac{(E_i^{meas} - E_i^{pred})^2}{\sigma_i^2} \tag{3.17}$$

where i is tower index in a cluster, E_i^{meas} is energy measured in a tower i, E_i^{pred} is energy predicted to be deposited in a tower i, and σ_i is an error on E_i^{pred}. Figure 3.13 shows χ^2 distribution for showers induced by 2 GeV/c electrons and pions in the PbSc-type calorimeter. For example, a cut of "photon probability > 0.01" eliminates 1% of photon clusters and $\sim$50% of hadron clusters.

3.6 Charged particle tracking

The DC system[71] is located in the region from 2 to 2.4 m from the beam pipe to measure the position and momentum of charged particles with the help of the PC (pad chamber). The DC system consists of one frame in each of the East and West Arms, and each frame has a cylindrical shape and a size of 2.5 m$\times$90° in z-ϕ direction (see Fig. 3.14). Each frame is divided into 20 sectors covering 4.5° in ϕ direction, and each sector consists of four sense planes with a 2$\sim$2.5 cm drift space in the ϕ direction (see Fig. 3.15). Each

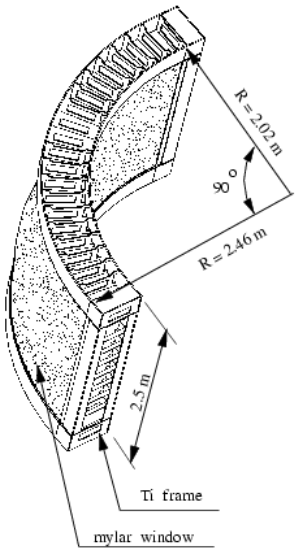

Figure 3.14: The construction of the DC frame.

sense plane has six types of wire modules stacked radially. Two of the six type wires in one sector, which are called X1 and X2, run in parallel to the beam to perform precise track measurements in r-ϕ. The other four type wires, which are called U1, V1, U2 and V2, are tilted by a $\pm 5^\circ$ stereo angle to determine the z coordinate of tracks. In total, 40 wire planes are placed in the following order; 12 X planes (X1), 4 U planes (U1), 4 V planes (V1), 12 X planes (X2), 4 U planes (U2) and 4 V planes (V2) from inner to outer.

The PC system[71] is composed of multi-wire proportional chambers and form three separate layers, which are called PC1, PC2 and PC3, of the Central Arms tracking system. The PC1 is located behind the DC and is used for determining the momentum vector together with the DC by providing the z coordinate. The PC1 consists of a single plane of anode and field wires lying in a gas volume between two cathode planes (see Fig. 3.16). One cathode is segmented into pixels and the other is solid copper, and signals from the pixels are routed outside the gas volume. Figure 3.17 shows the PC pixel pattern. One cell has an effective readout size of 8.45 mm in z $\times$ 8.40 mm in the x-y plane, and is divided into three pixels; one center pixel and two side pixels. Nine pixels over nine (3×3) cells compose a pad that is read out by a single preamplifier and discriminator. Charges made by a particle in the gas volume spread over one or two cells, and the hit reconstruction of the PC system requires that all three pixels in a cell must have a signal si-

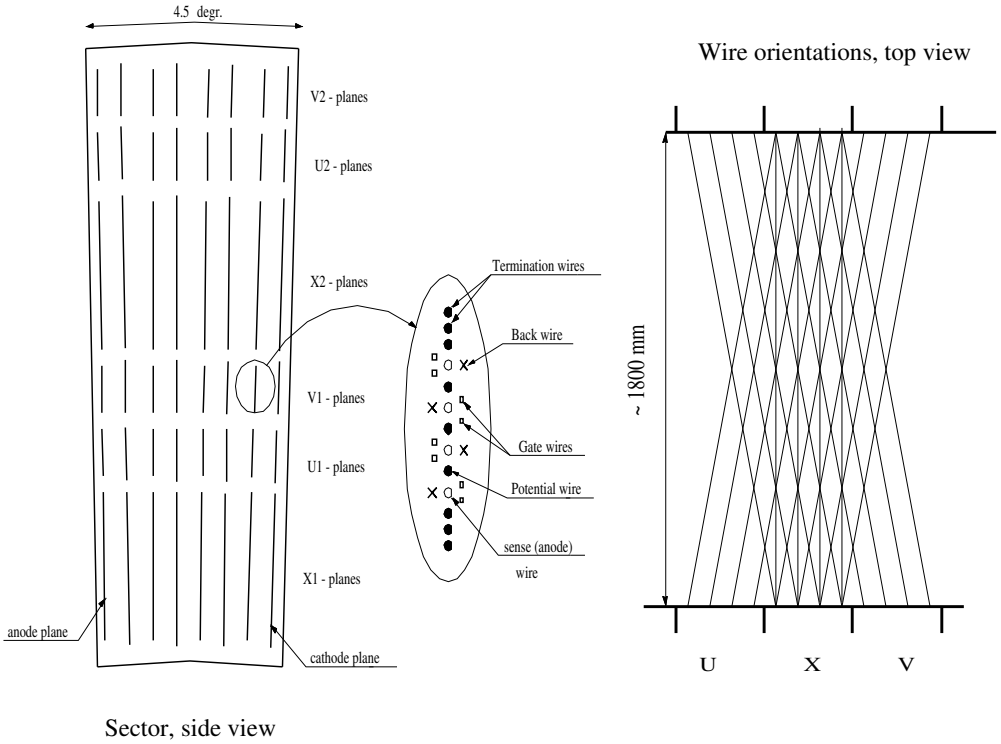

Figure 3.15: The layout of DC wire positions within one sector and inside the anode plane (left). A schematic diagram, top view, of the stereo wire orientation (right).

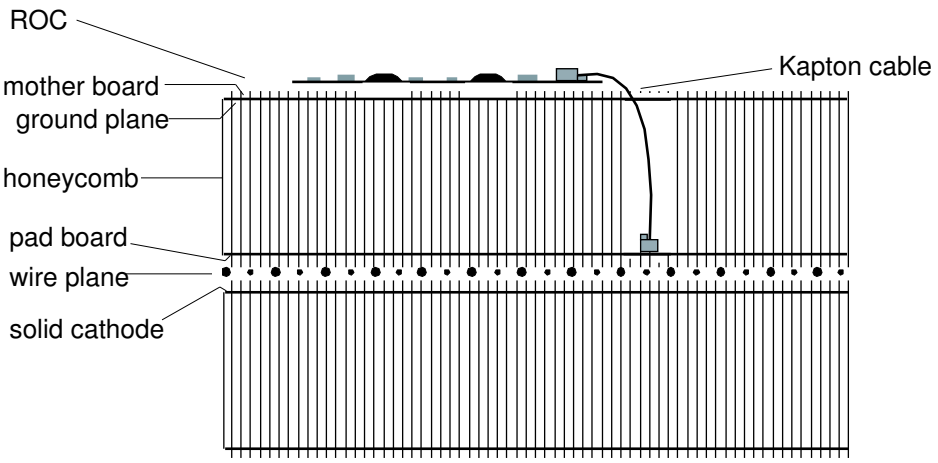

Figure 3.16: The PC vertical cut through a chamber.

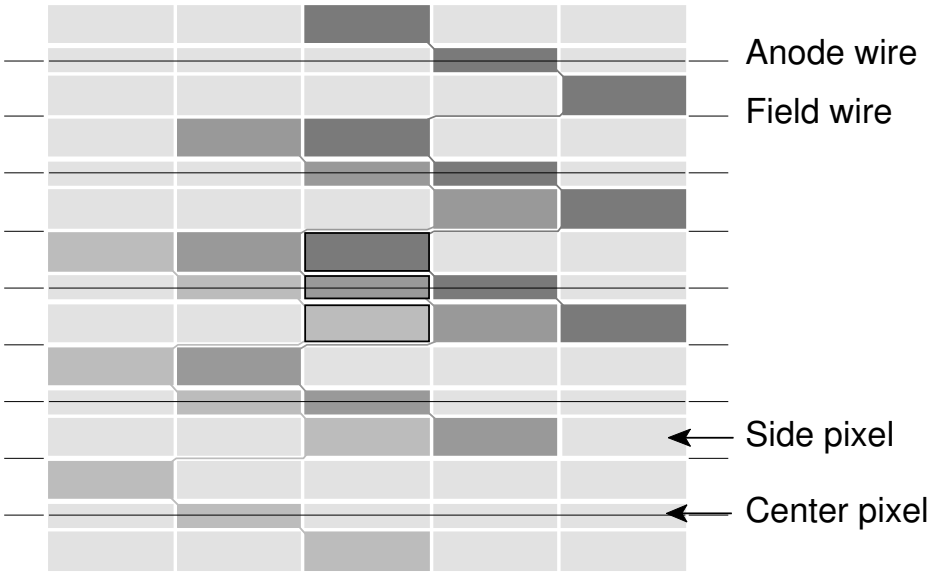

Figure 3.17: The PC pixel pattern. The three pixels form a cell at the center of the figure. Nine connected pixels form a pad.

multaneously. This requirement reduces mis-reconstructions due to electrical noises.

Charged particle tracks are reconstructed using the information of the DC and the PC1[72]. The magnetic field between the collision vertex and the DC is axial, and thus bends particles in the x-y plane. The field is so weak at the DC and the outer side that particle tracks can be assumed to be straight. First, in the DC, a track reconstruction is performed using a combinatorial Hough transform technique. In this technique, the DC hits are mapped pair-wise into a feature space defined by the polar angle at the intersection of the track with a reference radius near the midpoint of the DC (ϕ) and the inclination of the track at that point (α). Figure 3.18 shows variables appeared in the Central Arm tracking, such as ϕ and α. Figure 3.19 shows an example of track hits and a result of the Hough transform using the track hits. The α variable is proportional to the inverse of transverse momentum, and is used as a probable value of reconstructed momentum. Then the tracks reconstructed in the DC are associated with hits in the PC1. If there is an unambiguous PC1 association, θ of a track is defined by z of the associated PC1 hit and z of the collision vertex. If there is no PC1 association or are multiple association candidates, the U and V wires of the DC are used instead of the PC to define θ of a track. The condition of the hit association to a track is represented as a integer parameter "track quality".

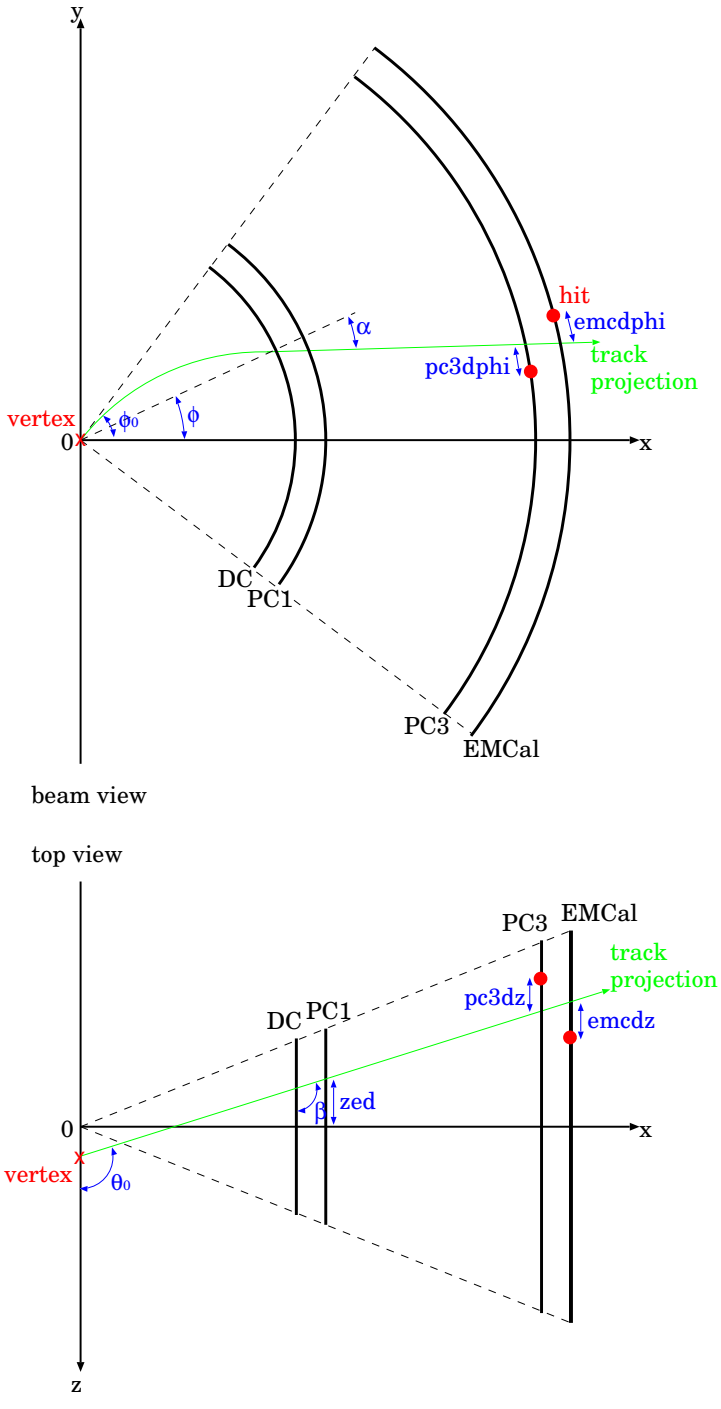

Figure 3.18: Variables in the Central Arm tracking.

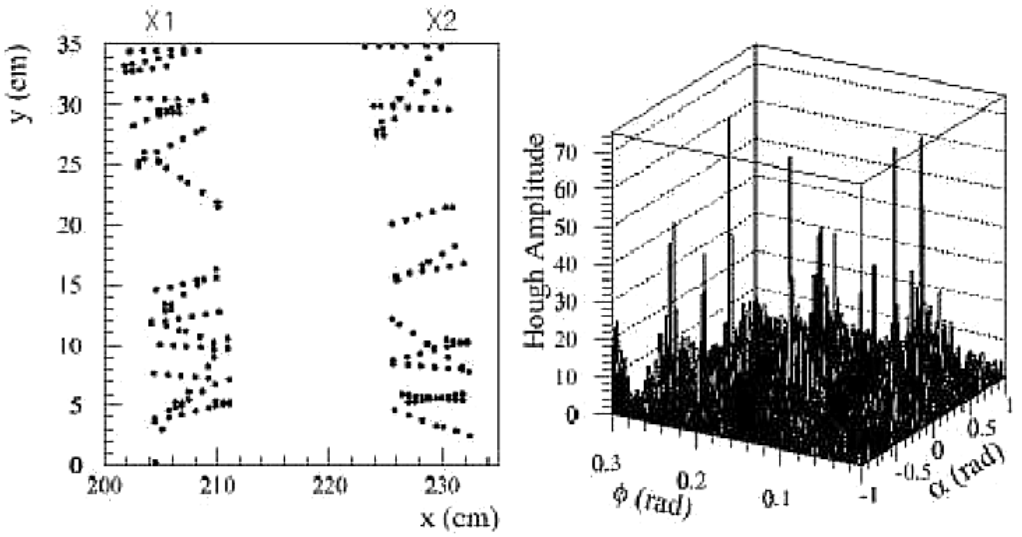

Figure 3.19: **Left**: Simulated hits from a central Au+Au collision for a small physical region of the DC. **Right**: The Hough transform feature space for the region shown in the left plot. Tracks appear as peaks.

It contains 6-bit information; 1st bit = X1 used (or not), 2nd bit = X2 used, 3rd bit = UV found, 4th bit = UV unique, 5th = PC1 found, 6th bit = PC1 unique. Usually the track quality cut "= 31 OR $\geq$ 61" is required, where the "= 31 (= 011111)" means "X1 and X2 used, UV found and unique, PC1 found" and the "$\geq$ 61 ($\geq$ 111101)" means "X1 or X2 used, UV found and unique, PC1 found and unique".

The momentum resolution is given by

$$\frac{\sigma(p)}{p} = 8.1 \cdot p(\mathrm{GeV}/c) + 0.9(\%) \quad \text{at} \quad p \gtrsim 0.5 \text{ GeV}/c \tag{3.18}$$

3.7 Data acquisition (DAQ) system

3.7.1 DAQ outline

The RHIC facility provides the PHENIX with two clocks (blue clock and yellow clock) that synchronize with bunches in either the blue ring or the yellow ring. When the two beams collide the two clocks should make a common timing, and the PHENIX DAQ synchronizes the blue clock practically.

Figure 3.20 shows a block diagram of the PHENIX DAQ system. The blue

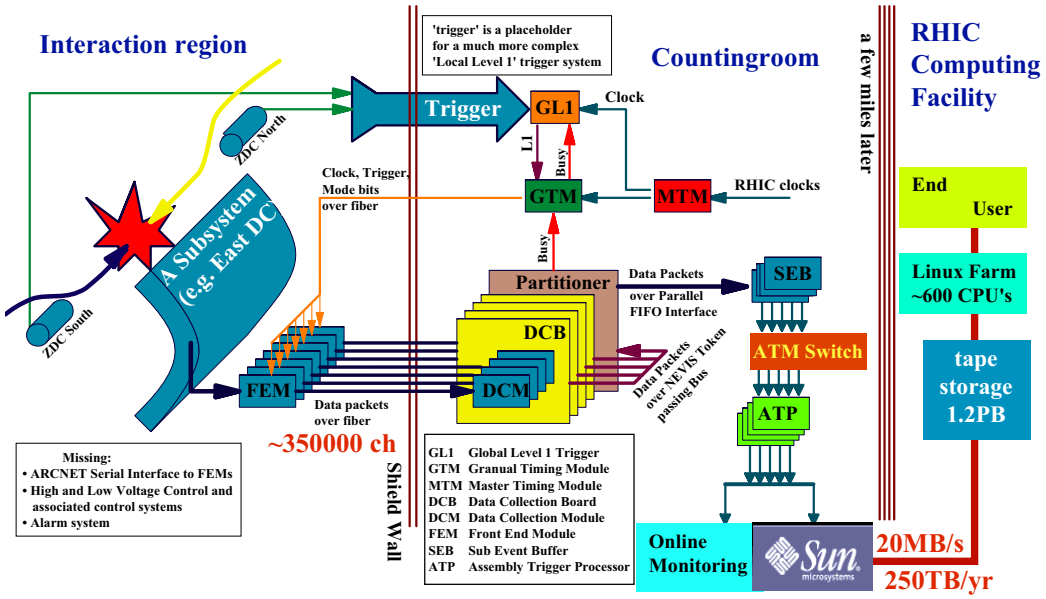

Figure 3.20: Block diagram of PHENIX DAQ system.

clock inputs to the Master Timing Module (MTM) and the MTM distributes the clock timing to the Granule Timing Modules (GTM). Each GTM provides the clock timing to its own granule, where the "granule" means a handy group of detectors such as the BBC, the DC West and EMCal East Bottom (two bottom sectors of the East Arm), and this scheme enables us to operate many granules separately at a time.

The GTM clock inputs to the Front-end Electronics Module (FEM) of its granule that is placed in the interaction region. The FEM holds all data from its detector in the Analog/Digital Memory Unit (AMU/DMU) on the FEM over many RHIC clocks. If an event is decided to be taken by a PHENIX hardware trigger, data of the event stored in the AMU/DMU are read out into the Data Collection Module (DCM) after a digitalization if needed. The DCM formats the data into the PHENIX Raw Data Format (PRDF) and sends them to the Sub Event Buffers (SEB) and then to the Assembly and Trigger Processors (ATP). The SEBs and the ATPs gather all data of each event and write the event data onto five or six hard disks, called PHENIX Buffer Boxes, simultaneously.

As an example of the treatment of detector signals, the EMCal FEM is explained in detail here. Figure 3.21 shows the scheme of the EMCal FEM. One EMCal FEM handles signals from 12×12 towers.

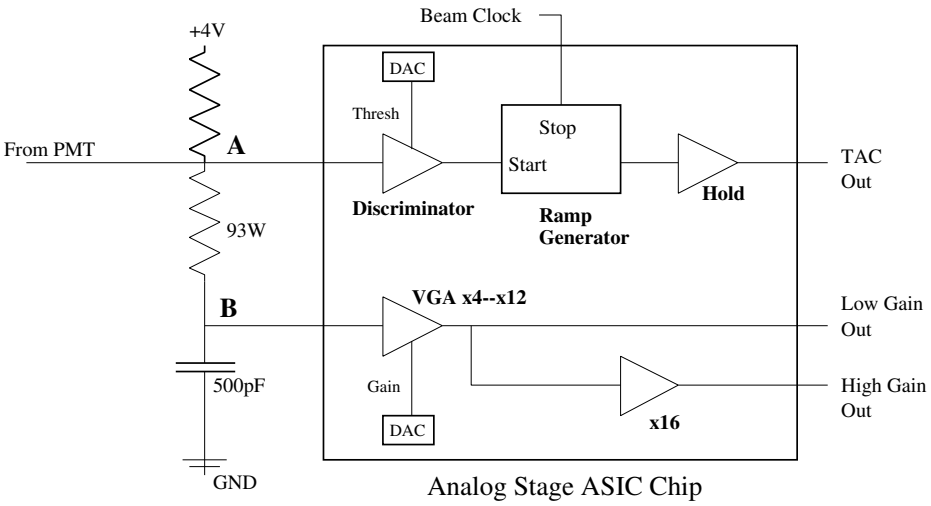

Figure 3.21: The scheme of the EMCal readout circuit.

The PHENIX EMCal PMT emits a negative current pulse with a rise time of < 5 ns. The voltage profile at the point A in Fig. 3.21 follows the current profile and has a fast rise time as the input pulse. The voltage profile at the point B follows the integral of the current, and is a step function with a rise time of ~ 100 ns. The fast and slow voltage pulses are inputted into an ASIC chip, which is designed specially for the PHENIX EMCal system, and are used as a timing and energy signals, respectively.

The timing signal is discriminated in either a leading-edge mode or a constant-fraction mode, where the choices of mode and threshold voltage are remotely selected via ARCNet which is commonly used for the monitoring and the slow control of the PHENIX FEMs. The discriminator starts a voltage ramp generator. The ramp is stopped on the next edge of the RHIC clock providing a common-stop mode TAC. The voltage after a stop is held for two clock cycles and then sampled in an AMU on the EMCal FEM.

On the other hand, the energy signal passes through a Variable Gain Amplifier (VGA), which is exclusive to each PMT and whose gain can be set remotely in a range of $\times 4 \sim \times 12$ with 5-bit resolution. The VGAs compensate for the gain variation of PMTs that share a common high voltage. The dynamic range of physics signals from the EMCal is too large to be covered with a single 12-bit ADC conversion. Thus two different levels of amplification are adopted: one signal is amplified only once by the VGA (called "low-gain"), and another signal is amplified twice by the VGA and a $\times 16$ amplification (called "high-gain"). The low-gain and high-gain signals

are sampled in AMUs on the EMCal FEM.

The TAC, low-gain and high-gain signals are sampled once per RHIC clock tick and each signal is held in a ring buffer of 64 AMUs exclusive to each signal. Therefore the signal is preserved for 64 RHIC clock ticks or ~ 7 ms, which covers the latency of the PHENIX hardware trigger, 40 RHIC clock ticks. When the FEM receives a signal of hardware trigger acceptance on an event, the signals of the event stored in an AMU unit are read out and converted in the ADC. The ADC outputs are controlled, collected and reformatted by several Xilinx FPGAs and are sent to the DCM.

3.7.2 Triggers

The PHENIX experiment has various trigger configurations to efficiently select many interesting rare events. The PHENIX Level-1 trigger is a hardware trigger and consists of two types of subsystems; the Local Level-1 (LL1) triggers and the Global Level-1 (GL1) trigger. Input data from detector systems are processed individually by a LL1 trigger system of each detector to produce a data set of trigger bit for each RHIC beam crossing. The GL1 trigger receives the data from the LL1 triggers and provide a trigger decision. The GL1 trigger can hold 32 sets of trigger configurations and issues a trigger acceptance when at least one of enabled trigger configurations is fired. Any trigger configuration can be prescaled by an arbitrary number, namely one triggered event per *prescale+1* triggered events is recorded. The decision by the GL1 trigger causes all subsystems to send data to the DCM of each subsystem. This measurement uses the BBCLL1 and ERTLL1 trigger systems.

BBCLL1

The BBCLL1 trigger in proton-proton collisions requires one hit on both the north side and the south side. In other words, it requires that one charged particle is produced at both the forward range ($3.0 < \eta < 3.9$) and backward range ($-3.9 < \eta < 3.0$). The reconstructed z-vertex is required to be within $\pm \sim 50$ cm in order to assure an flat acceptance of the PHENIX detectors. The BBCLL1 trigger is used as a minimum bias trigger. In addition, a trigger configuration without the vertex cut, which is called "BBCLL1(noVertexCut)", is used in luminosity measurements.

The efficiency (f_{BBC}) of the BBCLL1 trigger for high-p_T QCD scatterings such as jet production has been evaluated using data triggered by a high-p_T photon trigger, which is called ERTLL1_4x4b and is explained later,

$$f_{BBC} = \frac{N_{\pi 0}^{Ert\&BbcAnyVertex}}{N_{\pi 0}^{Ert}} \tag{3.19}$$

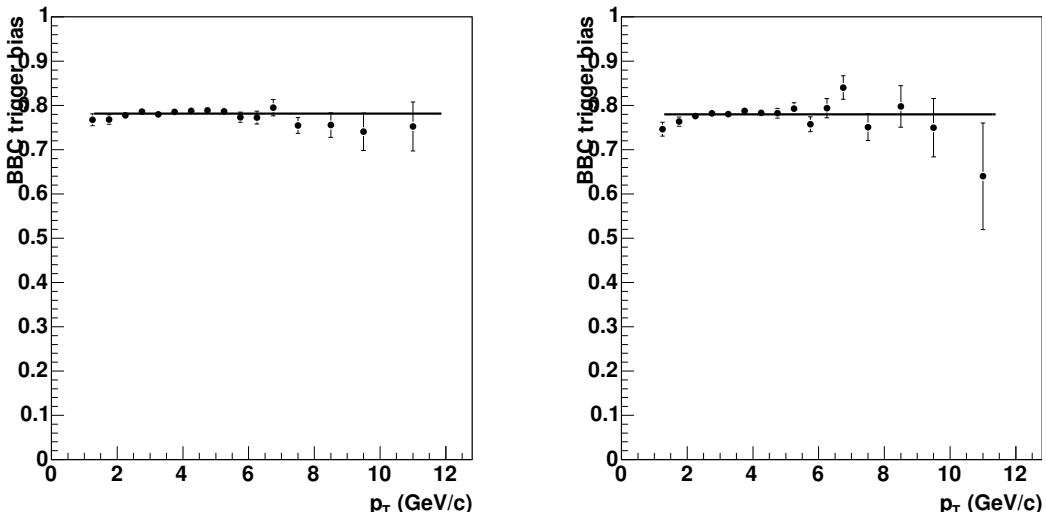

Figure 3.22: The efficiency of the BBCLL1 trigger for π^0 measured with the PbSc (**left**) and PbGl (**right**) sectors as functions of π^0 p_T. Lines are fits to a constant.

where $N_{\pi 0}^{Ert}$ is the number of π^0s in events that fired the ERTLL1_4x4b trigger, and $N_{\pi 0}^{Ert\&BbcAnyVertex}$ is the number of π^0s in events that fired both the ERTLL1_4x4b trigger and the BBCLL1(noVertexCut) trigger. The data analyzed in the f_{BBC} evaluation were taken only by the ERTLL1_4x4b trigger, and a BBCLL1 trigger bit stored in event data was checked in the offline analysis. Figure 3.22 shows the efficiencies f_{BBC} as functions of p_T of π^0 when π^0s were measured with the PbSc or PbGl sectors. The results are independent of π^0 p_T in the measured range. The constant value from the fit are 0.782 ± 0.002 for the PbSc and 0.780 ± 0.003 for the PbGl. The average value 0.781 had to be increased by 0.005 ± 0.005 because of a drop of f_{BBC} from the vertex range $|z| < 30$ cm (the cut is used in physics analysis) to the vertex range $|z| < 40$ cm (where the f_{BBC} was measured). Therefore the final value is

$$f_{BBC} = 0.786 \pm 0.005 \tag{3.20}$$

ERTLL1

The ERT stands for EMCal-RICH Trigger. It is fired by the EMCal and/or the RICH of the Central Arms. It has various configurations concerning the threshold energy or the number of EMCal modules in which the total detected energy is calculated. Figure 3.23 shows the scheme of the EMCal signal summing. Signals from 2×2 EMCal modules (called 2×2 tile) are

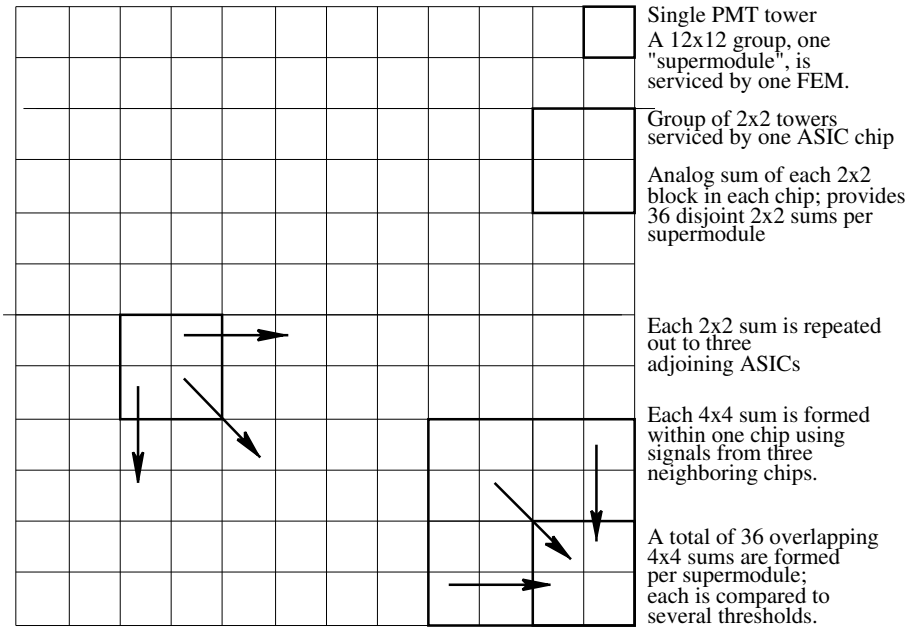

Figure 3.23: The scheme of the EMCal signal summing.

summed up in an ASIC chip on EMCal FEM. Five copies of the summed signal are made and used. One copy is discriminated with an adjustable threshold and used in a trigger called ERTLL1_2x2. One copy is added to three summed signals that come from three adjacent 2×2 tiles, and a 4×4 summed signal is made. The 4×4 summed signal is divided into three sub signals, and three sub signals are discriminated with three different thresholds which are individually adjustable. The three discriminated signals are called ERTLL1_4x4a, ERTLL1_4x4b and ERTLL1_4x4c. Three copies are sent to three adjacent 2×2 tiles to form 4×4 summed signals on them. 4×4 tiles overlap with one another, namely the right-top 2×2 tile in a 4×4 tile is the left-top 2×2 tile in the right-next 4×4 tile, and thus the trigger efficiency doesn't change even if a photon hits on an edge of a 4×4 tile. Table 3.2 summarizes ERT trigger configurations. The ERTLL1_4x4c trigger was used in the analyses for this thesis.

The efficiency (f_{ERT}) of the ERTLL1_4x4c trigger has been evaluated using data triggered by the BBCLL1 trigger:

$$f_{ERT}(E) = \frac{N_{ph}^{MB\&ERT}(E)}{N_{ph}^{MB}(E)} \tag{3.21}$$

where $N_{ph}^{MB}(E)$ is the number of photons with an energy E in events that

Table 3.2: The main ERT configurations concerning the photon detection.

name	EMCal energy threshold	EMCal modules
ERTLL1_2x2	0.4 or 0.6 GeV	2×2
ERTLL1_4x4a	2.1 GeV	4×4
ERTLL1_4x4b	2.8 GeV	4×4
ERTLL1_4x4c	1.4 GeV	4×4

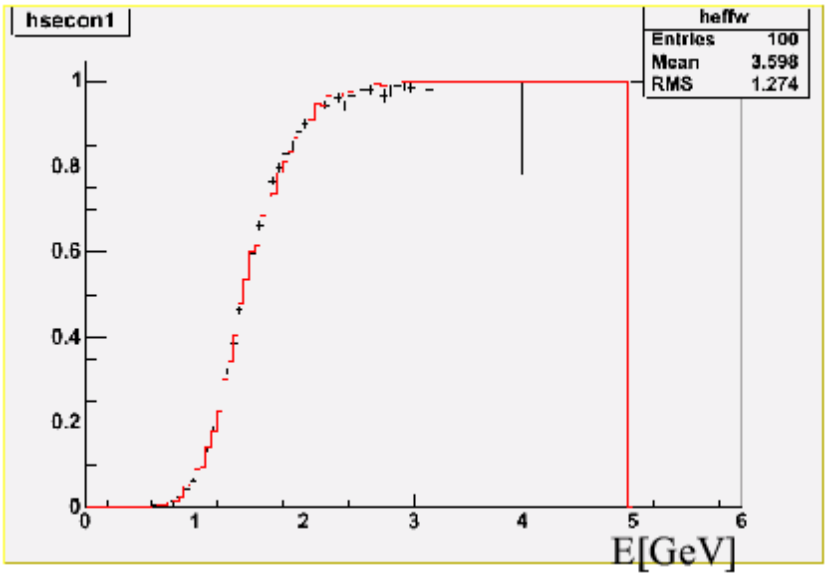

Figure 3.24: The ERTLL1_4x4c trigger efficiency as a function of photon energy.

fired the BBCLL1 trigger, and $N_{ph}^{MB\&ERT}(E)$ is the number in events that fired both the BBCLL1 trigger and the ERTLL1_4x4c trigger. The data analyzed in the f_{ERT} evaluation were taken only by the BBCLL1 trigger, and a ERTLL1_4x4c trigger bit of 12×12 modules that a photon hit was checked in the offline analysis. Figure 3.24 shows the efficiency f_{ERT}. The turn-on curve at $E \sim 1.4$ GeV is caused by variations of tower gains and of trigger thresholds. The efficiency is almost flat and close to unity above $E \sim 2$ GeV.

Trigger count scaler

The PHENIX DAQ have two types of scalers, GL1 scaler and GL1P scaler. The GL1 scaler counts the events triggered by each trigger configuration. Three types of counts are accumulated; raw, live (event count when the DAQ isn't in dead time) and scaled (event count after the prescale). The GL1P scaler counts the events which occured at each beam crossing and triggered by one of four trigger configurations. The GL1P scaler counts are used in evaluating luminosities of every beam crossing in proton-proton collisions.

3.8 Simulation settings

To understand the response of the detectors in jet measurement, the PYTHIA event generator[73] and the GEANT detector simulator[74] were used.

3.8.1 PYTHIA event generator

The PYTHIA version 6.220 was used. The collision condition is the same as the actual experiment: proton-proton collisions in their center-of-mass frame at $\sqrt{s} = 200$ GeV. With the MSEL set to 1, the PYTHIA generates QCD high-p_T process. With the CKIN(3) set to 1.5, the PYTHIA generates the events which have a $\hat{p}_T$ of > 1.5 GeV/c, where $\hat{p}_T$ is transverse momenta of scattered partons in center-of-mass frame of the two scattered partons. The modified MSEL and CKIN(3) reduces the time for event generation and does not affect any physics results at measured p_T region. We call a PYTHIA simulation with these conditions "PYTHIA default".

3.8.2 Underlying event and Multi-Parton Interaction

When a hard parton-parton scattering event takes place in proton-proton collisions, the event contains particles which originate from the two outgoing partons and also particles which come from the breakup of the proton, i.e. beam-beam remnants. The former particles consist of the two outgoing jets and initial- and final-state radiation. The latter particles are everything except the former ones, and are called "underlying event". The two kinds of particles cannot be completely distinguished with topological selection of events. Therefore, reconstructed jets are contaminated with the underlying event.

The PYTHIA reproduces the underlying event with Multi-Parton Interaction (MPI) mechanism. The MPI includes many semi-hard or soft parton-parton scatterings in one event. Figure 3.25 is a schematic drawing of MPI.

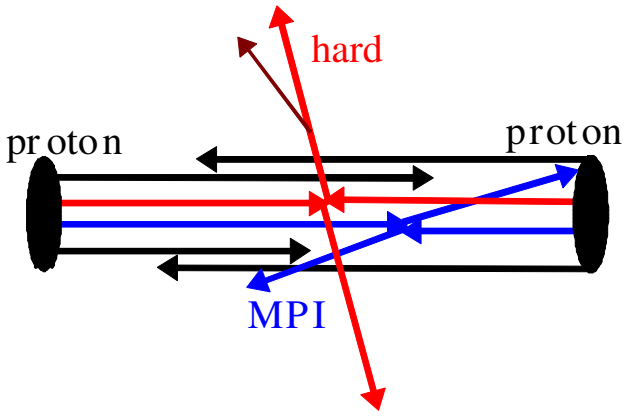

Figure 3.25: Schematic drawing of multi-parton interaction.

First the hardest parton-parton scattering is generated with its initial- and final-state radiation, next any multiple interactions, and finally beam remnants are attached to the initiator partons of the hardest scattering to form Lund strings.

By default the PYTHIA employs the MPI for reproducing the underlying event, but it does not reproduce the data with satisfactory precision. Therefore we modified MPI parameters as shown in Tab. 3.3. The values in Tab. 3.3 have been tuned with CDF data[75]. We call the PYTHIA with these conditions "PYTHIA MPI".

Actually the values in Tab. 3.3 have been adopted as default values in the PYTHIA version 6.226 and later. We checked outputs of the "PYTHIA default" and the "PYTHIA MPI" to estimate the effect of the underlying event on our measurement.

3.8.3 GEANT detector simulator

The PHENIX experiment has developed a GEANT3-based detector simulator, called Phenix Integrated Simulation Application (PISA). It holds the position and material of all detectors as drawn in Fig 3.26 and generates hit signals made by simulated particles. The hit signals are formatted into the PRDF and then are processed in the same way as the real data. But the PISA doesn't have actual detector conditions such as a variation of the EMCal tower gains and a bad (dead/noisy) area of the tracking system. Therefore outputs of the simulation were compared with the real data and the simulation has been tuned as described in the next chapter.

Table 3.3: PYTHIA MPI parameters.

parameter	default	used
MSTP(81)	1	1
MSTP(82)	1	4
PARP(81)	1.9	1.9
PARP(82)	1.9	2.0
PARP(83)	0.5	0.5
PARP(84)	0.2	0.4
PARP(85)	0.33	0.9
PARP(86)	0.66	0.95
PARP(89)	1000	1800
PARP(90)	0.16	0.25
PARP(67)	1.0	4.0

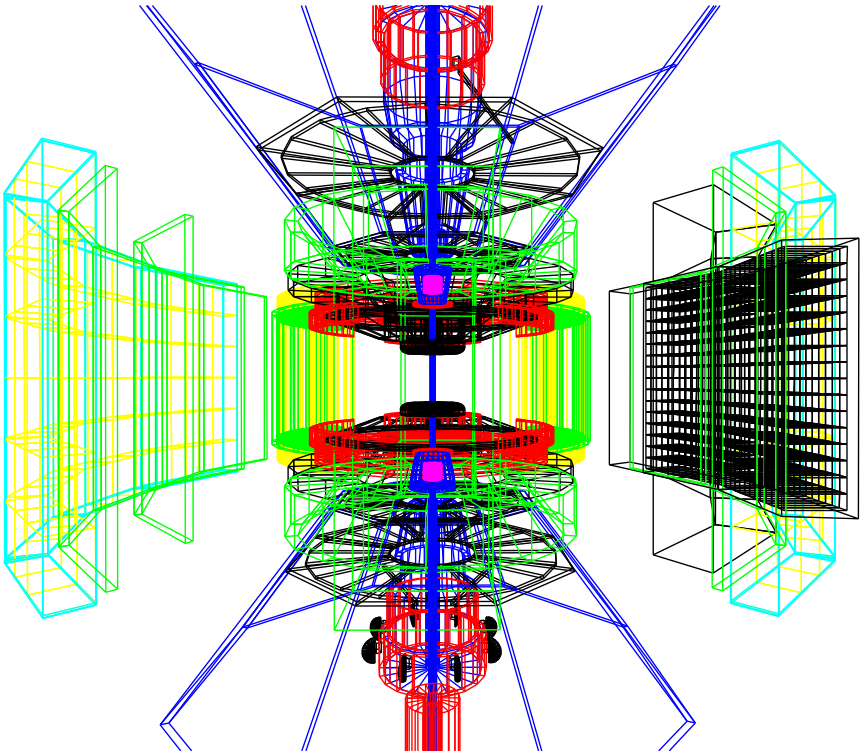

Figure 3.26: The detector geometry in the simulation. It is seen from top. The East Arm is on the right side.

Chapter 4

Analysis Methods

4.1 Outline

In this thesis, A_{LL} of jet production process is analyzed to extract Δg. The data taken in 2005 are used. The total luminosity delivered to PHENIX is 3.8 pb^{-1}, and the PHENIX DAQ recorded 2.7 pb^{-1}, mostly with the ERTLL1_4x4c & BBCLL1 trigger. The BBCLL1 (without ERTLL1_4x4c) trigger was also used for a check on systematic errors in the analyses for this thesis. The effective luminosity recorded with the trigger was $\sim$0.3 pb^{-1} because the BBCLL1 trigger was prescaled by $\sim$10 on average in order to match the total bandwidth of the PHENIX DAQ $\sim$ 5 kHz. Some data were discarded because of bad conditions as described in Section 4.2.

Core particles of jet were measured and clustered with the cone method. Photons in jets were detected with the EMCal, and charged particles in jets were detected with the DC and PC1. Quality assurances and calibrations of the detectors were made as described in Section 4.3. The methods of particle clustering is described in Section 4.4.

The relation between measured jet core and original jet was estimated with the PYTHIA+GEANT simulation. Simulation studies are explained in Section 4.5. To confirm that the simulation reproduces well the real data in terms of event structure, namely spacial distribution of particles in an event, quantities sensitive to event structure were measured and was compared between the real data and the simulation output. It is described in Section 4.6.

Rate of cone production was measured in prior to A_{LL}. It assures that pQCD is applicable to our measurement. The methods of the rate measurement are described in Section 4.7. The methods of A_{LL} measurement and various checks on systematic errors are described in Section 4.8.

4.2 Run selection

The PHENIX DAQ usually takes data continuously for 0.5 to 1 hour, and such continuous data taking period is called "run". All quality assurances were done run-by-run. After the run selections which are described below, the integrated luminosity of usable data was 2.2 pb^{-1}.

Obvious problems were detected during the data taking. High voltage trips of the DC, PC and EMCal were monitored, which cause an increase of dead areas. Variations of gain of the EMCal modules were traced using a test pulse by laser or LED. Detector QA analyses detected further problems: Noisy EMCal modules were detected as a large π^0 combinatorial background. Noisy wires of the DC and/or PC1 were detected as a high occupancy. The status of beam polarization was checked (wrong spin pattern, bad local polarimeter condition, etc.). Runs with bad scaler counts were discarded because scaler counts are used in luminosity evaluation.

4.3 Quality assurance and calibration of detectors

4.3.1 EMCal

Bad-tower map

Noisy or dead towers were detected by checking the number of hits per tower compared to its mean value in a sector. All runs were divided into nine ranges of run numbers, and energies were divided into four ranges; 0.4∼0.5, 0.5∼2, 2∼5 and 5∼30 GeV. The check has been done in each run and energy range. The towers that were bad in at least one range were labeled bad. All the edge towers and the uncalibrated towers in the tower-by-tower energy calibration which is described later were also labeled bad. Towers around the noisy/dead/edge/uncalibrated towers (3x3 towers) were excluded in this analysis. Figure 4.1 shows the bad-tower map.

EMCal and ERT live area

Table 4.1 shows the history of ERTLL1_4x4c masks due to noisy trigger tiles. The first half of statistics has been taken with four masks (W0-FEM5, E0-FEM26, E2-FEM1, E0-FEM12) and the latter half has been taken with additional four masks (W3-FEM4, W2-FEM9, E0-FEM6, E0-FEM16). The additional four masks cover only 2% of the acceptance. Therefore we decided

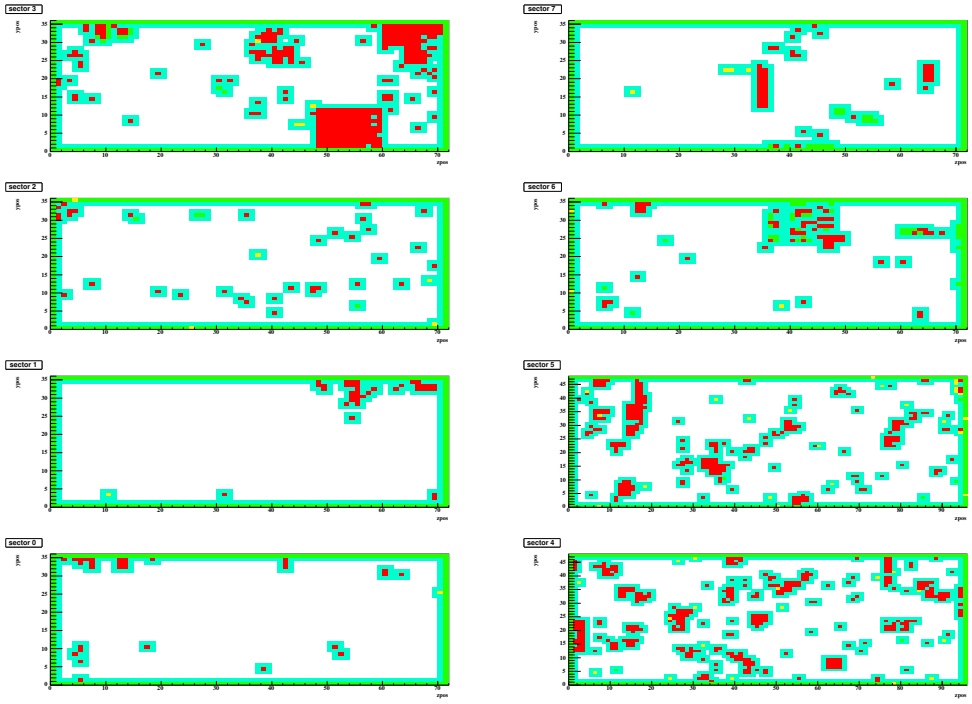

Figure 4.1: EMCal bad-tower map. (red: noisy, yellow: dead, green: uncalibrated/edge, glaucous: around them).

Table 4.1: The history of the ERT 4x4c FEM mask.

date	run from	masks added	statistics
2005.04.09	-	W0-FEM5, E0-FEM26, E2-FEM1	0%
2005.04.17	168320	E0-FEM12	55%
2005.06.03	176574	W3-FEM4	0%
	176608	W2-FEM9	1%
2005.06.04	176803	E0-FEM6, E0-FEM16	44%

Table 4.2: The live areas of the EMCal towers and ERTLL1_4x4c trigger tiles. All two towers from sector edges have been excluded in advance.

Sector	EMCal live	ERT live	Both live	N of towers
W0	2052 (94.30%)	2076 (95.40%)	1952 (89.71%)	2176
W1	2061 (94.72%)	2176 (100.00%)	2061 (94.72%)	2176
W2	1898 (87.22%)	2032 (93.38%)	1769 (81.30%)	2176
W3	1506 (69.21%)	2056 (94.49%)	1506 (69.21%)	2176
E0	2812 (69.47%)	3544 (87.55%)	2363 (58.37%)	4048
E1	3050 (75.35%)	4048 (100.00%)	3050 (75.35%)	4048
E2	1827 (83.96%)	2056 (94.49%)	1710 (78.58%)	2176
E3	1930 (88.69%)	2176 (100.00%)	1930 (88.69%)	2176
Total	82.86%	95.66%	79.49%	

that the live area with the eight masks was used in acceptance correction with the absolute 2% systematic error.

Table 4.2 shows the live areas of the EMCal towers and the ERTLL1_4x4c trigger tiles. All the edge towers (two towers from edge) were excluded in this calculation.

Energy calibration

The gains of the EMCal towers have been measured before the installation and are used to evaluate energy deposited in each tower. But the gains gradually shift and thus a fine recalibration using physics data is needed. The energy calibration for the data taken in 2005 has been done with the following procedure;

1. correction for tower-by-tower gain variation,
2. correction for run-to-run gain shift, and
3. correction for residual non-linearity at low energy.

The correction for the tower-by-tower gain variation used a part of data taken in 2005. The correction is represented with one parameter ϵ_i for each tower (index i), with which a calibrated tower energy is given by $E_i^{calib} = \epsilon_i E_i^{orginal}$. The ϵ_i of a tower i was adjusted so that a π^0 mass peak position was at 135 MeV (Particle Data Group value[14]).

The π^0s were reconstructed with photon pairs in which one photon hits the tower i with an energy of > 0.8 GeV and another photon hits other

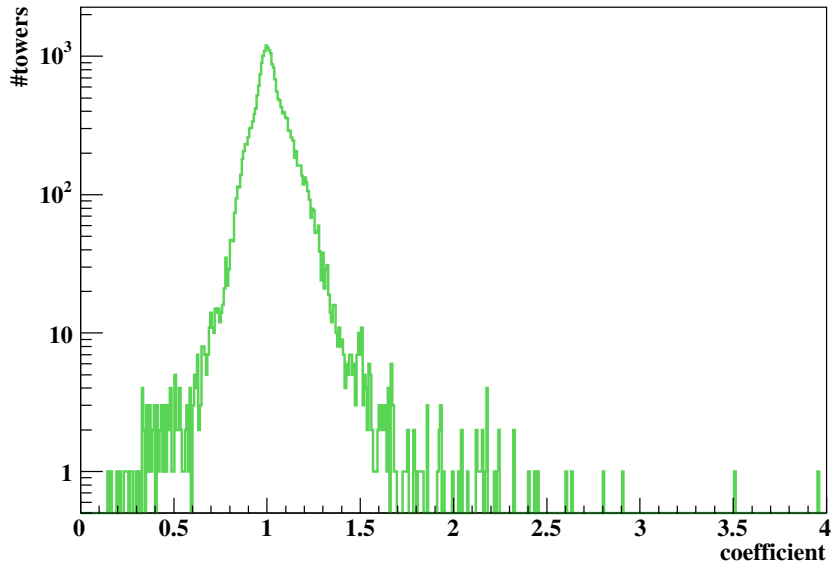

Figure 4.2: The distribution of the correction factor ϵ_i on tower energy.

tower with an energy of > 0.1 GeV. All photons had to have the photon probability of > 0.01, and only π^0s with $p_T > 1.0$ GeV/c were used. The π^0 mass peak position was obtained by fitting it to a "Gaussian + 2nd/3rd order polynomial" function, and the ϵ_i was set to the ratio of the PDG value to the obtained peak position. Here it was assumed that the peak position only depended on the energy of the tower i, but in reality it did depend on the energies of towers around the tower i and the energy of the pair photon. The parameters ϵ of other towers were obtained with the same procedure.

Since the ϵ_i wasn't accurate due to the assumption above, the procedure was iterated on all towers seven times. In the iterations, a photon energy was calibrated with ϵ's obtained in a previous iteration as $E_{new} = \sum_j \epsilon_j e_j$, where the j was indices of towers that composed the photon cluster, and e_j is the energy deposited in tower j. Figure 4.2 show the distribution of the correction factor ϵ_i. Figure 4.3 shows the position and width of π^0 mass peak before and after the correction. The width was decreased by $\sim 10\%$, which is consistent with the width of the ϵ_i distribution.

The correction for the run-to-run gain shift was done because the π^0 mass peak position was gradually decreasing by 3% during the whole data taking period. All runs were divided into 10 run periods. One parameter for each run period and each sector was evaluated so that the π^0 mass peak positions

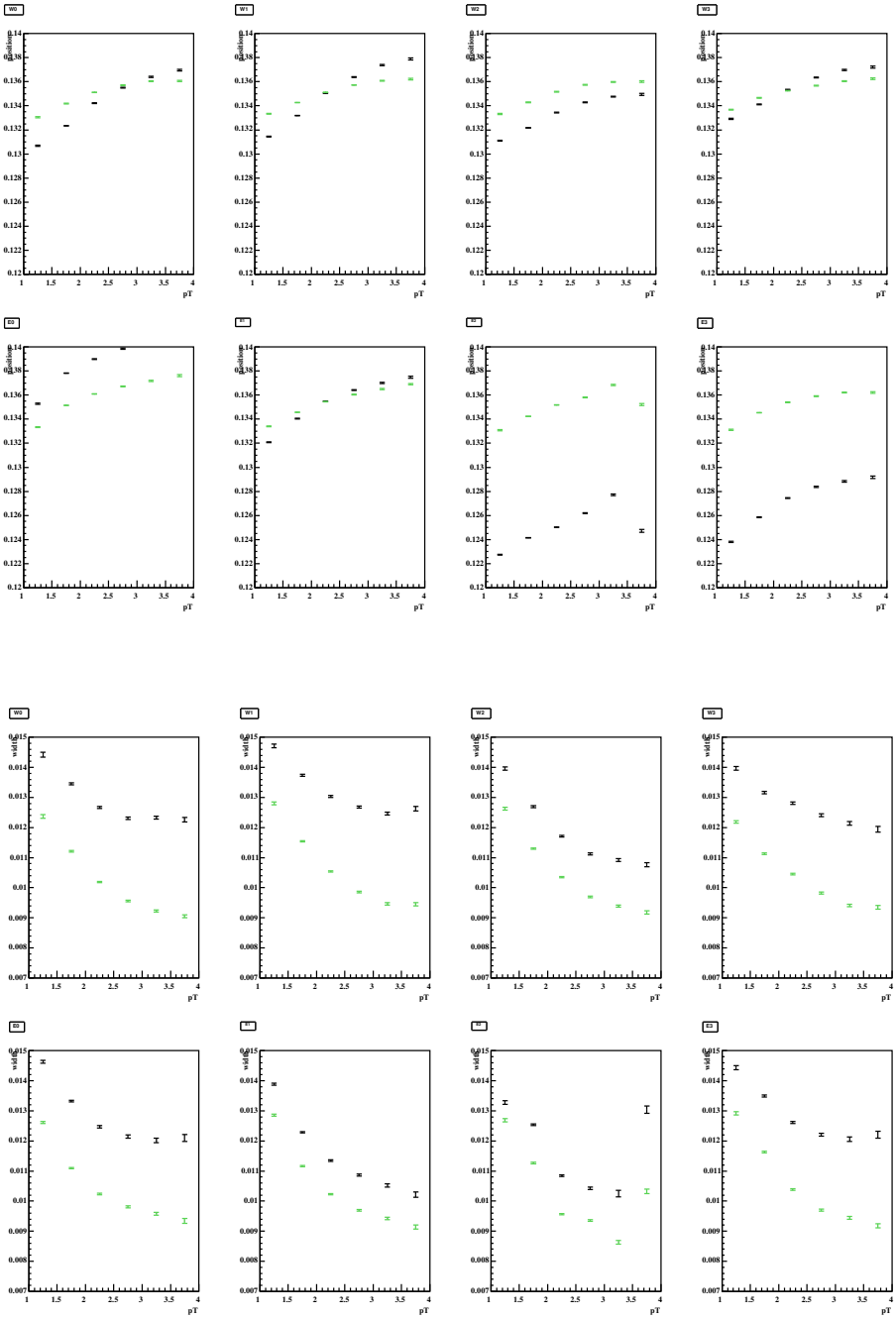

Figure 4.3: The position (**Top**) and width (**Bottom**) of π^0 mass peak as functions of p_T of π^0 in each sector before (**Black**) and after (**Green**) the correction for the tower-by-tower gain variation.

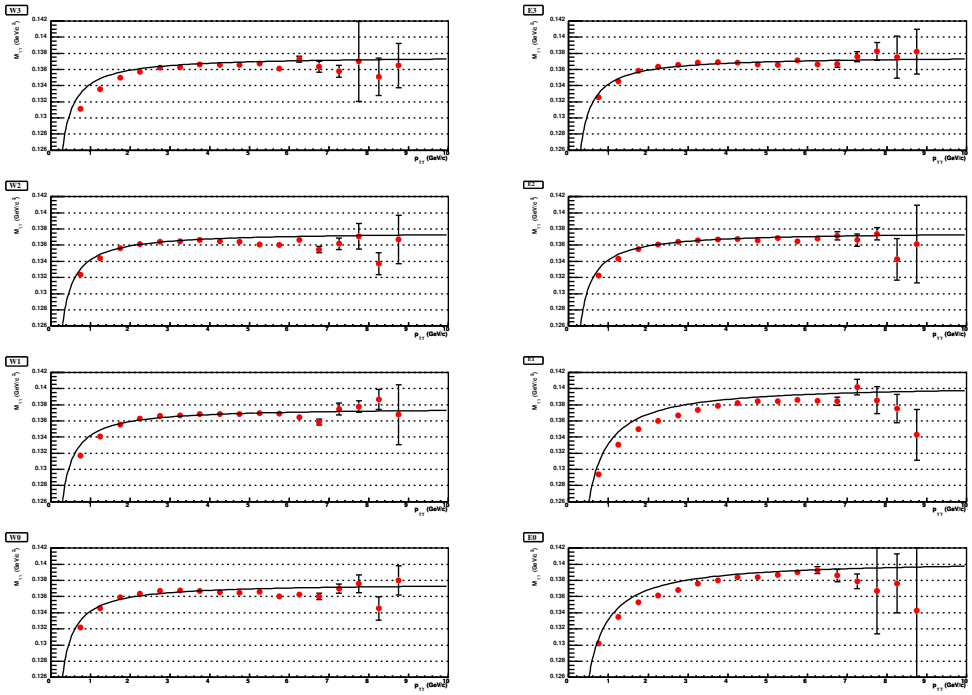

Figure 4.4: The position of π^0 mass peak as a function of photon-pair momentum at each EMCal sector, where only photon pairs with a symmetric energy were used. Lines are the correction factor $\epsilon(\bar{E}) = a - b/\bar{E}$ where $\bar{E} = p_{\gamma\gamma}/2$.

reconstructed in every run period and sectors became equal to one another. The parameters varied from 0.98 to 1.01.

The correction for the residual non-linearity at low energy also used the π^0 mass peak position. Although the non-linearity correction have been applied in the EMCal photon reconstruction together with the incident-angle correction, residual non-linearity has been checked and corrected. Two photons with a symmetric energy (energy asymmetry $a \equiv \frac{|E_1 - E_2|}{E_1 + E_2} < 0.2$) were used to reconstruct π^0s. Under this condition the effect of the non-linearity on two photons was the same. The effect was parameterized with the average of two photon energies $\bar{E} = |p_{\gamma\gamma}|/2$. Figure 4.4 shows the π^0 mass peak position as a function of photon-pair momentum. The PbSc sectors and the PbGl sectors have some strong dependencies. The correction factor $\epsilon(\bar{E})$ was determined so that the mass peak position at each $p_{\gamma\gamma}$ bin moves to the expected value (136 MeV). The expected value of the π^0 mass is not 135 MeV because of the energy smearing effect. It has been estimated to be

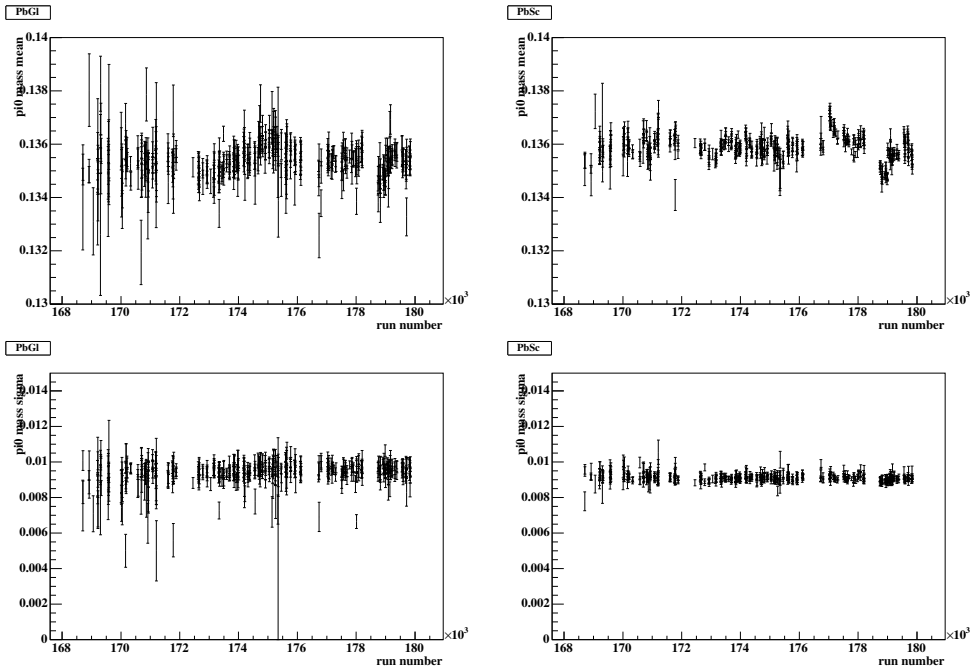

Figure 4.5: **Top**: The mean value of π^0 mass peak for PbGl (left) and PbSc (right) vs run number. **Bottom**: The sigma of π^0 mass peak for PbGl (left) and PbSc (right) vs run number. The non-linearity correction and run-to-run scale correction have already been applied.

136 MeV with a simulation. The correction factor $\epsilon(\bar{E})$ are represented as a function

$$E_{corrected} = E_{org}/(a - b/E_{org}) \tag{4.1}$$

$$a = 1.012\ , \quad b = 0.0127 \quad (PbSc) \tag{4.2}$$

$$a = 1.033\ , \quad b = 0.0269 \quad (PbGl) \tag{4.3}$$

Figure 4.5 shows the mean and sigma of π^0 mass as a function of run after applying all the corrections.

Energy scale and resolution

After all the corrections above have been applied to the data, the energy scale and resolution of photons were confirmed by checking the position and width of π^0 mass peaks. Photon selections used in the cone measurement described later were applied. Figure 4.7 and 4.6 show π^0 mass distributions measured with the PbGl and the PbSc, respectively, at π^0 p_T bins. Figure 4.8 shows

the position and width of the peaks as functions of π^0 p_T. The red lines are results of the real data. The peak position is around the expected value of 136 MeV over all p_T range, but small deviations still remain. Therefore a 1.5% systematic error was assigned to the photon energy scale.

The black lines in Fig. 4.7, 4.6 and 4.8 are results of the simulation. This comparison has been done to assure that the simulation condition matches the real one. A data set of input π^0s was generated with flat distributions in p_T, η and ϕ spaces and weighted by the measured p_T slope[76];

$$w(p_T) = \frac{Ap_T}{(1 + p_T/p_0)^n} \tag{4.4}$$

$$A = 386 \text{ mb GeV}^{-2}c^3 \ , \quad p_0 = 1.219 \text{ GeV}/c \ , \quad n = 9.99 \tag{4.5}$$

In the simulation the bad-tower map was applied to match the masked area as was in the real data analysis. An additional smearing by ∼6% on simulated energy was applied. Finally the simulation output agrees with the real data.

4.3.2 Tracking detectors

Fiducial cut

Low-efficiency or dead areas in the DC and PC1 were detected by checking hit counts. Hit position of tracks were parameterized by a board number and the alpha value (shown in Fig. 3.18). The board number is an index of the sense-wire planes of the DC, where 80 planes cover the 90° azimuth. A straight track crosses a single plane while a track that have a large alpha crosses multiple planes. Thus low-efficiency or dead areas can depend on the alpha as well as the board number. Tracks that had the track quality of "= 31 OR ≥ 61" were used. Hit counts in 100 runs at the beginning of the data taking, 50 runs at the end and the simulation output were checked. Some (alpha, board) positions have been masked in the measurements and the simulation so that the fiducial areas became the same. Figure 4.9 and 4.10 show the hit counts in the real data before and after the fiducial cut.

Momentum scale and resolution

The momentum scale and resolution of the central tracking system were checked both for the real data and the simulation output to confirm the reproducibility of the simulation. The momentum scale and resolution were evaluated from m^2s for $\pi^{\pm}$, $K^{\pm}$ and $p^{\pm}$ using the DC, the PC1 and a high-resolution TOF which is located at the front of the PbGl-type EMCal. The

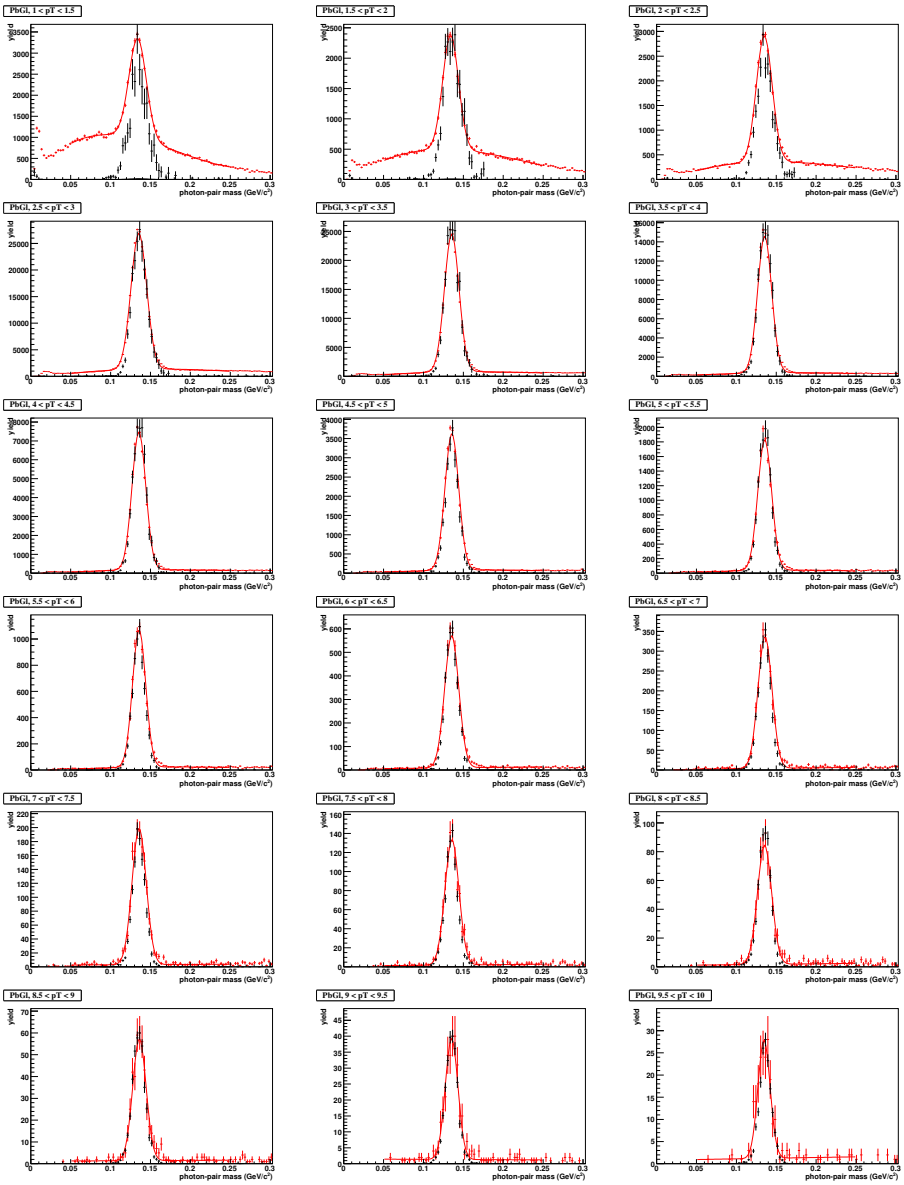

Figure 4.6: π^0 mass distribution for PbGl with single particle simulation after applying the scale and resolution correction (red: real data, black: simulation output).

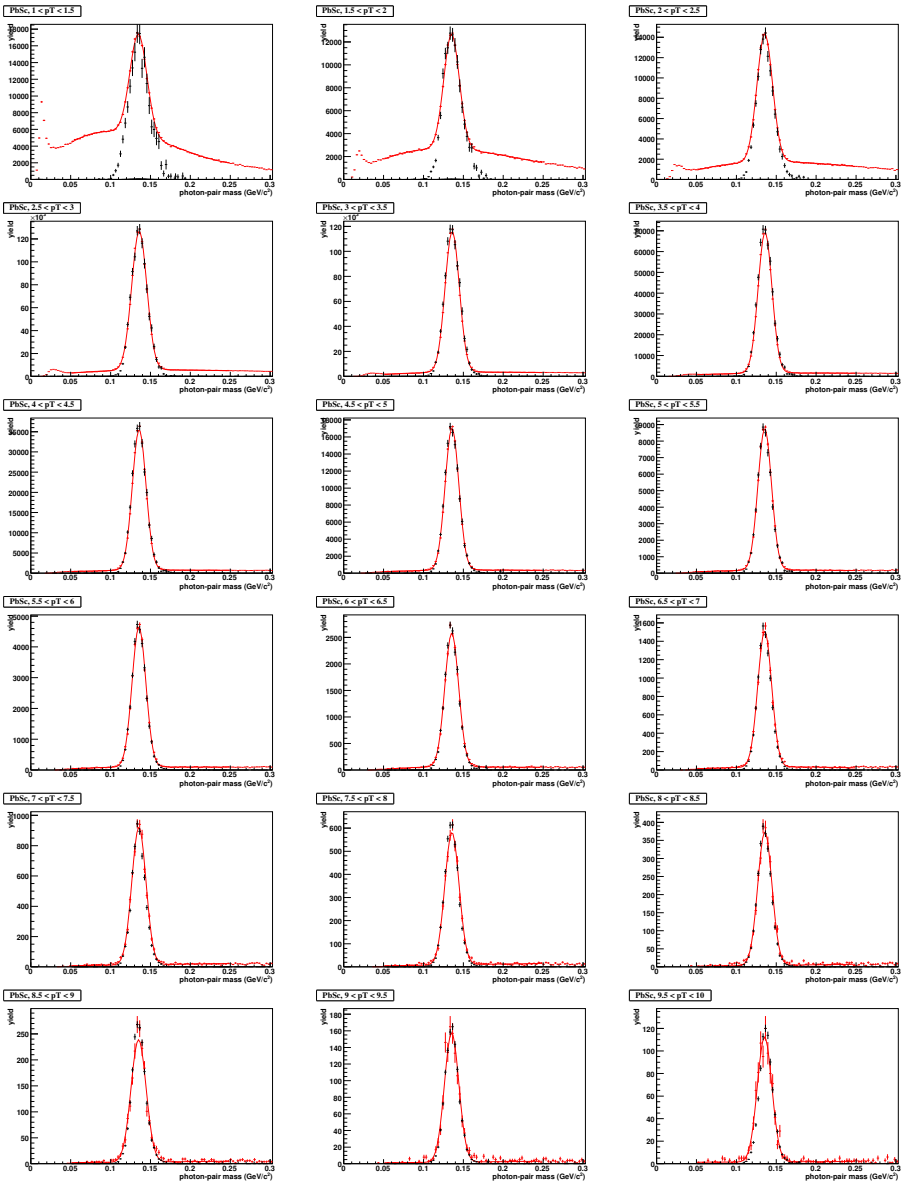

Figure 4.7: π^0 mass distribution for PbSc with single particle simulation after applying the scale and resolution correction (red: real data, black: simulation data).

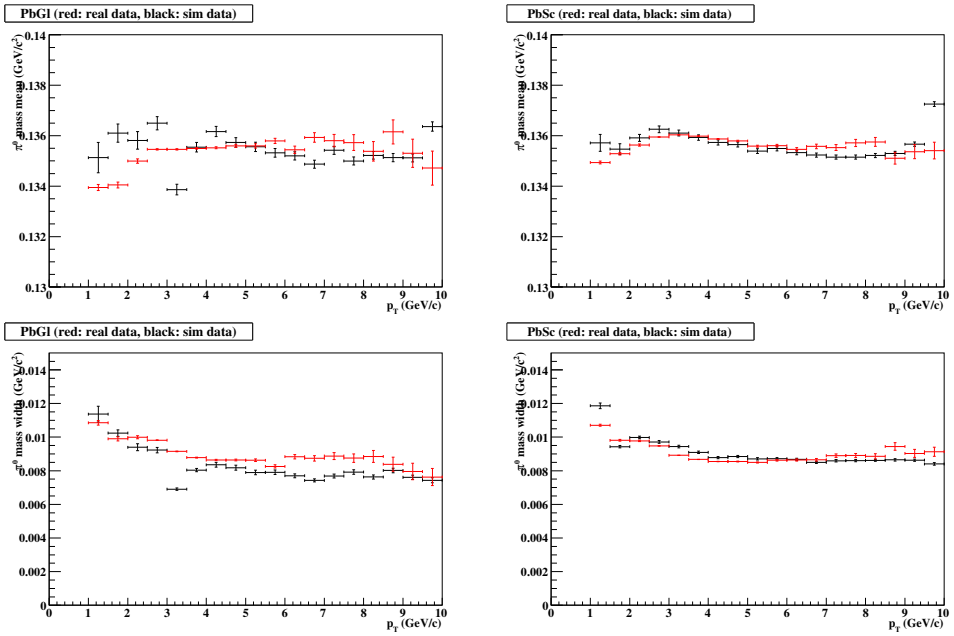

Figure 4.8: The mean value and sigma of π^0 mass distribution for PbSc with single particle simulation after applying the scale and resolution correction (red: real data, black: simulation data).

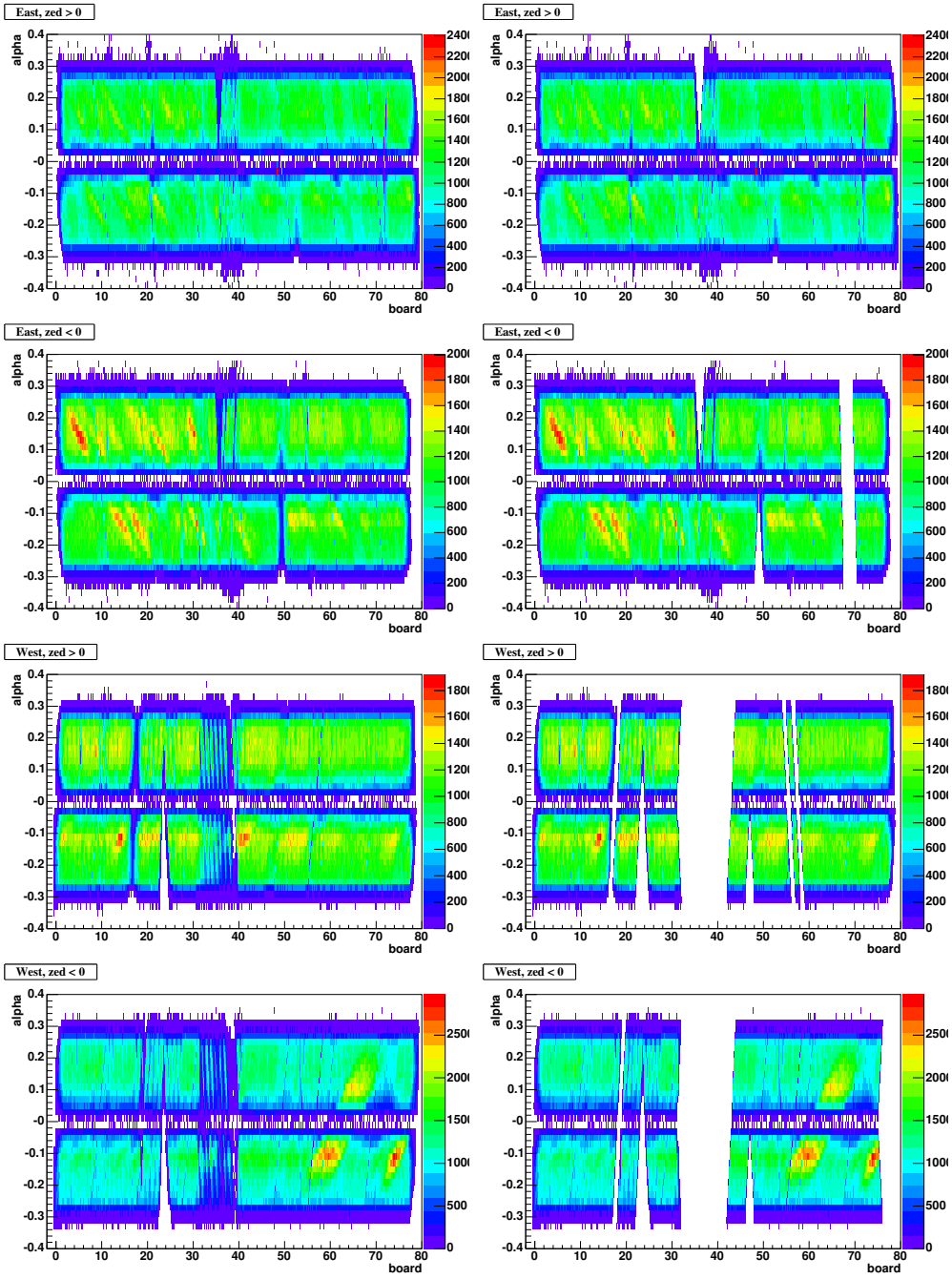

Figure 4.9: **Left**: The hit counts in (alpha, board) bins for East/West Arms and $zed > 0/zed < 0$ positions in 100 runs at the beginning before fiducial cut. **Right**: Same as the left plots after fiducial cut.

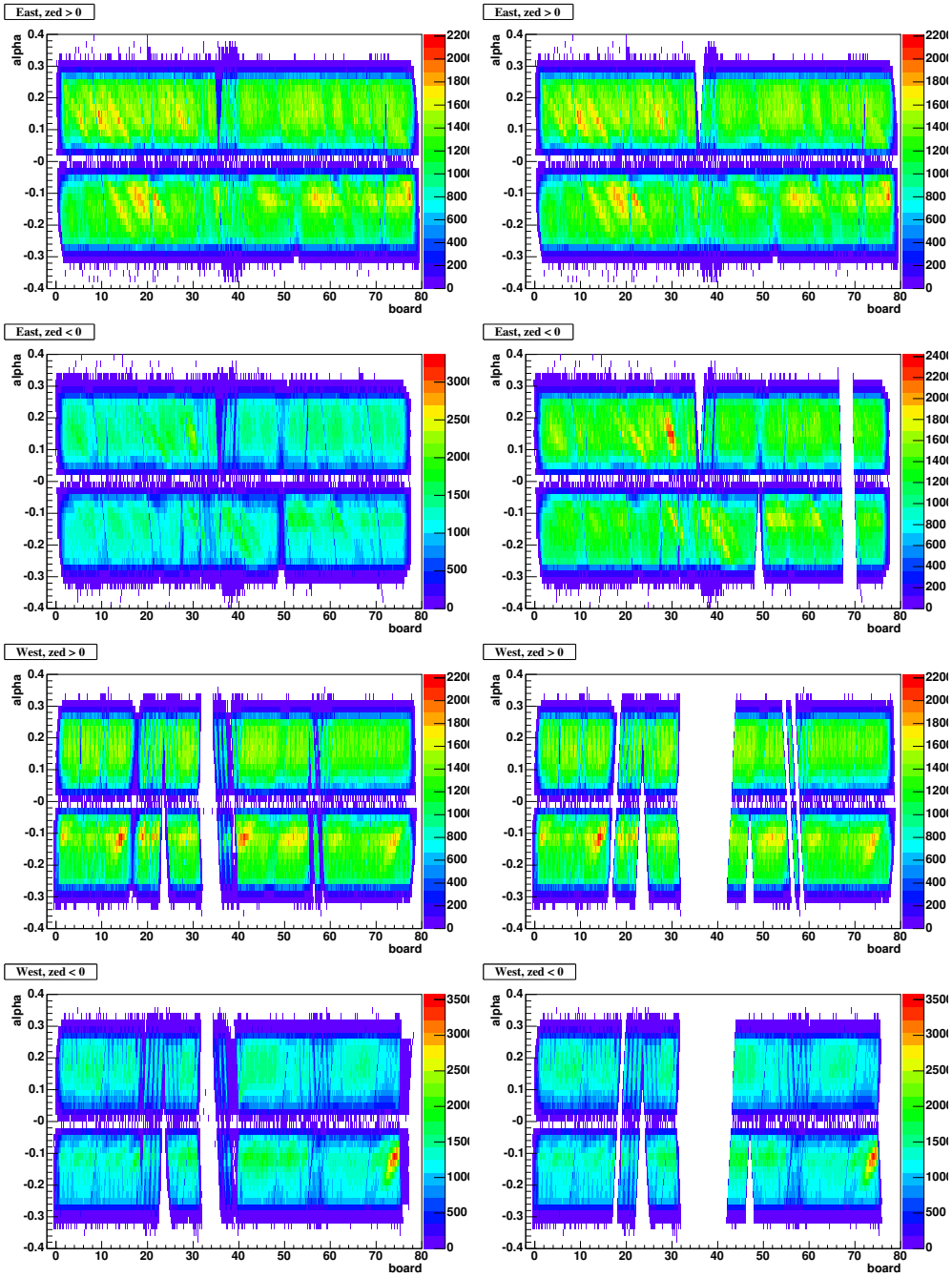

Figure 4.10: **Left**: The hit counts in (alpha, board) bins for East/West Arms and $zed > 0/zed < 0$ positions in 50 runs at the end before fiducial cut. **Right**: Same as the left plots after fiducial cut.

m^2 is given by

$$m^2 = p^2 \left(\frac{t^2 c^2}{d^2} - 1 \right), \tag{4.6}$$

where d is the path length of particles. The error in m^2 can be expressed as

$$\sigma_{m^2}{}^2 = \frac{\sigma_\alpha{}^2}{K_1{}^2}(4m^2p^2) + \frac{\sigma_{ms}{}^2}{K_1{}^2}\left[4m^2\left(1+\frac{m^2}{p^2}\right)\right] + \frac{\sigma_{tof}{}^2 c^2}{L^2}\left[4p^2\left(m^2+p^2\right)\right] \tag{4.7}$$

where $K_1 = \int_{0.3/R_{DC}} lBdl = 87$ mrad GeV, σ_α is the angular resolution of the central tracking detector, σ_{ms} is the angular smearing due to multiple scatterings and σ_{tof} is the TOF resolution. With σ_α and σ_{ms}, the momentum resolution of the central tracking can be expressed as

$$\left(\frac{\delta p}{p}\right)^2 = \left(\frac{\sigma_\alpha}{K_1} p\right)^2 + \left(\frac{\sigma_{ms}}{K_1 \beta}\right)^2 \tag{4.8}$$

The m^2 was calculated for positive and negative particles at eight momentum bins. Figure 4.11 shows the m^2 distributions obtained from the real data. The peaks of $\pi^\pm$, $K^\pm$ and $p^\pm$ were fitted to a Gaussian + polynomial (2nd order for real data and 1st order for simulation) function to obtain the mean (m^2) and width (σ_{m^2}) of the peaks. The σ_{m^2} of $\pi^\pm$, $K^\pm$ and $p^\pm$ at all momentum bins were fitted to the formula above with σ_α, σ_{ms} and σ_{tof} being free parameters. The σ_α, σ_{ms} and σ_{tof} were evaluated for positive and negative particles separately.

Figure 4.12 shows the m^2, σ_{m^2} and momentum resolution as a function of momentum. The deviation of m^2/m^2_{PDG}[14] from 1.0 is caused by discrepancies of the momentum scale and the TOF offset. The deviation caused by a discrepancy of the momentum scale must be momentum independent. The deviation caused by a discrepancy of the TOF offset must increase as the momentum increases, and must be larger for heavier particles. These two facts indicate that a 1.5% momentum scale error, which makes 3% error in m^2, is sufficient to explain the momentum-independent deviation.

The same analysis has been done for the simulation in order to assure that the simulation condition matches the real one. A data set of input $\pi^\pm$, $K^\pm$ and $p^\pm$ was generated with flat distributions in p_T, η and ϕ. An additional smearing by $\sim$1% on simulated momentum was applied. Figure 4.13 shows the m^2, σ_{m^2} and momentum resolution of the tuned simulation. It agrees with the result of the real data well.

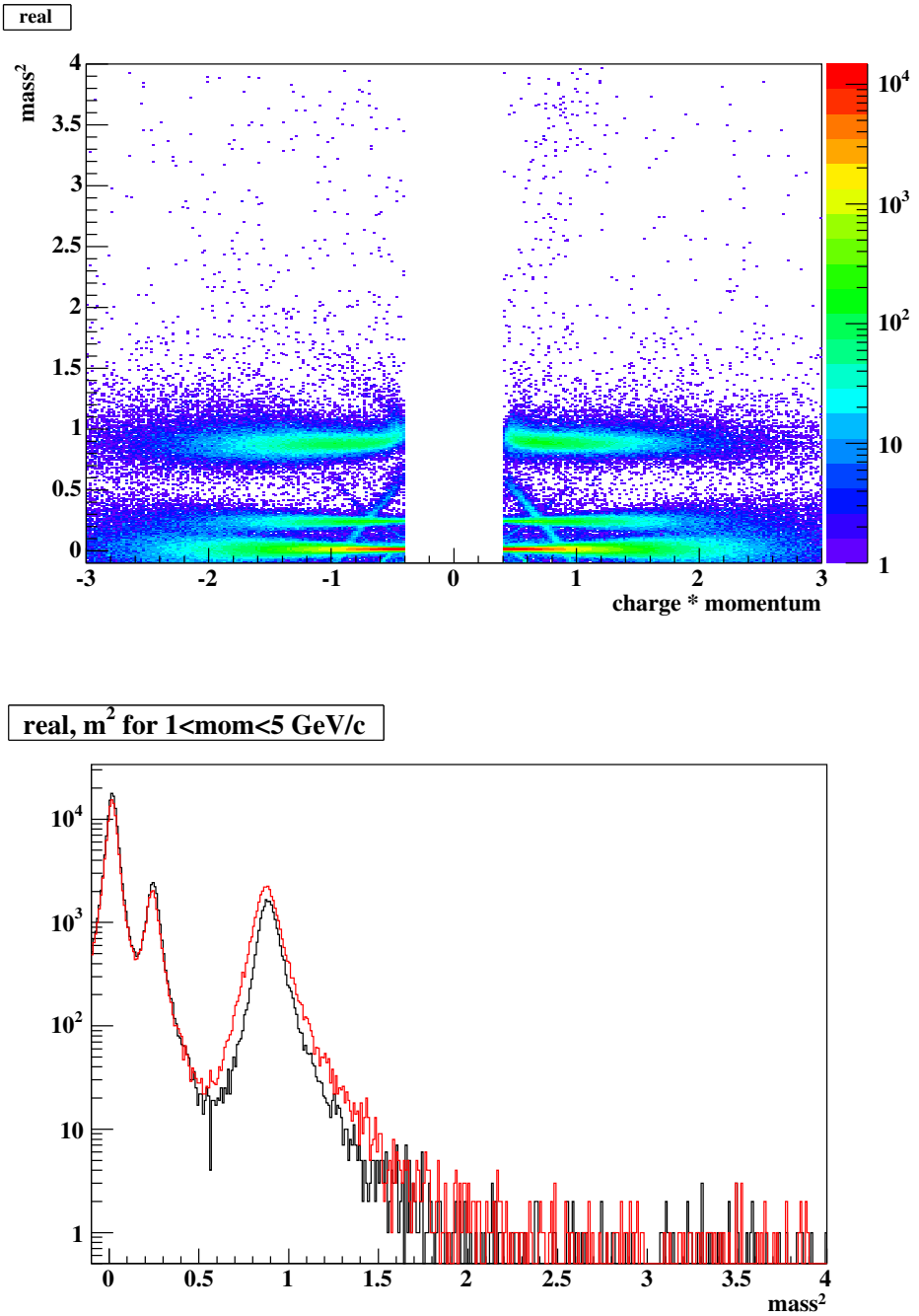

Figure 4.11: **Top**: m^2 vs momentum. **Bottom**: m^2 distribution for positive (**black**) and negative (**red**) particles.

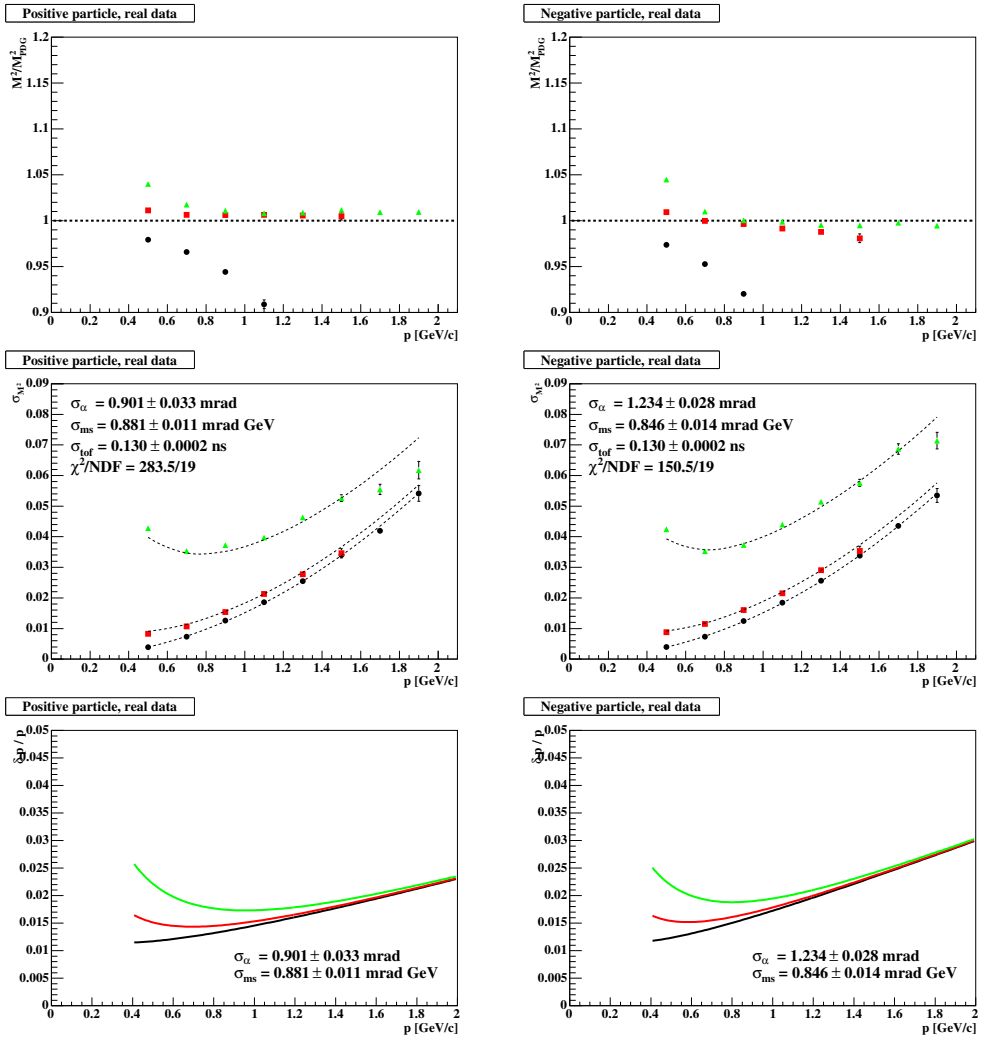

Figure 4.12: Identified charged particles with the real data. **Top**: m^2/m^2_{PDG}[14], **Middle**: σ_{m^2}, **Bottom**: Momentum resolution calculated with σ_α and σ_{ms}. **Left**: positive particles, **Right**: negative particles. **Black**: $\pi^\pm$, **Red**: $K^\pm$, **Green**: $p^\pm$.

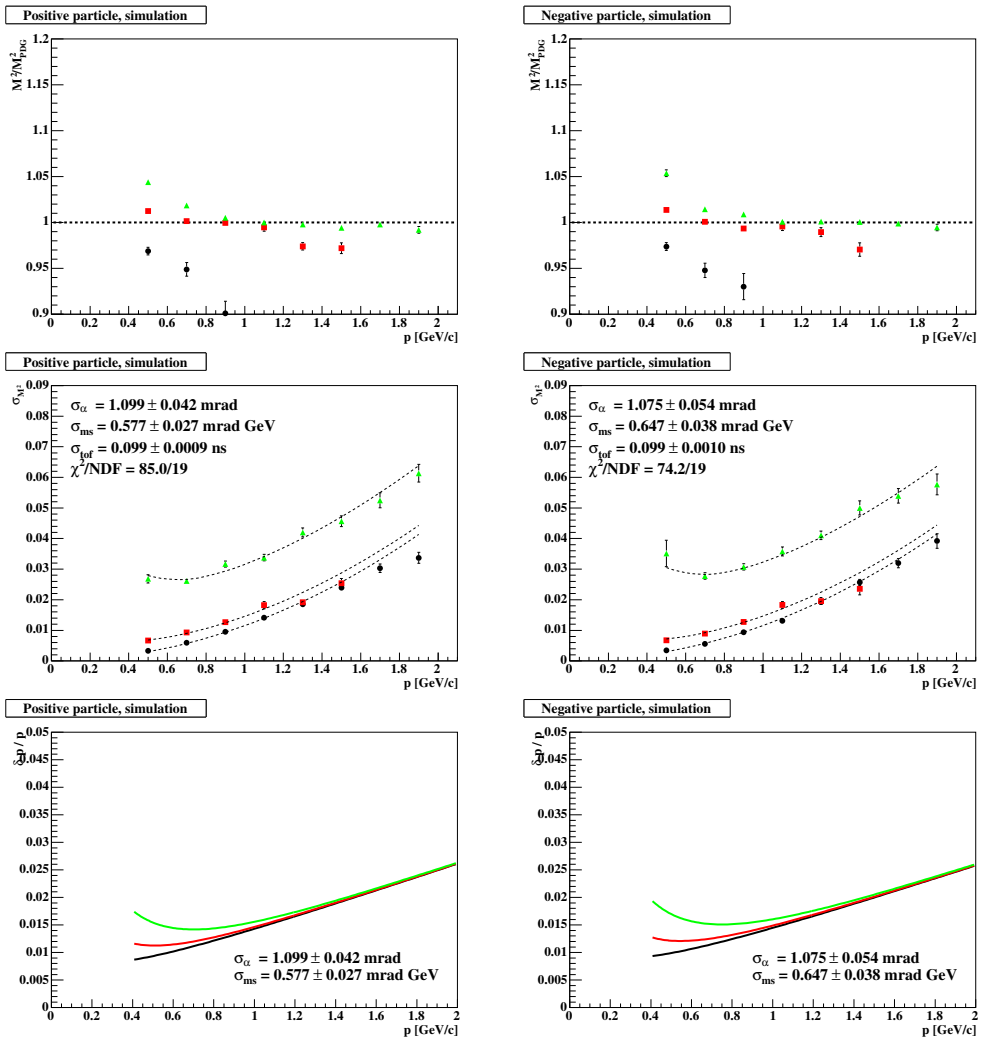

Figure 4.13: Identified charged particles with the simulation.

4.3.3 Run dependence of the summed transverse momentum

The summed transverse momentum $p_T^{\rm sum}$ is defined as

$$p_T^{\rm sum} \equiv \left| \sum_{i \in {\rm arm}} p_T^i \right| \tag{4.9}$$

where the sum over i is performed over particles detected with a single arm in each event. The number of events with certain $p_T^{\rm sum}$ values was compared between runs to search for bad (noisy or silent) runs. Event yields were normalized by the number of offline triggered ($p_T^{\rm ph} > 2$ GeV/c) events. The binning of $p_T^{\rm sum}$ was 0.4∼1, 1∼2, 2∼3, 3∼5, 5∼8, 8∼12, 12∼20 GeV/c. Photon-$p_T^{\rm sum}$ and charged-$p_T^{\rm sum}$ were checked separately. Figure 4.14 and 4.15 shows the normalized event yields in each photon- or charged-$p_T^{\rm sum}$ bin. All runs were found to be stable in terms of $p_T^{\rm sum}$. The χ^2/NDF of the photon-$p_T^{\rm sum}$ at $2 < p_T^{\rm sum} < 3$ GeV/c was smaller than 1.0 because the normalization factor was strongly correlated with the event yields.

4.4 Particle Clustering with Cone Method

One particle cluster in one arm is constructed with photons and charged particles detected with the EMCal, the DC and the PC1 of the Central Arms. A seed-cone algorithm is used for the cluster finding.

4.4.1 Particle selection

To select the energy region where the efficiency of the ERTLL1_4x4c trigger is plateau, it was required that at least one photon with $p_T > 2.0$ GeV/c existed in each event. The requirement causes the bias that a jet includes mostly high-p_T π^0, η, etc. or partly fragmentation (radiated) photon.

To select true photon signals from all EMCal clusters, a p_T cut, a charged track veto, and an electro-magnetic shower shape cut were applied. The p_T cut reduces low energy noise and was set to > 0.4 GeV/c. The charged track veto reduces charged particle contaminations and was performed by checking whether each EMCal cluster has a matched charged track within 3σ of their position resolutions. The shower shape cut reduces hadron contaminations by requiring a photon probability of > 0.01.

To select true charged particle signals from all tracks, a p_T cut and the usual track quality cut (= 31 OR $\geq$ 61) were applied. The p_T cut was set to $0.4 < p_T < 4.0$ GeV/c. Below the lower limit the acceptance is strongly

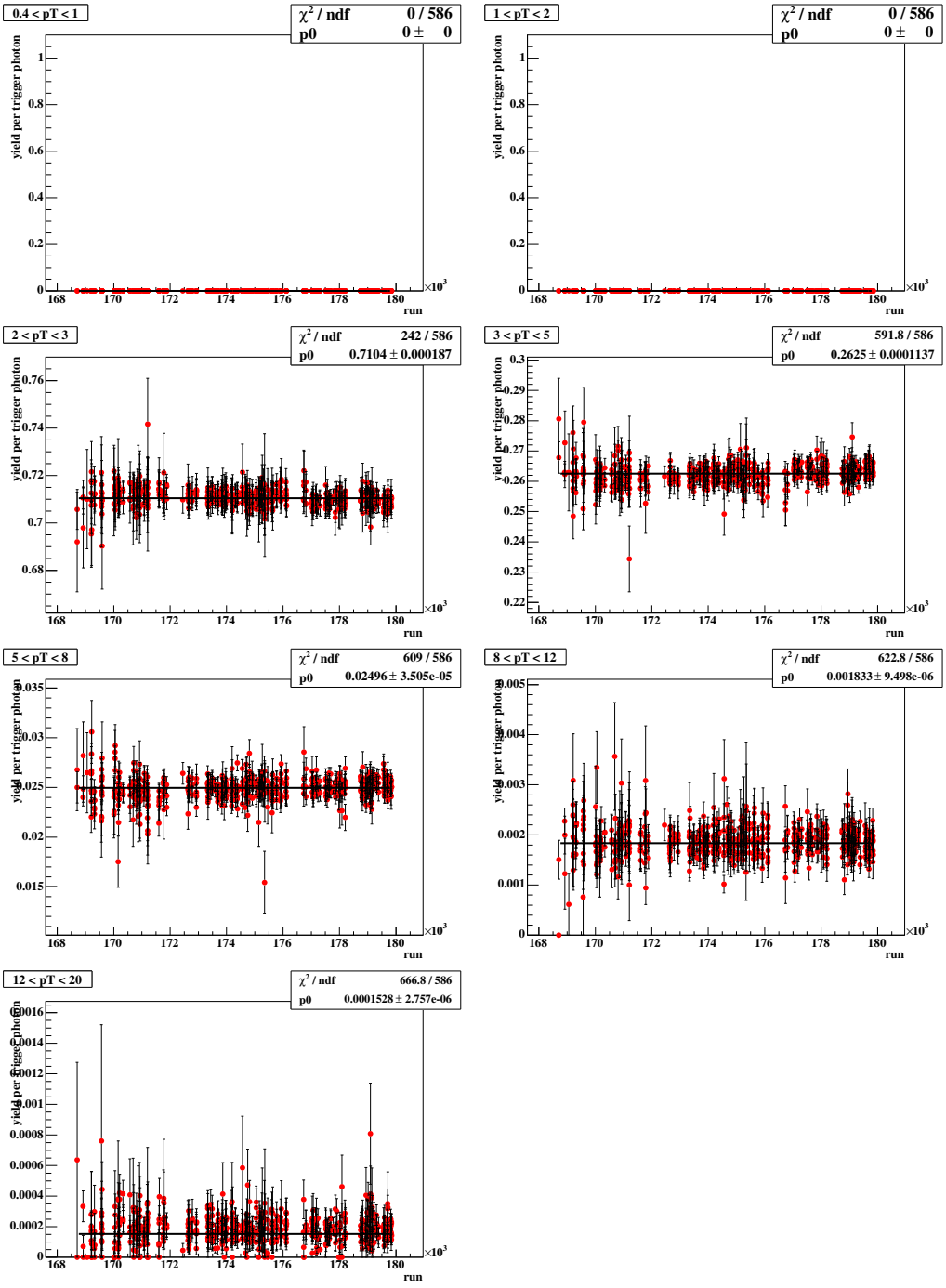

Figure 4.14: Event yields normalized with the number of offline triggered events at each photon-$p_T^{\rm sum}$ bin.

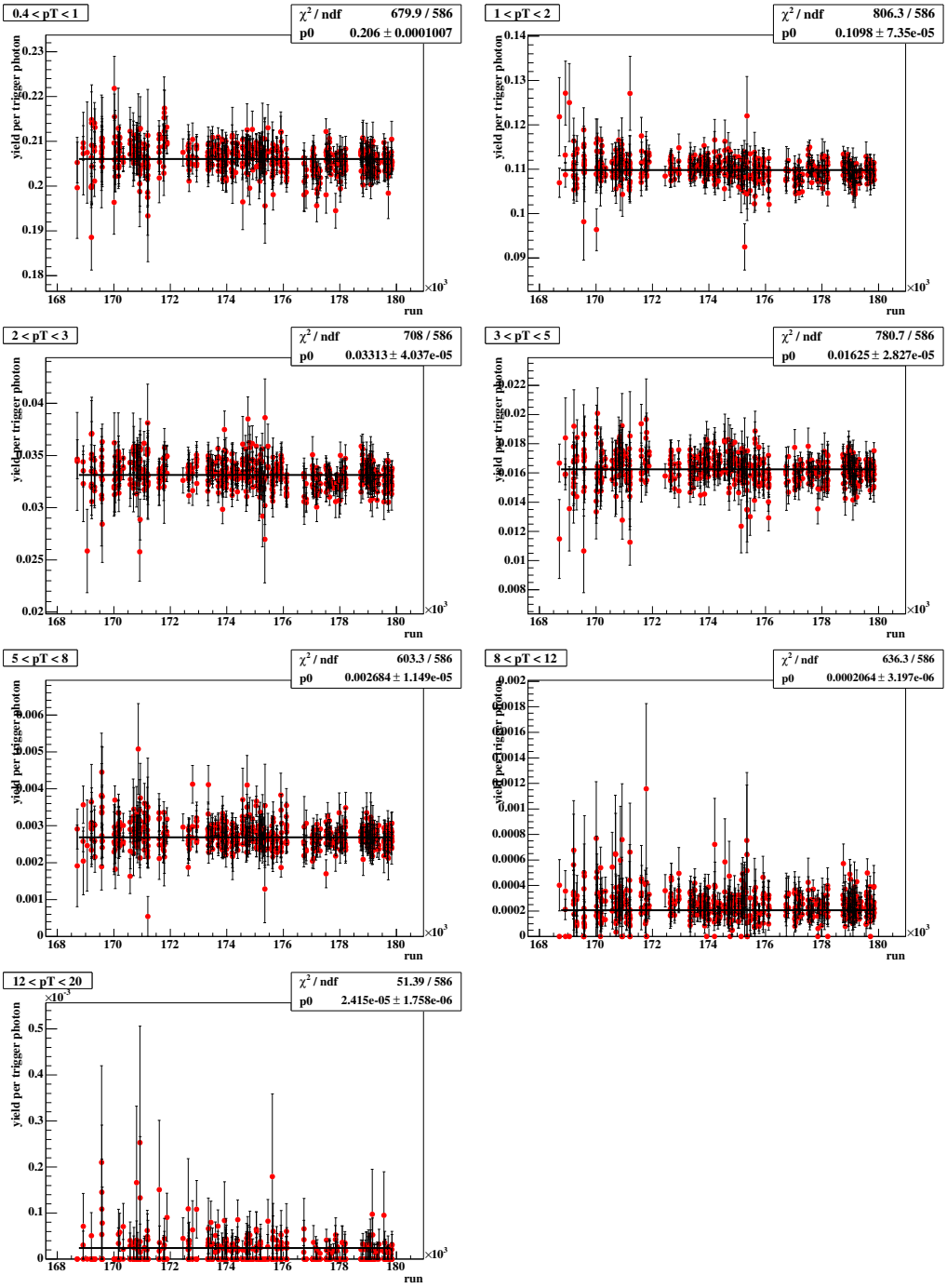

Figure 4.15: Event yields normalized with the number of offline triggered events at each charged-$p_T^{\rm sum}$ bin.

distorted due to large bending angle. The upper limit eliminates fake high-p_T tracks, which originate from low-p_T particles that are produced from a decay in the magnetic field.

4.4.2 Cluster finding algorithm

All particles that satisfied the experimental cuts in one arm were used as a seed to determine the cone axis. Starting with the momentum direction of a seed particle as a temporal cone axis, we calculated the next temporal cone axis with particles which were in the cone. The distance between the cone axis (η^C, ϕ^C) and the momentum direction of each particle (η^i, ϕ^i) is defined as

$$R^i \equiv \sqrt{(\eta^i - \eta^C)^2 + (\phi^i - \phi^C)^2} \tag{4.10}$$

The cone radius R was set to 0.3, which was about a half of the η acceptance. The cone size is smaller than the typical one (~ 0.7), but the simulation study described later showed that even this small cone can collect $\sim 80\%$ of jet p_T on average. The next temporal cone axis is calculated as a vector sum of momenta of particles in the cone.

$$\vec{p}^{\,\text{cone}} \equiv \sum_{i \in \text{cone}} \vec{p}_i \tag{4.11}$$

$$\vec{e}_{\text{cone}} \equiv \frac{\vec{p}^{\,\text{cone}}}{|\vec{p}^{\,\text{cone}}|} \tag{4.12}$$

This procedure was iterated until the temporal cone axis became stable.

The cluster finding is done with all seed particles, and then each seed particle has one cone and some of cones can be the same or overlapped. The cone which has the largest p_T^{cone} in an event is used in the event.

An evaluation of p_T^{cone} without seed has been done using a part of the statistics in order to check the effect of the use of seed. The initial direction of cone was scanned over all the PHENIX Central Arm acceptance ($|\eta| < 0.35$, $\Delta\phi = 90^\circ \times 2$) with a step of $\delta\eta = \delta\phi = 0.01$ in each event. The p_T^{cone} distribution with the seedless method was larger than that with the seed method by $\sim$20% at $p_T^{\text{cone}} = 4$ GeV/c, $\sim$10% at $p_T^{\text{cone}} = 8$ GeV/c and $\sim$5% at $p_T^{\text{cone}} = 12$ GeV/c. The deviation is compensated in the relation between measured jet core and original jet estimated with the simulation, and therefore the p_T^{cone} difference between the cluster finding methods is smaller than the deviation above.

4.4.3 Remaining hadron contribution

Among hadrons remaining after the particle selections, antineutron ($\bar{n}$) makes the largest contribution to the photon component of $p_T^{\rm cone}$ because of the neutrality and the reaction with n or p in the EMCal material. The fraction of $\bar{n}$-origin clusters after the particle selections is ∼20% at $E_{cluster} = 1$ GeV, ∼1% at $E_{cluster} = 3$ GeV and ∼0.1% at $E_{cluster} = 8$ GeV, which has been estimated with a GEANT simulation tuned with the EMCal response to identified $\bar{p}$s. In the simulation, the sum of p_T of $\bar{n}$-origin clusters in cone was excluded from $p_T^{\rm cone}$, and as a result the cone yields at $4 < p_T^{\rm cone} < 10$ GeV/c decreased only by 0.02%. Therefore the $\bar{n}$ contribution is negligible.

Because the live area of the DC and PC1 is ∼90%, a part of EMCal clusters made by charged particles was not eliminated by the charged track matching. The fraction of clusters which match to a charged track is ∼40% at $E_{cluster} = 0.4$ GeV and ∼4% at $E_{cluster} = 4$ GeV. Therefore the remaining charged-particle-origin clusters are $40\% \times (1 - 90\%) = 4\%$ of all clusters at $E_{cluster} = 0.4$ GeV, and is also negligible.

4.4.4 $p_T^{\rm cone}$ distribution

Figure 4.16 shows the distribution of $p_T^{\rm cone}$ measured with the clustering method above. The simulation outputs have been normalized so that they matched to the real data result at $p_T = 5$ GeV/c. Therefore the difference in only p_T slope between the real data and the simulation outputs can be studied.

The slope of the PYTHIA MPI output is consistent within 10% with that of the real data at all p_T range. The slope of the PYTHIA default output is less steep.

4.5 Simulation Study

The particle cluster measured with the cone method is a part of an original jet, not the whole jet. The relation between particle clusters and jets has been studied with the PYTHIA+GEANT full simulation.

4.5.1 Relating cone to jet

In the scheme of PYTHIA hadron+hadron collisions, a hard-scattered parton (from partonic $2 \to 2$ scattering) is first split into several partons as a sequence of $1 \to 2$ branchings up to a certain cut-off scale (by default, the invariant mass of two branched partons $m < 1$ GeV). Then Lund color

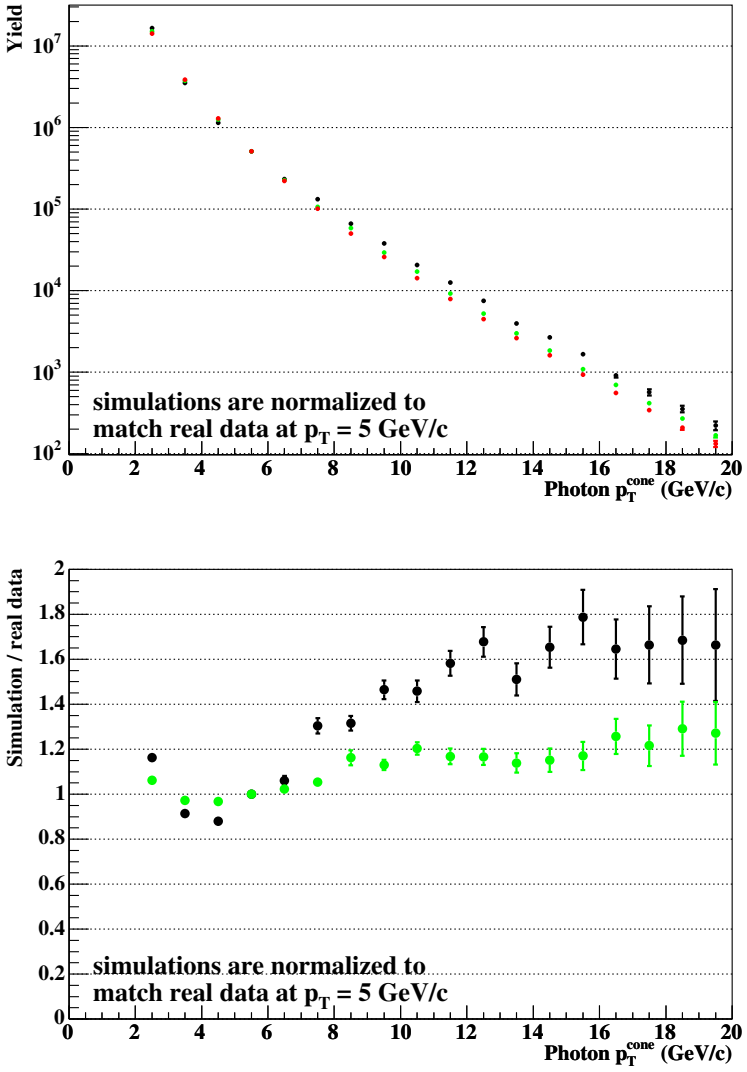

Figure 4.16: **Top**: p_T^{cone} distributions. The red, black and green points correspond to the real data, the PYTHIA default output and the PYTHIA MPI output, respectively. The simulation outputs have been normalized so that they matched the real data result at $p_T = 5$ GeV/c. **Bottom**: The difference of p_T^{cone} between the real data and the simulations.

strings are generated between the partons and fragment into hadrons, some of which decay like $\pi^0 \to \gamma\gamma$. All stable particles at the final state are input into the GEANT simulator, and converted to detected particles. The detected particles are clustered with the cone method.

For a measured cone, one of two hard-scattered partons, which are of particle number 7 or 8 in PYTHIA event list, is selected as an original jet of the measured cone with the condition that the angle between the cone momentum and the parton momentum, $\Delta R = \sqrt{\Delta\eta^2 + \Delta\phi^2}$, is smaller than the others. The calculation of QCD hard scatterings in the PYTHIA is at leading order, although the PYTHIA phenomenologically adopts higher order effects such as initial/final-state radiations. Therefore the jet that is related to the measured cone with the method above is what is basically defined at leading order. On the other hand, the unpolarized cross section and A_{LL} of jet production that is compared with A_{LL} measured in this analysis have been calculated at the next-leading order. Therefore the definitions of the jet and thus its p_T in the PYTHIA simulation and the theory are not identical to each other. To minimize the difference in $p_T^{\rm jet}$ between the simulation and the theory, the cone radius R in the theory was set to the largest, $R = 1$, which is the limit value where the Small Cone Approximation can apply. The uncertainty on $p_T^{\rm jet}$ was estimated from the dependence of jet cross section on the cone radius. Figure 4.17 shows the R dependence of the unpolarized jet cross section. The difference in cross section between $R = 1$ and $R = 0.1$ is 60% of the value at $R = 1$. The difference in cross section can be expressed as the difference in p_T scale since a smaller cone radius causes a more p_T leak from the cone. Assuming that the R dependence at $R > 1$ is smaller than that at $R < 1$, we assigned the 10% difference to the p_T scale uncertainty, which covers the 60% cross section variation.

The relation between $p_T^{\rm cone}$, which is the value measured in the experiment, and $p_T^{\rm jet}$, which is the value calculated in the theory, has been evaluated using the PYTHIA+GEANT simulation. Figure 4.18 shows the event fractions in each $p_T^{\rm cone}$ and $p_T^{\rm jet}$ bin.

4.5.2 Bias of cone measurement

The relation between cones and jets can be characterized by

- p_T leak from cone and p_T contamination from the underlying event,
- p_T smearing, and
- biases due to high-p_T photon and small cone.

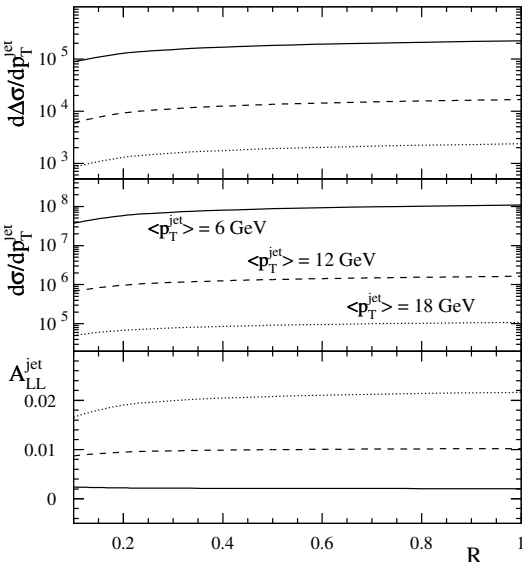

Figure 4.17: Cone radius R dependence of the polarized and unpolarized jet cross section and the corresponding spin asymmetry at NLO for $\sqrt{s} = 200$ GeV integrated over $-1 < \eta^{\rm jet} < 1$.

The leak and contamination of p_T

Since the acceptance is limited and the size of the cone is small, some particles in a jet can leak from the cone. Some particles produced in interactions between beam remnants can go into the cone and contaminate $p_T^{\rm cone}$.

The p_T smearing

$p_T^{\rm jet}$ of events that are in a $p_T^{\rm cone}$ bin is distributed widely due to the finite $p_T^{\rm jet}$ resolution of the PHENIX Central Arm. It is difficult to unfold the cone yield vs $p_T^{\rm cone}$ into the jet yields vs $p_T^{\rm jet}$ because the relation between $p_T^{\rm cone}$ and $p_T^{\rm jet}$ is not diagonal and thus unfolding methods do not work stably.

The biases due to high-p_T photon and small cone

This bias is due to the fact that gluon jet is softer and broader than quark jet[77][78]. Because of the softness of gluon jets, the high-p_T photon requirement has lower efficiency for gluon jets. Because of the broadness of gluon jets, the ratio of $p_T^{\rm cone}$ to $p_T^{\rm jet}$ for gluon jets is smaller on average. Figure 4.19 shows the ratio $p_T^{\rm cone}/p_T^{\rm jet}$ for each subprocess estimated with the PYTHIA simulation. Clearly the ratio in gg subprocess is smaller than others particu-

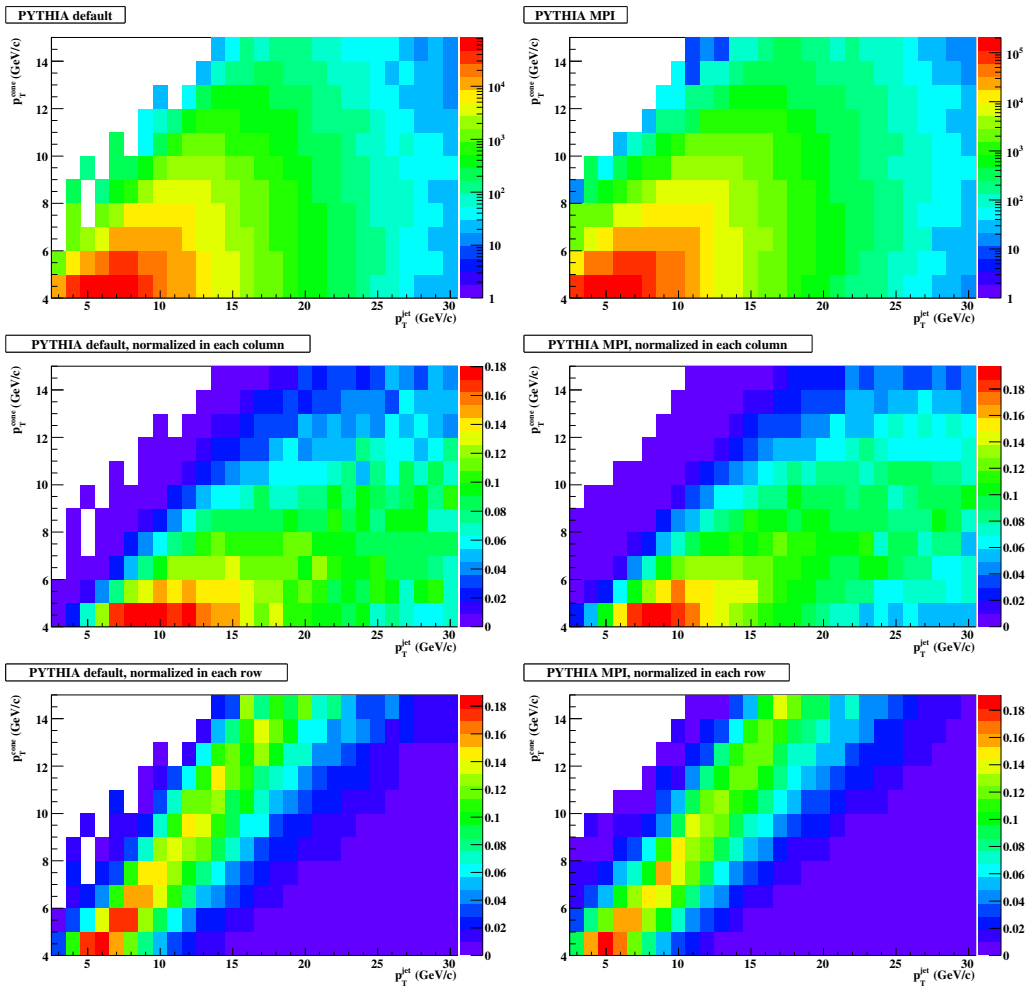

Figure 4.18: **Top**: p_T^{cone} vs p_T^{jet} evaluated with the PYTHIA default (**Left**) and the PYTHIA MPI (**Right**). **Center**: Same as the top plots but are normalized in each column (p_T^{jet}) bin. **Bottom**: Same as the top plots but are normalized in each row (p_T^{cone}) bin. The normalization in each row or in each column included underflow and overflow bins.

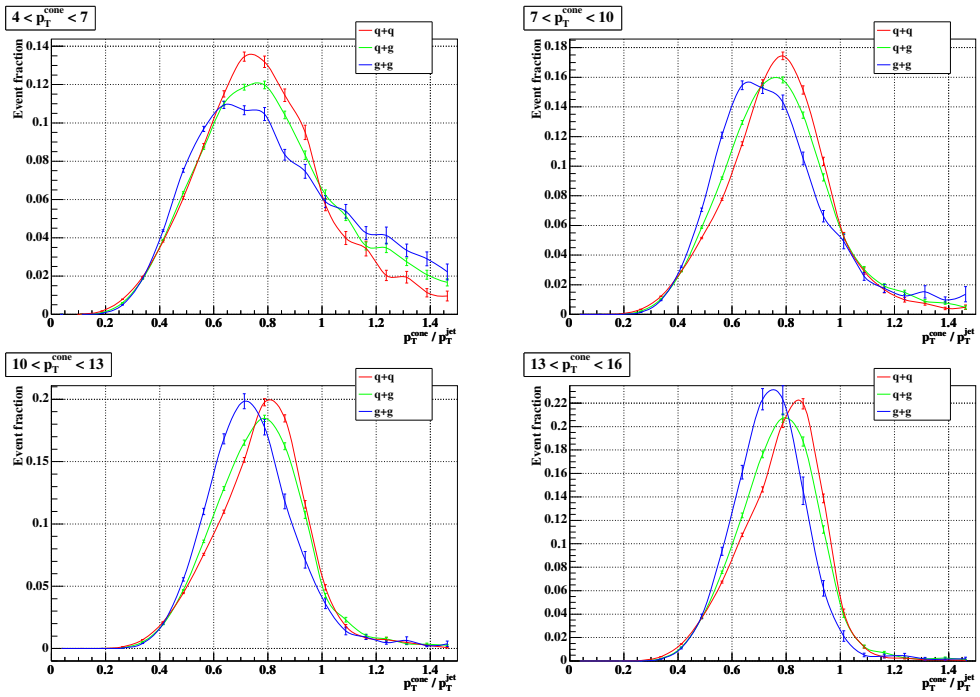

Figure 4.19: The ratio of p_T^{cone} to p_T^{jet} for each subprocess at four different p_T^{cone} bins. It was estimated with the PYTHIA MPI simulation.

larly at higher $p_T^{\rm cone}$. These effects suppress the fraction of the gg subprocess as appeared in the middle plot of Fig. 2.14.

4.6 Event structure

4.6.1 Multiplicity

Multiplicity is defined as the number of particles which satisfied the experimental cuts in one event.

4.6.2 Transverse momentum density

The p_T density, $\mathcal{D}_{P_T}(\Delta\phi)$, is defined as

$$\mathcal{D}_{p_T}(\Delta\phi) \equiv \left\langle \frac{1}{\delta\phi \cdot \delta\eta} \sum_{i \text{ in } [\Delta\phi,\ \Delta\phi+\delta\phi]} p_{Ti} \right\rangle_{\text{event}} \tag{4.13}$$

where $\Delta\phi$ is ϕ angle with respect to the direction of a trigger photon in event, $\delta\phi$ and $\delta\eta$ are area widths in ϕ and η direction ($\delta\eta = 0.7$), and p_{Ti} is transverse momentum of i-th particle in event. Therefore the p_T density means the area-normalized total transverse momentum in an area of $\delta\phi \times \delta\eta$ at a distance $\Delta\phi$ from trigger photon.

We name the region at $\Delta\phi \lesssim 0.7$ 'toward' region and the region at $\Delta\phi \gtrsim 0.7$ 'transverse' region (see Fig. 4.20). Since particles from a jet are concentrated along the jet direction, the $\mathcal{D}_{p_T}$ at the transverse region are sensitive to the underlying events.

To avoid the effect of the PHENIX Central Arm acceptance in the calculation of $\mathcal{D}_{p_T}$, we limited the ϕ direction of trigger photons to less than 20° from the edge of the PHENIX Central Arms, and didn't use photons and charged particles which were in the ϕ area between the trigger photon and the near edge. With this method the $\mathcal{D}_{p_T}$ distribution is not affected by the finite acceptance of the PHENIX Central Arms up to 70° (~ 1.2 rad).

4.6.3 Thrust distribution in PHENIX Central Arm

Thrust T represents the topology of particles in one event, and is defined as

$$T \equiv \max_{\boldsymbol{u}} \frac{\sum_i |\boldsymbol{p}_i \cdot \boldsymbol{u}|}{\sum_i |\boldsymbol{p}_i|} \tag{4.14}$$

Here, $\boldsymbol{u}$ is a unit vector which is called the thrust axis and is directed to maximize T, and $\boldsymbol{p}_i$ is a momentum of each particle in one arm. T is equal

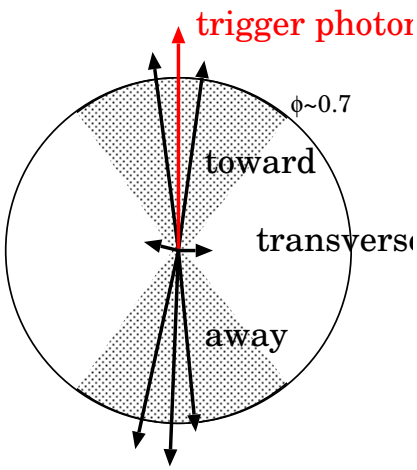

Figure 4.20: Toward and transverse region in ϕ space with respect to the direction of a triggered photon.

to one when all $\boldsymbol{p}_i$ are collinear, and T decreases as the jet cone size increases (see Fig. 4.21). The above equation is approximately equal to

$$T = \frac{\sum_i |\boldsymbol{p}_i \cdot \hat{\boldsymbol{p}}|}{\sum_i |\boldsymbol{p}_i|} \tag{4.15}$$

$$\hat{\boldsymbol{p}} = \frac{\sum_i \boldsymbol{p}_i}{|\sum_i \boldsymbol{p}_i|} \tag{4.16}$$

Here, $\hat{\boldsymbol{p}}$ is the unit vector of the sum of $\boldsymbol{p}_i$. This equation can be calculated without iterations to determine the thrust axis.

We defined and evaluated a PHENIX thrust, T_{PH}, with particles in one arm ($\Delta\eta = 0.7$, $\Delta\phi = 90^{\circ}$) as

$$T_{PH} = \frac{\sum_i |\boldsymbol{p}_i \cdot \hat{\boldsymbol{p}}|}{\sum_i |\boldsymbol{p}_i|} \tag{4.17}$$

$$\hat{\boldsymbol{p}} = \frac{\sum_i \boldsymbol{p}_i}{|\sum_i \boldsymbol{p}_i|} \tag{4.18}$$

In the PHENIX Central Arm acceptance, $\Delta\eta = 0.7$ and $\Delta\phi = 90^{\circ}$, the mean value of the thrust of high-multiplicity isotropic events is equal to 0.88 (see Fig. 4.21).

The PHENIX thrust distribution of isotropic events in the PHENIX Central Arm acceptance for each $p_T^{\rm sum}$ bin was calculated with the following method. First, the particle production cross section is assumed to be proportional to $\exp(-6\ p_T(\mathrm{GeV}/c))$ and is independent of η and ϕ. Second,

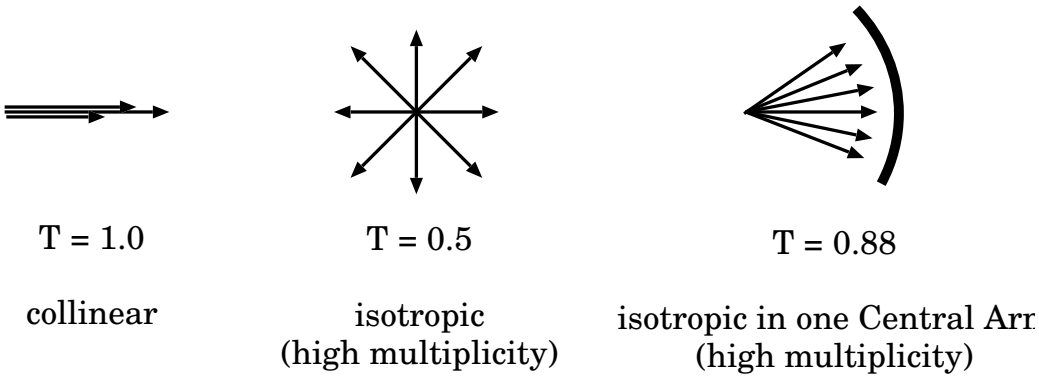

Figure 4.21: Thrust value in the case of collinear ($T = 1.0$), isotropic ($T = 0.5$), and isotropic in one Central Arm ($T = 0.88$).

the similar cuts to the experiment are applied numerically; the geometrical acceptance ($|\eta| < 0.35$, $\Delta\phi = 90^{\rm o}$), the momentum limit ($p_T > 0.4$ GeV/c), and one high-p_T particle ($p_T > 2.0$ GeV/c). The magnitude of $p_T^{\rm sum}$ is ignored and all simulated events are used in the calculation for each $p_T^{\rm sum}$ bin. Therefore, the effect of the high-p_T particle can be stronger than the actual case at particularly high-$p_T^{\rm sum}$ range. Third, the PHENIX thrust distribution of isotropic events was calculated for each number of particles in one event ($f_n(T)$ for $n = 1, 2, 3, \dots$). Figure 4.22 shows $f_n(T)$ distributions for $n = 2 \sim 7$. Particularly the thrust distribution of $n = 2$ events is steep. Thus we applied a cut of $n \geq 3$ in the T_{PH} measurement. The f_T is evaluated as the sum of $f_n(T)$s weighted by the fraction of n-particle events to total events;

$$f(T) = \sum_n \epsilon_n f_n(T) \quad , \quad \epsilon_n = \frac{N^n_{\rm evt}}{N_{\rm evt}} \tag{4.19}$$

4.7 Cone production rate

4.7.1 Evaluation method

The cone production rate $\mathcal{Y}$, namely the cone yield per luminosity, is defined with measured quantities as

$$\mathcal{Y}^{ic} \equiv \frac{N^{ic}_{cone}}{L \cdot f_{BBC} \cdot f_{ERT}} \tag{4.20}$$

where L is the integrated luminosity; f_{BBC} is the BBC trigger efficiency in the high-p_T photon trigger; f_{ERT} is the the live area of the ERTLL1_4x4c

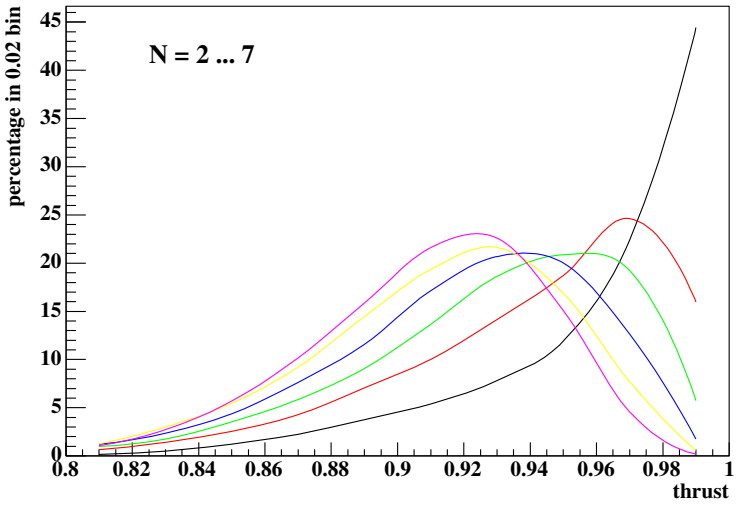

Figure 4.22: Thrust distribution for isotropic events with $N = 2 \sim 7$ in the PHENIX Central Arm acceptance. As the number of particles increases ($2 \rightarrow 7$), the mean value of thrust becomes smaller (black $\rightarrow$ purple).

trigger; N^{ic}_{cone} is the cone yield in a ic-th $p_T^{\rm cone}$ bin.

The $\mathcal{Y}$ is defined with theory and simulation quantities as

$$\mathcal{Y}^{ic} \equiv \sum_{ij} f^{ic,ij} \cdot \epsilon^{ij}_{trig+acc} \cdot \mathcal{Y}^{ij}_{theo} \tag{4.21}$$

where the label ic and ij are the indices of $p_T^{\rm cone}$ and $p_T^{\rm jet}$ bins, respectively. The $\mathcal{Y}^{ij}_{theo}$ is a jet production rate within $|\eta| < 0.35$ in a ij-th $p_T^{\rm jet}$ bin, which is calculated from the jet cross section. The $\epsilon^{ij}_{trig+acc}$ is a high-p_T-photon trigger efficiency and acceptance correction, which is evaluated with the simulation. The $\epsilon^{ij}_{trig+acc} \cdot N^{ij}_{theo}$ is a yield of jets that include a high-p_T photon within $|\eta| < 0.35$. The $f^{ic,ij}$ is the probability that a photon-included jet within a ij-th $p_T^{\rm jet}$ bin is detected as a cone within a ic-th $p_T^{\rm cone}$ bin. The $f^{ic,ij}$ is shown at the center row of Fig. 4.18. This method uses the relative $p_T^{\rm cone}$ distribution in each $p_T^{\rm jet}$ bin and thus the slope of $p_T^{\rm jet}$ distribution in the simulation doesn't affect the result of $\mathcal{Y}^{ic}$.

Below the methods of evaluating L and $\epsilon^{ij}_{trig+acc}$ are described.

4.7.2 Luminosity in measurement

The integrated luminosity of the analyzed data was evaluated as

$$L = \sigma_{BBC} \cdot \sum_{irun} F^{irun} N^{irun}_{BBC} \tag{4.22}$$

where σ_{BBC} is the cross section of the BBCLL1 trigger, namely the proton-proton total cross section multiplied by the BBCLL1 trigger efficiency; F^{irun} is the prescale factor of the BBCLL1 trigger, which can vary between the runs; N^{irun}_{BBC} is the number of scaled BBCLL1 trigger counts with the offline 30 cm z-vertex cut in run $irun$, where the vertex cut has to be required because it is also required in the particle cluster measurement. In the RHIC Vernier scan, the BBCLL1 trigger was used to record the collision rate at the PHENIX interaction point since it is the minimum bias trigger. Therefore it is also used in evaluating the luminosity.

σ_{BBC} has been evaluated using Vernier scan data taken in 2002. It is defined as

$$\sigma_{BBC} \equiv \frac{R_{max}}{L_{effective}} = \frac{R_{max}}{L_{machine} \cdot \epsilon_{vertex}} = \frac{\sigma^{raw}_{BBC}}{\epsilon_{vertex}} \tag{4.23}$$

where R_{max} is the maximum rate of the BBCLL1 trigger, i.e. the trigger rate at $dx = 0$; $L_{effective}$ is the effective luminosity for the PHENIX; $L_{machine}$ is the total luminosity delivered to the PHENIX; ϵ_{vertex} is the efficiency of the offline z-vertex cut ($|z| < 30$ cm). The online z-vertex cut in 2002 was ± 75 cm. Because the longitudinal length of beam bunches was wider than the online z-vertex cut, collisions outside the region could occur and was included in the machine (accelerator) luminosity. Therefore the extra collisions have been corrected by ϵ_{vertex}. The raw value of R_{max} was the trigger rate with the online z-vertex cut, and thus it has been corrected by the fraction of events with the offline z-vertex cut. The systematic errors on σ_{BBC}, such as beam current, beam position, non-zero crossing angle and beam size blow-up, have been studied. σ_{BBC} was obtained to be $21.8 \pm 9.6\%$.

The BBC trigger efficiency in 2005 increased by $0.051 \pm 1.6\%$ from that in 2002 mostly due to changes of BBC HV setting, and thus σ_{BBC} changed to 22.9 mb $\pm$ 9.7%.

The integrated luminosity of the analyzed data was estimated to be 2.2 pb^{-1} $\pm$ 9.7%, where the error almost came from σ_{BBC}.

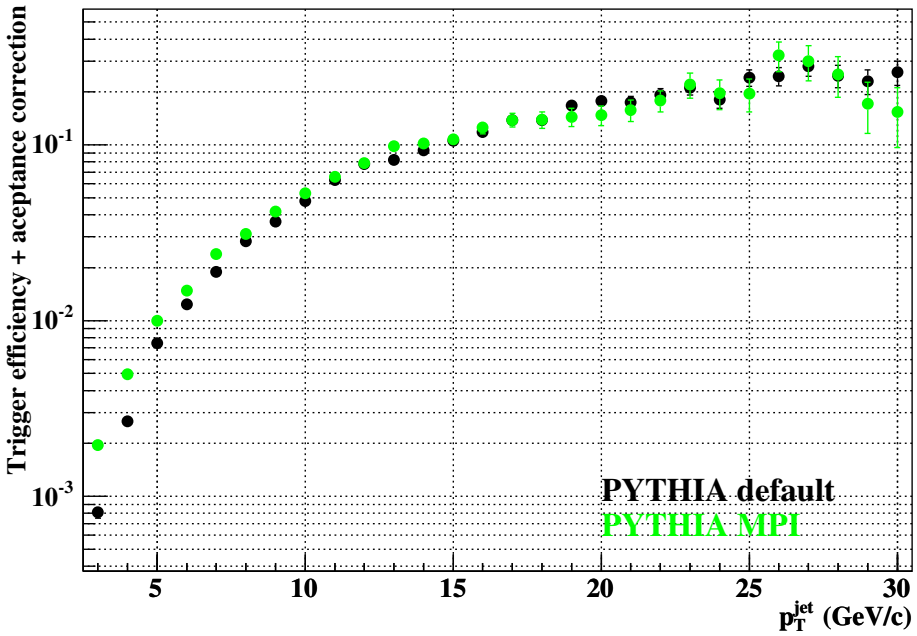

Figure 4.23: The correction factor $\epsilon^{ij}_{trig+acc}$ for high-p_T photon trigger efficiency and acceptance effect. The PYTHIA default (**Black**) and the PYTHIA MPI setting (**Green**) were used.

4.7.3 Trigger efficiency and acceptance correction in simulation

The high-p_T photon ($p_T > 2.0$ GeV/c) trigger efficency and acceptance correction ($\epsilon^{ij}_{trig+acc}$) were estimated using the PYTHIA+GEANT simulation. The high-p_T photon efficency is the probability that jets include a high-p_T photon which is detected with the EMCal. The acceptance in the experiment is not for jets but for trigger photons, and thus the acceptance correction means the correction from trigger photon acceptance to jet acceptance. The correction factor can be written as

$$\epsilon^{ij}_{trig+acc} = \frac{N^{ij}_{\rm jet} \text{ with } \left\{ p_T^{\rm ph} > 2 \text{ and } \{(\eta_{\rm ph}, \phi_{\rm ph}) \text{ in EMCal acceptance}\} \right\}}{N^{ij}_{\rm jet} \text{ with } \{|\eta_{\rm jet}| < 0.35\}} \tag{4.24}$$

Figure 4.23 shows $\epsilon^{ij}_{trig+acc}$ as a function of $p_T^{\rm jet}$ estimated with the PYTHIA default and MPI simulations.

4.7.4 Systematic error estimation

A systematic error on the cone production rate was estimated by comparing cone yields with and without the high-p_T-photon requirement in the real data and the simulations. The cone yields without the high-p_T-photon requirement in the real data was measured with the minimum bias (BBCLL1 trigger) sample.

The efficiencies of the BBCLL1 trigger and the ERTLL1_4x4c trigger haven't been included in the simulation. The BBCLL1 efficiencies on the high-p_T photon sample and the minimum bias sample for the real data are the same and thus cancel out. Since a high-p_T (> 2 GeV/c) photon is required to exist in each event, the efficiency of the ERTLL1_4x4c trigger is $\sim$100% except for the masked trigger tiles (4.34% in area). But the inefficiency is less than 4.34% for the particle cluster measurement because jet may include more than one high-p_T photons. The correction factor for the trigger efficiency was set to 0.975 ± 0.025, where the error covers all possible values.

Figure 4.24 shows cone yields vs $p_T^{\rm cone}$. The ratio (r) of the cone yields in the high-p_T photon sample to that in the minimum bias sample, and the difference of r between the real data and the simulation outputs are also shown. The r of the PYTHIA MPI output agrees with that of the real data within $\sim$10%. The r reflects not only the fragmentation function, which is related to the probability that a jet includes at least one high-p_T photon, but also the jet-cone relation, namely the $p_T^{\rm jet}$ distribution in each $p_T^{\rm cone}$ bin. If more events with lower $p_T^{\rm jet}$ contributes to a $p_T^{\rm cone}$ bin, the r becomes smaller since the probability that a lower-p_T jet includes high-p_T photon is smaller. It is the reason why the PYTHIA default shows the smaller r than the PYTHIA MPI although the fragmentation function is common. The similar tendency is seen in the $p_T^{\rm cone}$ distribution (Fig. 4.16), where the cone yield in the PYTHIA MPI simulation normalized with that of the real data yield is smaller at low $p_T^{\rm cone}$ than at high $p_T^{\rm cone}$ by $\sim$10%. It indicates that the 10% difference in r is due to mostly the difference in the cone yield of the high-p_T photon sample rather than the minimum bias sample. Therefore a 10% error was assigned to the cone production rate calculated using the PYTHIA MPI simulation, which uses the high-p_T photon sample.

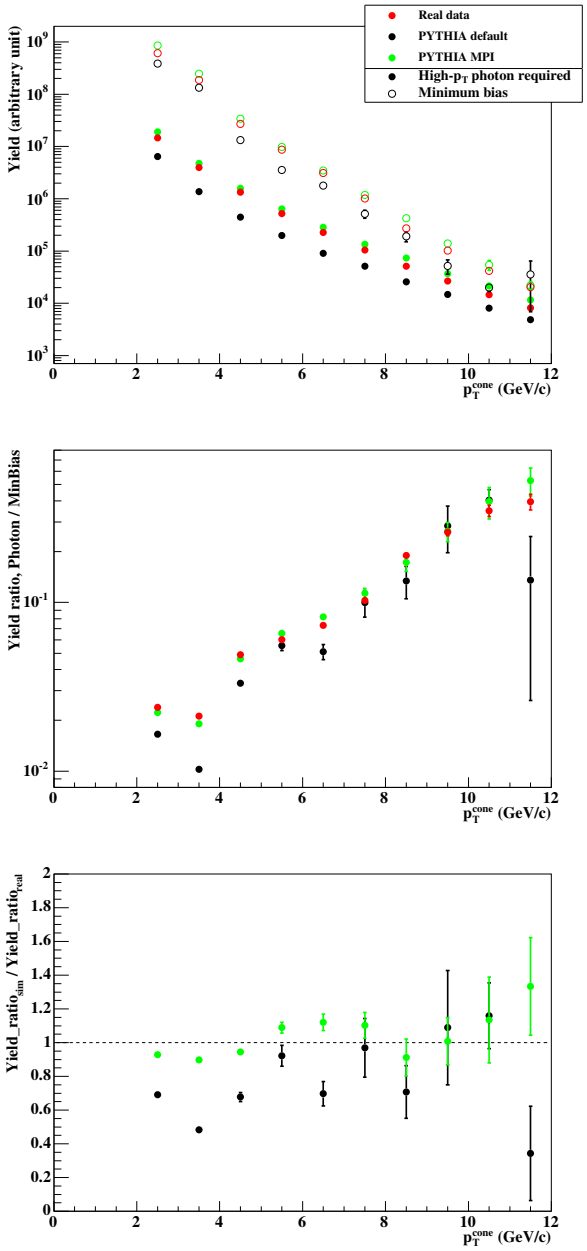

Figure 4.24: **Top**: p_T^{cone} distributions in the minimum data (**Open circle**) and the high-p_T photon data (**Close circle**) with the real data (**Red**), the PYTHIA default output (**Black**) and the PYTHIA MPI output (**Green**). **Middle**: The ratio of the photon-data yield to the MinBias-data yield in the top plot. **Bottom**: Difference of the yield ratio between the real data and the simulation outputs, namely the simulation yield ratio divided by the real-data yield ratio.

4.8 Double helicity asymmetry

4.8.1 Evaluation method

The A_{LL} is expressed with measured quantities as

$$A_{LL} = \frac{1}{|P_B||P_Y|}\frac{N_{++} - RN_{+-}}{N_{++} + RN_{+-}} \tag{4.25}$$

$$R \equiv \frac{L_{++}}{L_{+-}} \tag{4.26}$$

where N_{++} and N_{+-} are yields of measured objects, namely the particle clusters in this analysis, with colliding proton beams having the same ($++$ or $--$) and opposite ($+-$ or $-+$) helicity, respectively; P_B and P_Y are the beam polarizations; R is the relative luminosity. The methods of measuring each quantity are described below. The A_{LL} is measured fill-by-fill and the results are fitted to a constant, because the beam polarization and the relative luminosity are evaluated fill-by-fill to decrease systematic errors. Due to bad conditions on the beam polarization, three fills out of $\sim$100 fills have been discarded in the A_{LL} measurement. Finally the integrated luminosity used was 2.1 pb^{-1}.

With the cone method described in the previous section, the yields of particle clusters (N_{++} and N_{+-}) were measured in six $p_T^{\rm cone}$ bins, $4 \sim 5$, $5 \sim 6$, $6 \sim 7$, $7 \sim 8$, $8 \sim 10$ and $10 \sim 12$ GeV/c. The statistical error of the A_{LL} is written as

$$\begin{aligned}
\sigma_{A_{LL}} =& \sqrt{\left(\frac{\partial A_{LL}}{\partial N_{++}}\right)^2 \cdot \sigma^2_{N_{++}} + \left(\frac{\partial A_{LL}}{\partial N_{+-}}\right)^2 \cdot \sigma^2_{N_{+-}}} \\
=& \frac{1}{P_B P_Y}\frac{2R\sqrt{N^2_{+-}\sigma^2_{N_{++}} + N^2_{++}\sigma^2_{N_{+-}}}}{(N_{++} + RN_{+-})^2} \\
=& \frac{1}{P_B P_Y}\frac{2R\sqrt{N_{++}N_{+-}(N_{++} + N_{+-})}}{(N_{++} + RN_{+-})^2} \quad (\because \sigma_N \approx \sqrt{N})
\end{aligned} \tag{4.27}$$

When $R \simeq 1$ and $N_{++} \simeq N_{+-} \simeq N/2$ are assumed, it becomes

$$\sigma_{A_{LL}} \simeq \frac{1}{P_B P_Y}\frac{1}{\sqrt{N}} \tag{4.28}$$

The relative luminosity at PHENIX is defined with the BBCLL1 trigger counts (N^{++}_{BBC} and N^{+-}_{BBC}) as $R = N^{++}_{BBC}/N^{+-}_{BBC}$. The BBCLL1 trigger counts for each beam crossing were stored in the GL1P scaler and were summed up

Table 4.3: The subprocess fractions in events that fired the BBCLL1 trigger and the ZDCLL1 trigger. It has been estimated with a PYTHIA and GEANT simulation.

Subprocess	ID	BBCLL1	ZDCLL1
Elastic	91	0%	22%
Single diffraction (AB→XB)	92	1.7%	9.8%
Single diffraction (AB→AX)	93	1.6%	9.9%
Double diffraction	94	6.0%	19%
Low-p_T production	95	32%	21%
QCD $f_i g \to f_i g$	28	23%	6.9%
QCD $gg \to gg$	68	31%	10%

to obtain N_{BBC}^{++} and N_{BBC}^{+-} by taking into account the polarization direction of each beam crossing. According to a PYTHIA and GEANT simulation, the subprocess of events that fire the BBCLL1 trigger in proton-proton collisions at $\sqrt{s} = 200$ GeV is partly hard scatterings as shown in Tab. 4.3. A possible spin dependence, A_{LL}, of such hard scatterings causes an error on the relative luminosity. The error has been checked by comparing the relative luminosity with another relative luminosity defined with the ZDCLL1 trigger counts. The ZDCLL1 trigger is fired when both the north ZDC and the south ZDC have a hit and the reconstructed z-vertex is <30 cm. Table 4.3 shows the subprocess fractions also for the ZDCLL1 trigger, and the two triggers are mostly independent. The difference was zero within its error and thus this error size was used as the error of the relative luminosity on A_{LL}, which is 2.3×10^{-4}.

The beam polarizations were measured with the pC and H-jet polarimeters at 12 o'clock of the RHIC ring. The luminosity-weighted-average polarizations are

$$\langle P_B \rangle = 0.503 \pm 0.002(stat) \pm 0.025(systB) \pm 0.015(systG) \quad (4.29)$$

$$\langle P_Y \rangle = 0.485 \pm 0.002(stat) \pm 0.025(systY) \pm 0.015(systG) \quad (4.30)$$

where "systB" and "systY" are systematic uncertainties from the CNI polarimeter in the blue and yellow beams, respectively, and "systG" is a global systematic uncertainty due to the calibration with the H-jet polarimeter. The error on $\langle P_B \rangle \langle P_Y \rangle$ is 9.4%.

Figure 4.25 and 4.26 show the polarizations and the relative luminosity vs fill number. Figure 4.27 shows A_{LL} vs fill and the result of fittings in each $p_T^{\rm cone}$ bin. The χ^2 value in the fittings are normal.

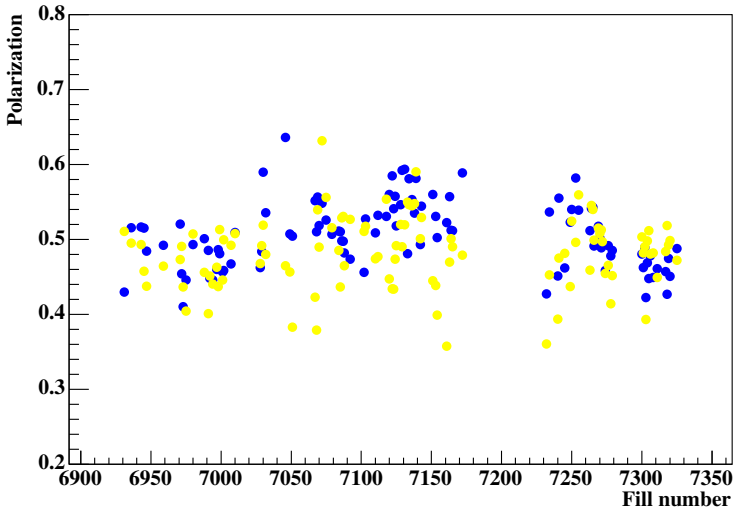

Figure 4.25: Polarizations of yellow and blue beams vs fill number.

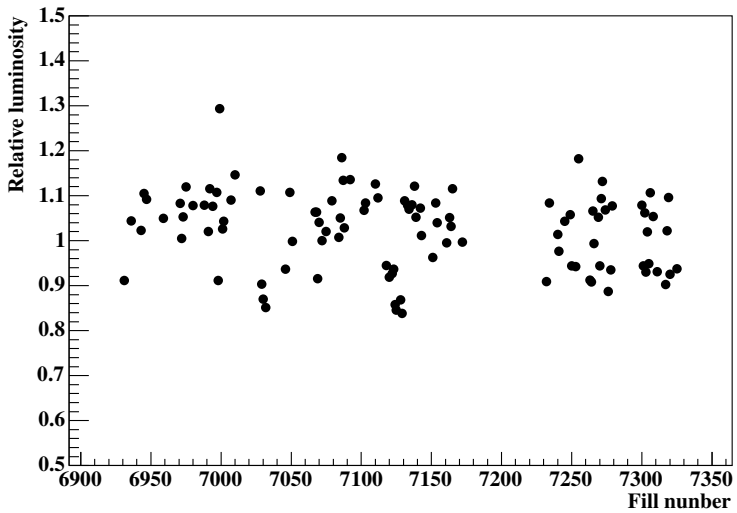

Figure 4.26: Relative luminosity vs fill number.

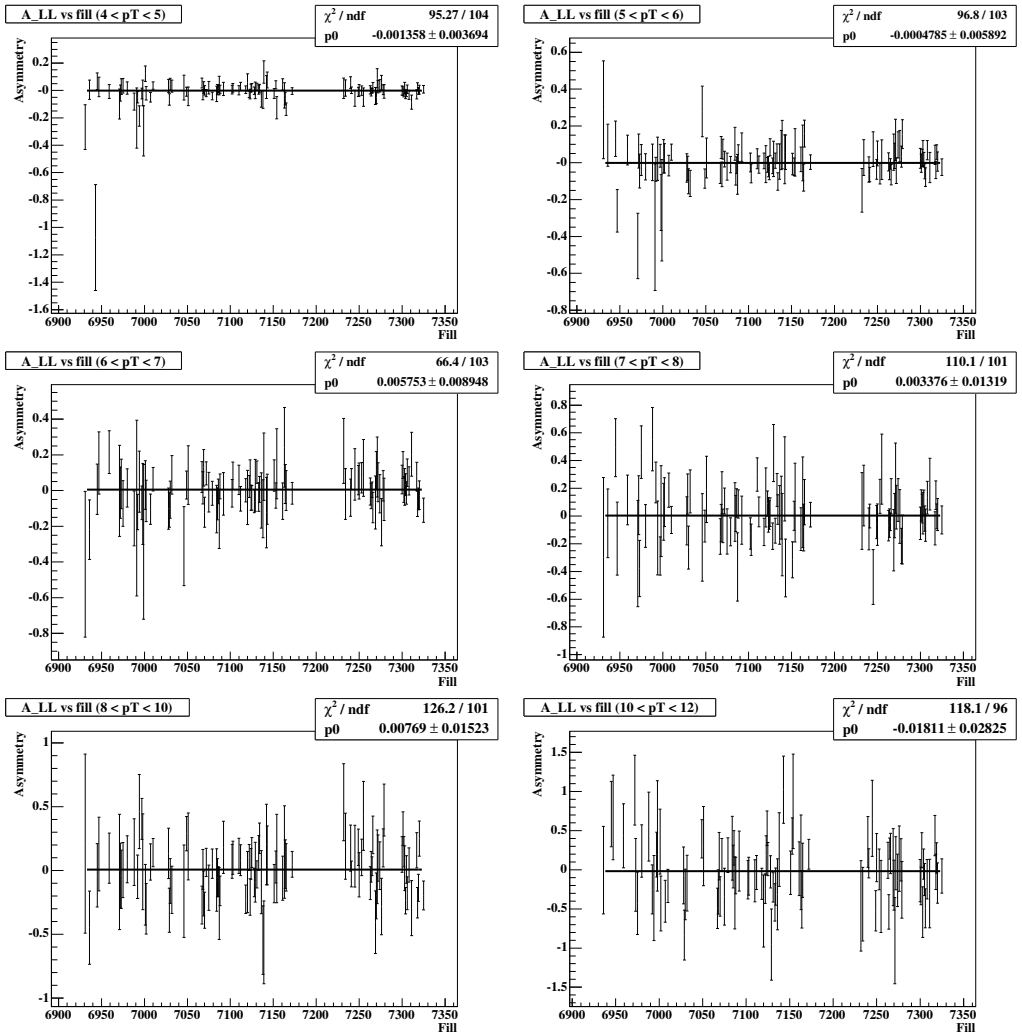

Figure 4.27: Asymmetry in every fill in each p_T^{cone} bin.

4.8.2 Check on systematic errors

Bunch shuffling method

Any fill- or bunch-dependent systematic errors can be checked with a bunch shuffling method. The spin polarization directions of every bunch in every fill are randomly assigned while the balance between the number of bunches with correctly and oppositely assigned helicities are kept. The A_{LL}s with such a random polarization direction should be zero and fluctuate by the statistical uncertainty. A mass of random data (10000 sets in this analysis) are generated, and it is checked whether the width of A_{LL} distribution in the random data correctly matches the A_{LL} statistical error estimated with Eq. 4.27.

Figure 4.28 shows A_{LL} distributions from bunch shuffling in each $p_T^{\rm cone}$ bin. Figure 4.29 shows χ^2/NDF distributions from bunch shuffling in each $p_T^{\rm cone}$ bin. This study shows that the statistical error on A_{LL} are correctly estimated and no additional systematic errors exist.

Single helicity asymmetry

Single helicity asymmetry, A_L, is defined as

$$A_L \equiv \frac{\sigma_+ - \sigma_-}{\sigma_+ + \sigma_-} = \frac{1}{P}\frac{N_+ - R\ N_-}{N_+ + R\ N_-} \quad , \quad R \equiv \frac{L_+}{L_-} \tag{4.31}$$

where the subscripts + and − denote the polarization direction of either the blue beam or the yellow beam. It must be zero under the parity symmetry. Thus any non-zero value indicates systematic errors.

4.8.3 Calculation of predicted asymmetry

Polarized/unpolarized cross sections of jet production for every subprocess (qq, qg and gg) was calculated at NLO based on the SCA. The polarized cross sections were calculated using various $\Delta g(x)$ in order to compare the measured A_{LL} with various predicted A_{LL}s to search for a $\Delta g(x)$ most agreeable to the measured A_{LL}. The various $\Delta g(x)$ are drawn in Fig. 4.30 and

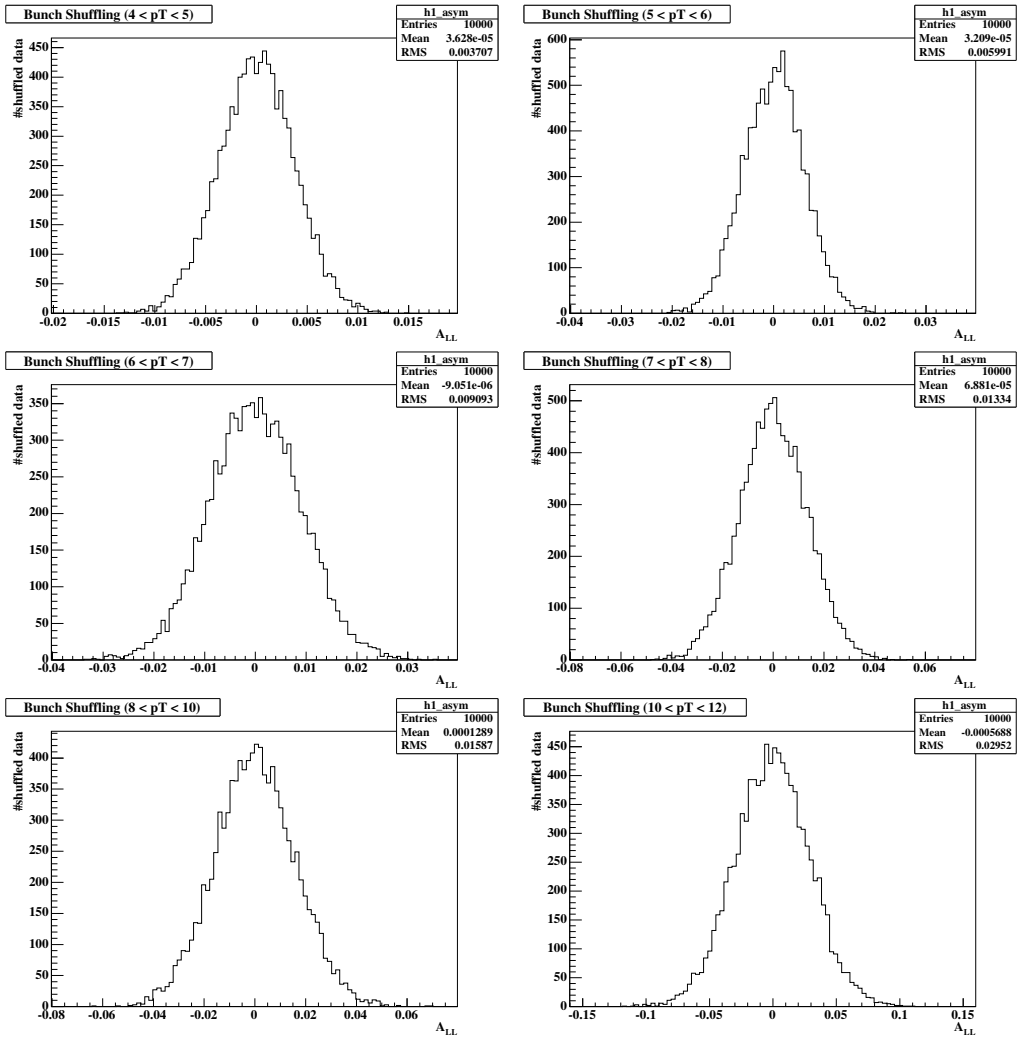

Figure 4.28: A_{LL} distributions from bunch shuffling in each p_T^{cone} bin.

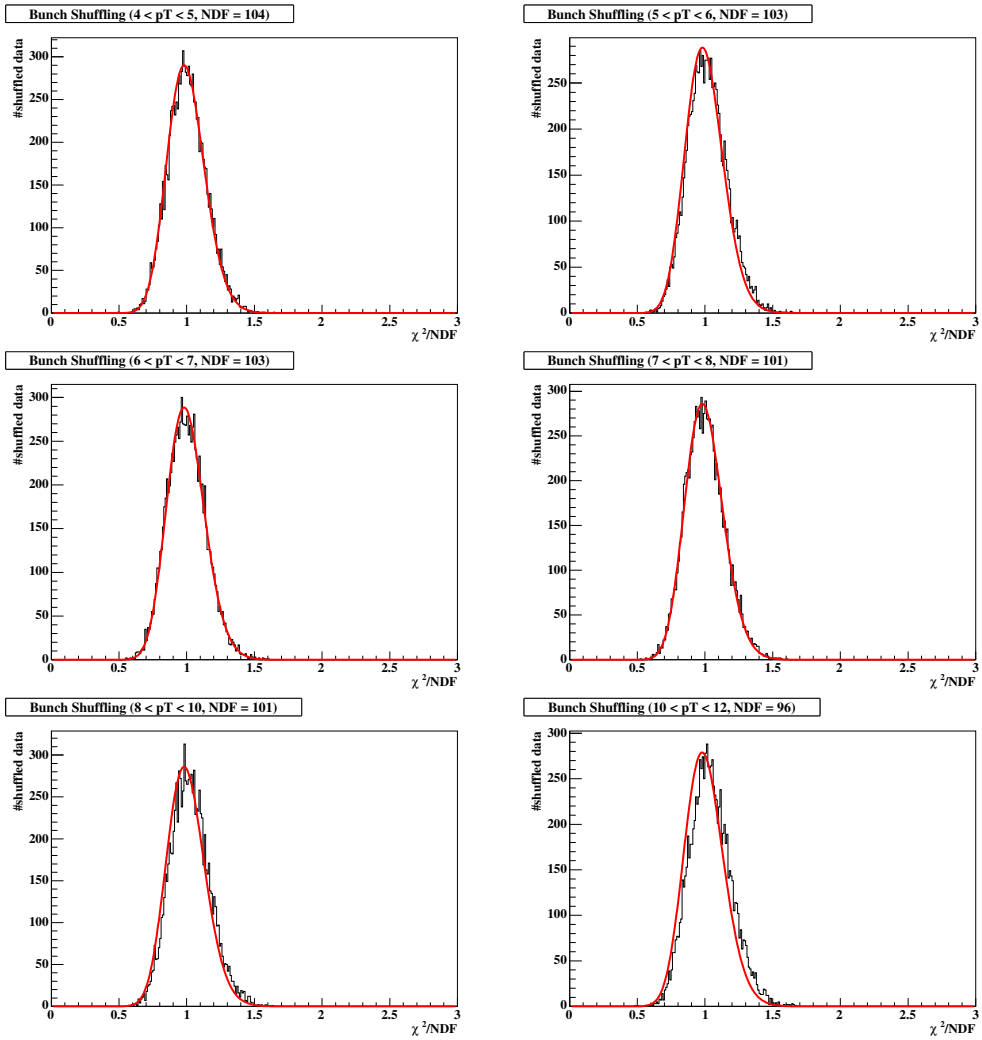

Figure 4.29: χ^2/NDF distributions from bunch shuffling in each p_T^{cone} bin. The red lines are calculated statistical distributions.

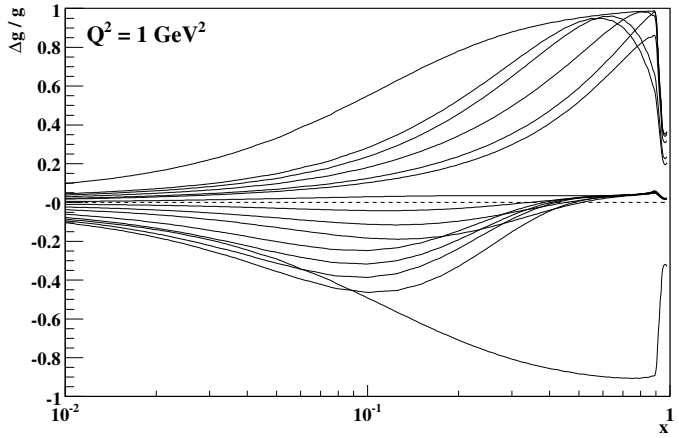

Figure 4.30: Assumed gluon distribution functions $\Delta g^{GRSV}(x)$ used in A_{LL} calculation. The topmost and bottommost curves correspond to the Δg integral of 1.24 and -1.24 at $Q^2 = 0.4$ GeV^2, respectively. For detailed explanations, see the text.

the integrated values are

$$\int_0^1 dx \Delta g(x, Q^2 = 0.4 \text{ GeV}^2) = \begin{cases} -1.24\ (\Delta g = -g), \\ -1.05, \\ -0.90, \\ -0.75, \\ -0.60, \\ -0.45, \\ -0.30, \\ -0.15, \end{cases} \quad \begin{cases} 0\ (\Delta g = 0), \\ 0.24\ (\text{GRSV-std}), \\ 0.30, \\ 0.45, \\ 0.60, \\ 0.70, \\ 1.24\ (\Delta g = g) \end{cases} \tag{4.32}$$

Each $\Delta g(x)$ (except the GRSV-std, the $\Delta g = g$ input, the $\Delta g = 0$ input and the $\Delta g = -g$ input) have been newly obtained with a global fit to the DIS data used in the original GRSV analysis[44]. In a global fit, the integral value of $\Delta g(x)$ was fixed to its peculiar value listed above, and the shape of $\Delta g(x)$ and the quark-related parameters were made free. The χ^2 in the global fits are almost constant over all the various $\Delta g(x)$, and this means that the variation of $\Delta g(x)$ is insensitive to the DIS data.

The various $\Delta g(x)$ above were evolved up to a Q^2 of every events in A_{LL} calculation. A_{LL} of every subprocess (A_{LL}^{qq}, A_{LL}^{qg} and A_{LL}^{gg}) can be derived

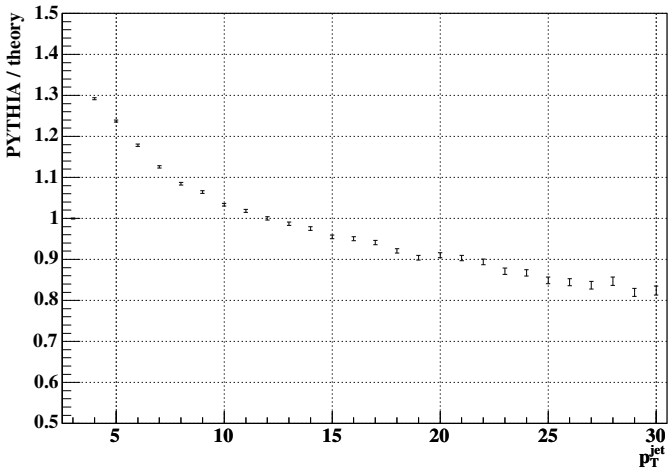

Figure 4.31: The ratio of the unbiased jet yield in the PYTHIA simulation to that in the theory calculation. The vertical axis is in arbitrary unit.

as functions of $p_T^{\rm jet}$ from the unpolarized and polarized cross sections. The PYTHIA+GEANT simulation produces the relative yields of every subprocess ($n^{qq}(p_T^{\rm jet})$, $n^{qg}(p_T^{\rm jet})$ and $n^{gg}(p_T^{\rm jet})$) in $p_T^{\rm cone}$ bins where $A_{LL}^{\rm cone}$ is measured. The relative yields take into account the convolution from jets to cones. $A_{LL}^{\rm cone}$ is calculated as a mean of A_{LL}^{qq}, A_{LL}^{qg} and A_{LL}^{gg} weighted by the relative yields;

$$A_{LL}^{\rm cone} = \frac{\int dp_T^{\rm jet} \sum_{isub=qq,qg,gg} n^{isub}(p_T^{\rm jet}) \cdot A_{LL}^{isub}(p_T^{\rm jet})}{\int dp_T^{\rm jet} \sum_{isub=qq,qg,gg} n^{isub}(p_T^{\rm jet})} \tag{4.33}$$

As an estimation on systematic errors, the slope of jet yields and the fraction of subprocesses were compared between the theory calculation and the PYTHIA simulation. Both the slope and the fraction were raw in the PYTHIA simulation, namely not biased by the high-p_T photon and the small cone, since the theory calculation cannot be biased. Figure 4.31 shows the ratio of the unbiased jet yield in the PYTHIA simulation to that in the theory calculation. The non-flat distribution indicates a discrepancy in jet yield slope. The sudden decrease at the lowest $p_T^{\rm jet}$ bin is caused by the cross section regularization at low p_T in PYTHIA. To check the variation of $A_{LL}^{\rm cone}$ caused by the slope difference, the relative yields of each subprocess were

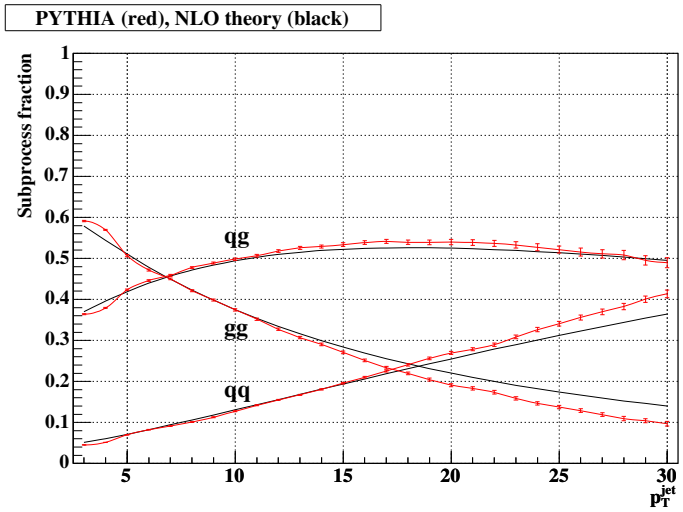

Figure 4.32: The fractions of subprocesses (qq, qg and gg) as a function of $p_T^{\rm jet}$. This is an unbiased fraction, i.e. no cone and no trigger photon are required in the PYTHIA simulation as well as the theory calculation.

modified as

$$n^{isub}(p_T^{\rm jet}) \rightarrow n^{isub}(p_T^{\rm jet})/R(p_T^{\rm jet}) \tag{4.34}$$

where $R(p_T^{\rm jet})$ is the ratio shown in Fig. 4.31. Figure 4.32 shows the fractions of subprocesses in the theory calculation and the PYTHIA simulation. The fraction of the qq subprocess in the PYTHIA simulation is a little larger at higher $p_T^{\rm jet}$. To check the variation of $A_{LL}^{\rm cone}$ caused by the fraction difference, the relative yields of each subprocess were modified as

$$n^{isub}(p_T^{\rm jet}) \rightarrow n^{isub}(p_T^{\rm jet}) \cdot r_{th}^{isub}(p_T^{\rm jet})/r_{PY}^{isub}(p_T^{\rm jet}) \tag{4.35}$$

where $r_{th}^{isub}(p_T^{\rm jet})$ and $r_{PY}^{isub}(p_T^{\rm jet})$ are the fraction of a subprocess $isub$ in the theory calculation and the PYTHIA simulation, respectively, which are shown in Fig. 4.32.

Figure 4.33 shows the relative yields of $qq/qg/gg$ subprocesses in the PYTHIA MPI+GEANT simulation, and Fig. 4.34 shows $A_{LL}^{\rm jet}$ derived from the polarized/unpolarized cross sections. Figure 4.35 shows $A_{LL}^{\rm cone}$ evaluated with the $A_{LL}^{\rm jet}$ and the relative yields of $qq/qg/gg$ subprocesses. The $A_{LL}^{\rm cone}$s estimated bin-by-bin were fitted to a 3rd-polynomial function to obtain a smooth $A_{LL}^{\rm cone}$ curve. The statistical errors (vertical bars in the figure), the yield slope difference (dash lines) and the subprocess-fraction difference (dotted line) are negligible when compared with other systematic errors.

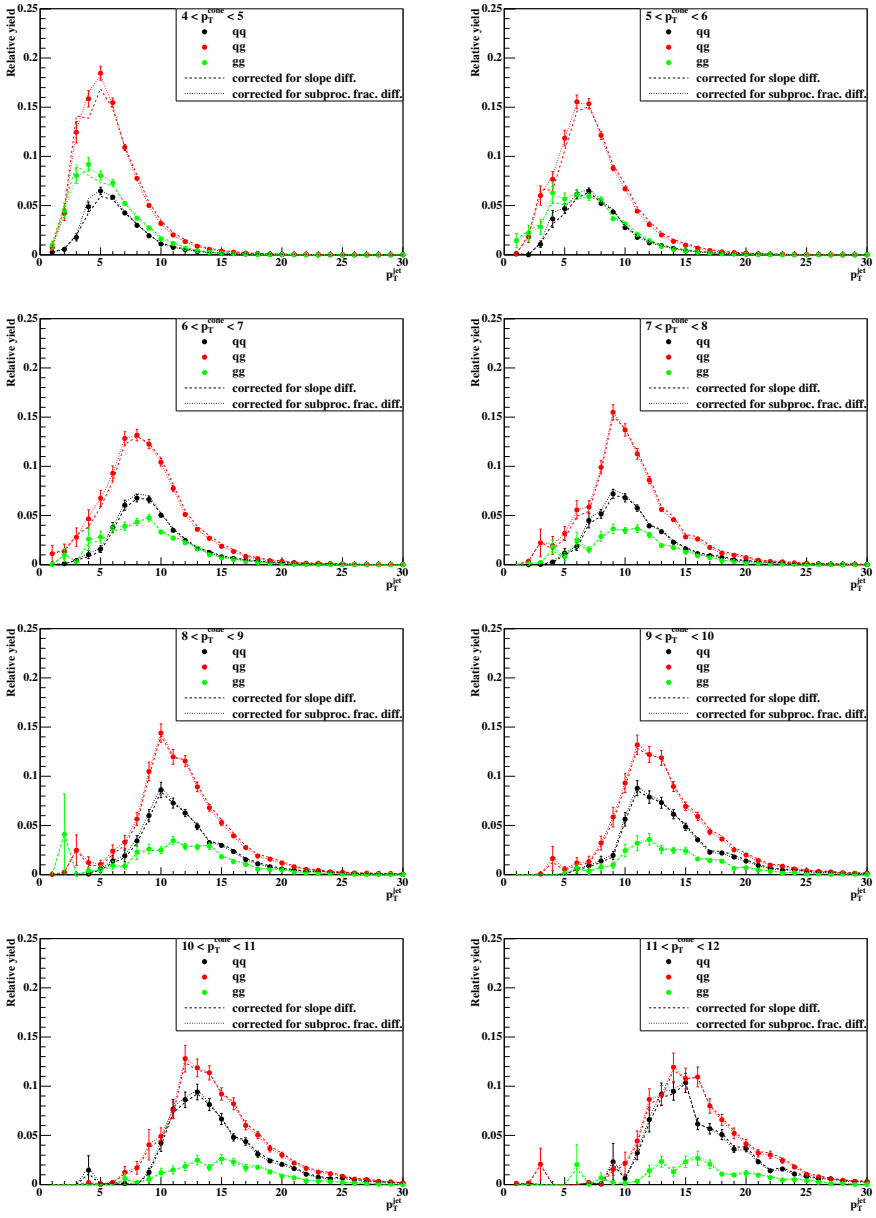

Figure 4.33: The relative yields of qq, qg and gg subprocesses in the PYTHIA+GEANT simulation. The yields corrected for the slope-of-yield difference and the subprocess fraction difference are also shown.

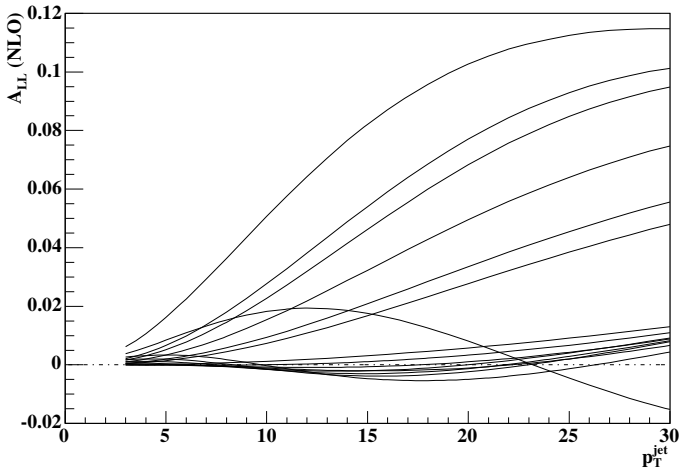

Figure 4.34: $A_{LL}^{\rm jet}$ evaluated as a function of $p_T^{\rm jet}$ with various Δg^{GRSV} values. All the Δg^{GRSV} values are shown in the text.

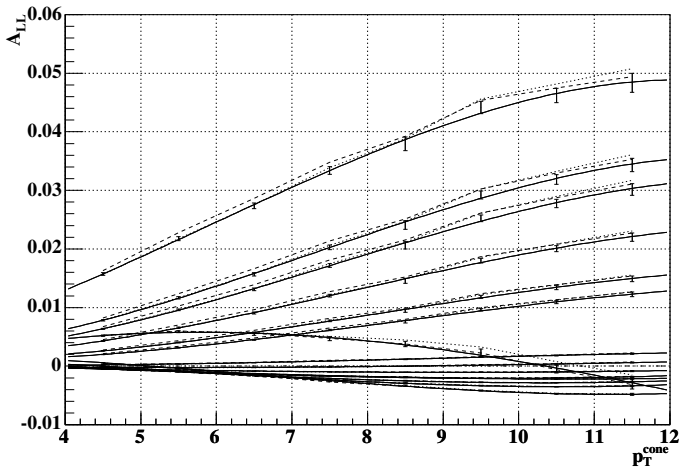

Figure 4.35: $A_{LL}^{\rm cone}$ as a function of $p_T^{\rm cone}$ evaluated with the jet A_{LL} and the relative yields of qq/qg/gg subprocesses. **Vertical bars**: $A_{LL}^{\rm cone}$ values evaluated at every $p_T^{\rm cone}$ bin with errors due to the statistical errors of the relative yields. **Solid lines**: 3rd-polynomial functions fitted to the $A_{LL}^{\rm cone}$ values. **Dash lines**: $A_{LL}^{\rm cone}$ values evaluated at every $p_T^{\rm cone}$ bin using the relative yields corrected for the yield slope difference. **Dotted lines**: $A_{LL}^{\rm cone}$ values evaluated at every $p_T^{\rm cone}$ bin using the relative yields corrected for the subprocess fraction difference.

4.9 Statistical overlap with π^0 measurement

The PHENIX experiment also measured π^0 A_{LL} with the identical data set[6]. Since π^0 comes from jet via fragmentation process, the statistical overlap between the cone measurement and the π^0 measurement has been studied. For events in which a high-$p_T^{\rm cone}$ particle cluster was found, photon pairs that passed the experimental cuts used in the π^0 measurement were judged as π^0 or not. When an event included several π^0s, a highest $p_T^{\pi 0}$ in the event was chosen. Two methods of identifying π^0 were used to check the systematic error of the methods.

One method (named "M1") used only measurable quantities and thus was applied to both the real data and the simulation. In principle π^0 can be identified not individually but statistically due to the combinatorial background, but in this estimation each photon pair was regarded as π^0 by the probability that was set to the fraction of signals under the mass peak, $\mathcal{P} = S/(S+B)$ at $112 < m_{\gamma\gamma} < 162$ MeV. This assumption is valid when π^0s in one event are not correlated. The $\mathcal{P}$ has been evaluated at each ($p_T^{\rm cone}$, $p_T^{\pi 0}$) bin. Because the statistics of the simulation was not enough particularly at low $p_T^{\pi 0}$ and the $S/(S+B)$ in the simulation agreed with that of the real data over the measured ($p_T^{\rm cone}$, $p_T^{\pi 0}$) range, the $\mathcal{P}$ evaluated with the real data was also used for the simulation output.

The other method (named "M2") used the simulation information on the origin of particles in order to judge whether each photon pair was π^0 or not. The comparison with the first method can check the validity of the assumption on $\mathcal{P}$ in the first method.

Figure 4.36 shows results with the two methods. The real data M1 result agrees with the simulation M1 result in general. The points at $4 < p_T^{\rm cone} < 5$ GeV/c and $4 < p_T^{\pi 0} < 5$ GeV/c shows $\sim$40% difference, and it may be caused by the difference in π^0 reconstruction efficiency between the real data and the simulation. The simulation M1 and M2 results are consistent within $\sim$20% at most, and thus the accuracy of the M1 is at this level. In every $p_T^{\rm cone}$ bin, the event fractions are distributed widely over $p_T^{\pi 0}$ bins. Therefore no outstanding correlation between a $p_T^{\rm cone}$ bin and a $p_T^{\pi 0}$ bin has been observed.

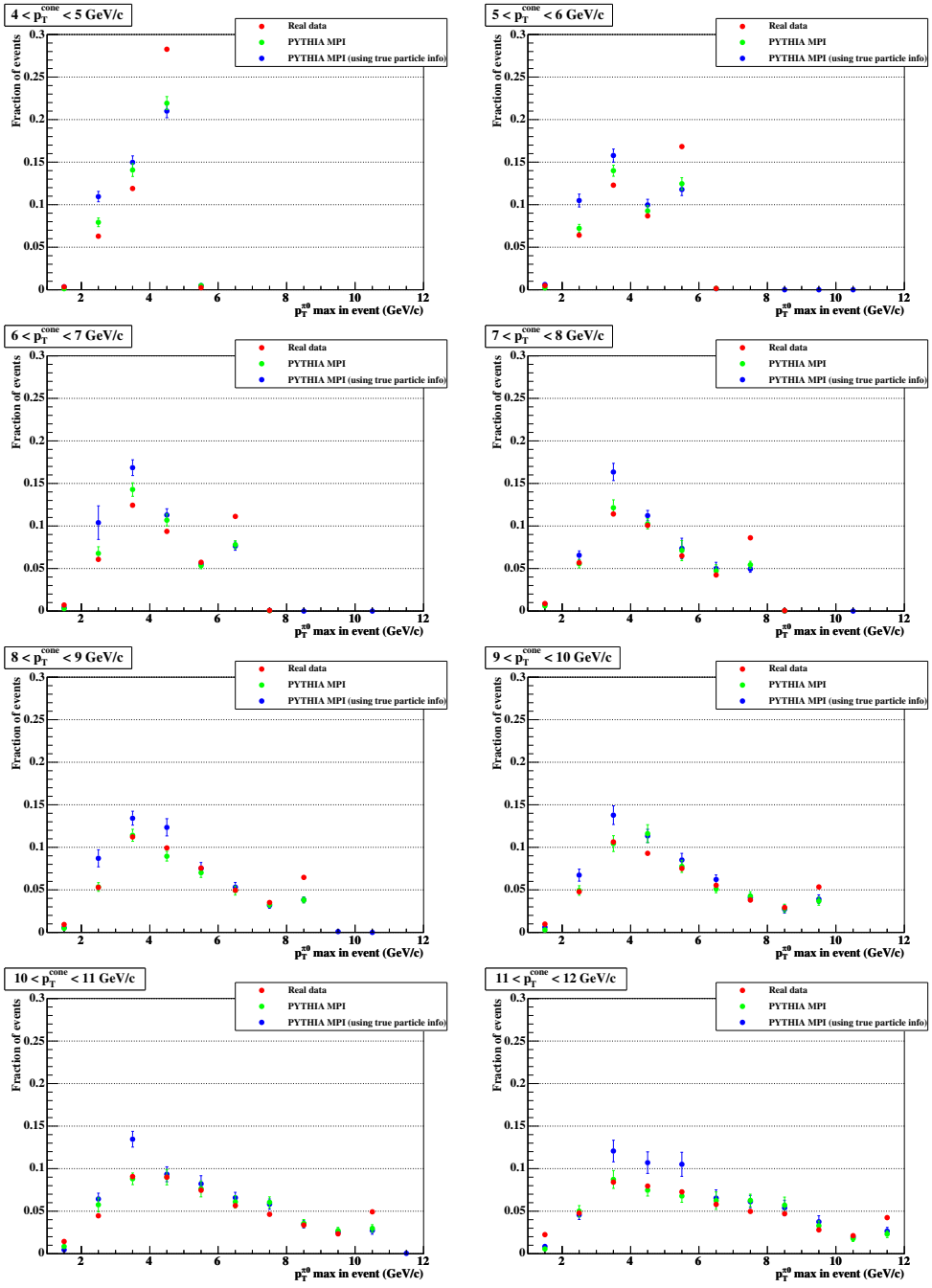

Figure 4.36: The fraction of events that include π^0 in each p_T^{cone} bin. The horizontal axis is the π^0 p_T maximum in each event. The vertical bar on every point shows statistical error.

Chapter 5

Results and discussions

5.1 Event structure

5.1.1 Multiplicity

Figure 5.1 shows the mean value of multiplicity in the Central Arm vs $p_T^{\rm sum}$ and in the cone vs $p_T^{\rm cone}$. The multiplicities in arm and cone of the simulation outputs agree, on the whole, with that of the real data. The PYTHIA MPI output is larger than the PYTHIA default output as expected, and the real data is closer to the PYTHIA default output. On the other hand, the $p_T^{\rm cone}$ distributions (Fig. 4.16) shows better agreement between the real data and the PYTHIA MPI output. It means that the PYTHIA MPI reproduces the sum of p_T of particles well, which is less sensitive to particle fragmentation process, while it doesn't reproduce the particle multiplicity very well. The reproducibility of the p_T sum is checked in the measurement of the transverse momentum density and the PHENIX thrust.

5.1.2 Transverse momentum density

Figures 5.2 and 5.3 show the $\mathcal{D}_{p_T}$ distributions for each $p_T^{\rm sum}$ range. In the "toward" region, the simulation outputs agree well with the real data. It shows that the shape of jets produced by the simulation is consistent with the real data. In the "transverse" region, the PYTHIA default output is generally smaller than the real data. It shows that the PYTHIA default does not contain sufficient underlying events. The PYTHIA MPI output agrees with the real data well.

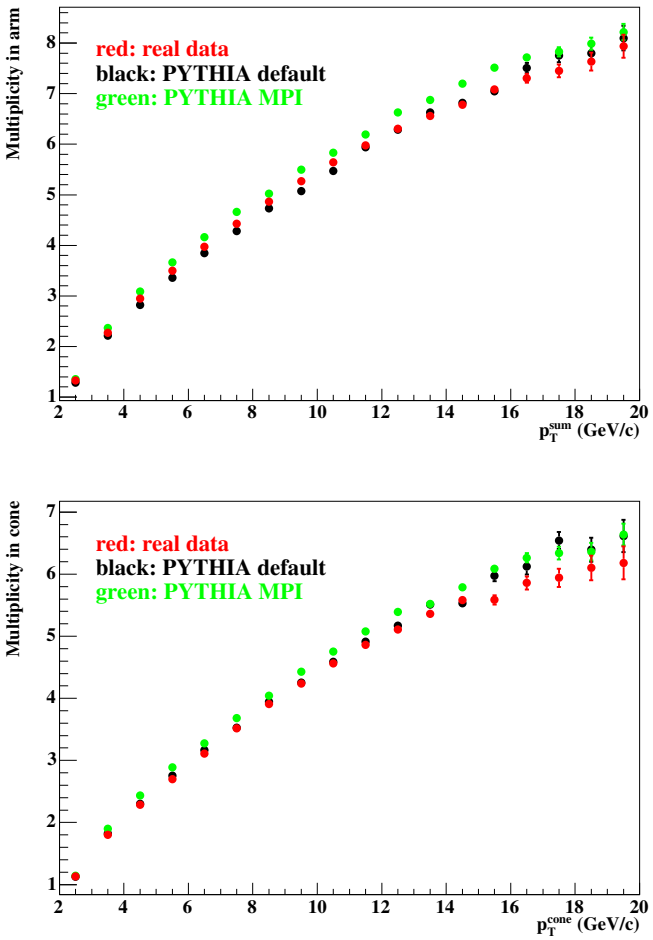

Figure 5.1: Mean multiplicity in the Central Arm vs $p_T^{\rm sum}$ (**Top**) and mean multiplicity in the cone vs $p_T^{\rm cone}$ (**Bottom**).

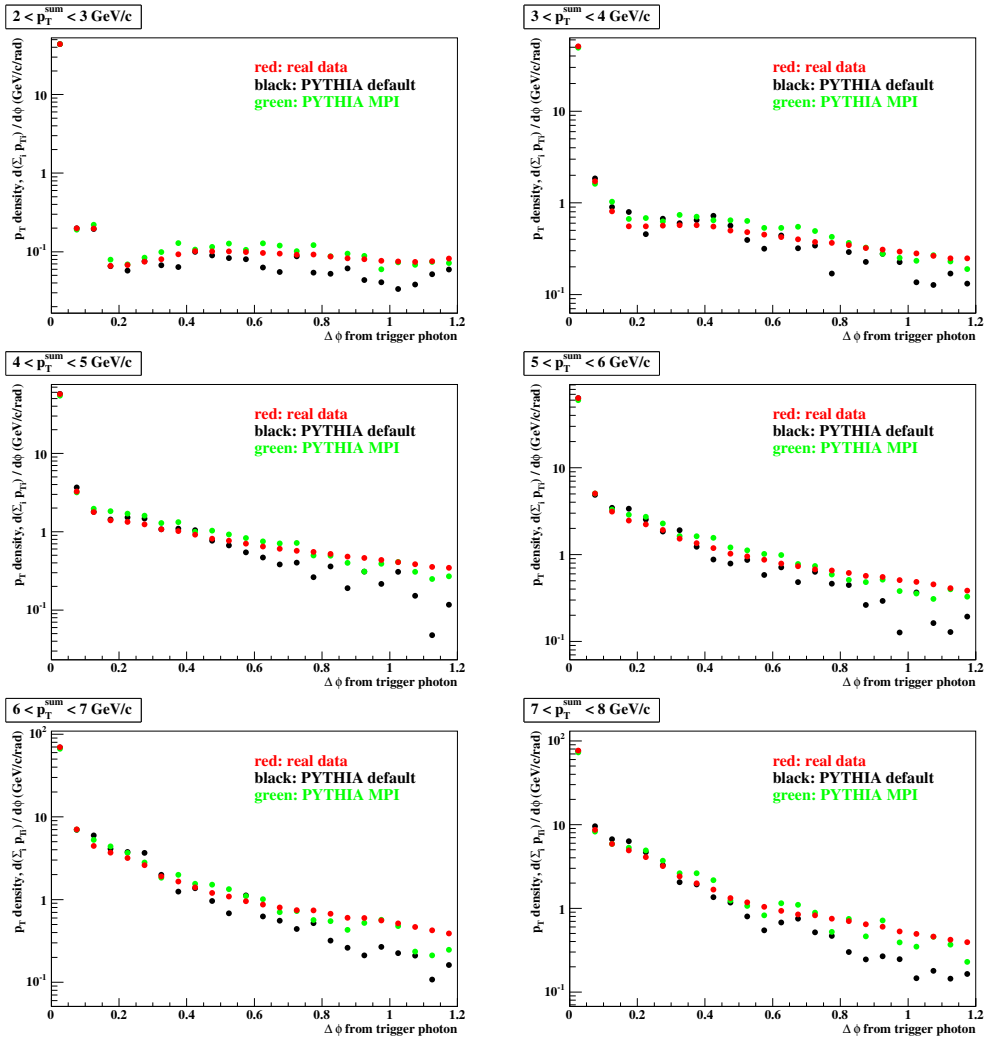

Figure 5.2: p_T density, $\mathcal{D}_{P_T} = d\Sigma_i p_{Ti}/d\phi$ (GeV/c/rad), in each $p_T^{\rm sum}$ bin.

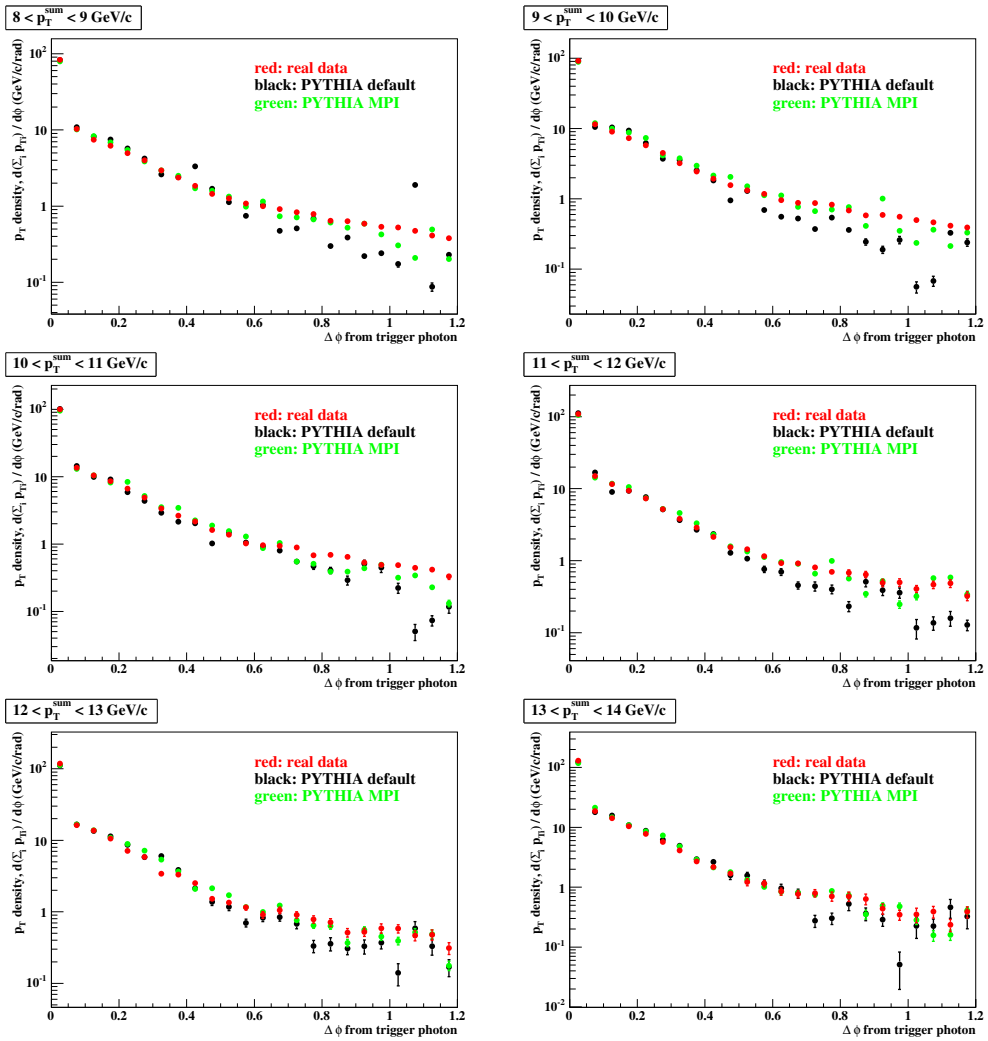

Figure 5.3: p_T density, $\mathcal{D}_{P_T} = d\Sigma_i p_{Ti}/d\phi$ (GeV/c/rad), in each $p_T^{\rm sum}$ bin (continued).

5.1.3 Thrust distribution in PHENIX Central Arm

Figures 5.4 and 5.5 show the thrust distribution in each $p_T^{\rm sum}$ range. The PYTHIA MPI output agrees with the real data well. The PYTHIA default has a steeper slope. It means the number of particles at the vicinity of jets is insufficient. In all the real data, the PYTHIA default output and the PYTHIA MPI output, the thrust distribution becomes sharper as $p_T^{\rm sum}$ increases. It is due to the jet characteristic that its transverse momentum (j_T) is independent of its longitudinal momentum ($p_T^{\rm jet}$) and is almost constant.

If the real data include a contribution from non-jet (isotropic) events, the T_{PH} distribution of the real data is a mixture of the distribution of the simulation output and the distribution of the isotropic case. The contribution from non-jet events is negligible based on the PYTHIA MPI output.

5.2 Cone production rate

Figure 5.6 shows the cone production rate. The sources of the systematic errors are listed in Tab. 5.1. The main sources on the measurement are the BBC cross section and the EMCal energy scale. Each error is fully correlated bin-to-bin. The error on the EMCal energy scale includes the change of p_T of individual photons and the change of the threshold of the high-p_T photon requirement. The main sources of errors on the calculation are the relation between jet and cone and the EMCal energy scale. The errors on the EMCal energy scale in the measurement and in the calculation are fully correlated and cancel out in the comparison between them. The largest uncertainty in comparing the measurement and the calculation is the 10% p_T scale uncertainty caused by the definition of jet. The calculation with the PYTHIA MPI agrees with the measurement within their errors over the measured range $4 < p_T^{\rm cone} < 15$ GeV/c.

The result with the PYTHIA default are smaller than the result with the PYTHIA MPI by 50% at $p_T^{\rm cone} = 4$ GeV/c, by 35% at $p_T^{\rm cone} = 9$ GeV/c and by 20% at $p_T^{\rm cone} = 14$ GeV/c. It can be fully explained with the difference appeared in Fig. 4.23 between the PYTHIA default and the PYTHIA MPI. According to the comparisons of the event structures, the PYTHIA MPI reproduces the space distribution of particle momenta in one event much better than the PYTHIA default. Therefore, for the cone production rate evaluated with the PYTHIA MPI simulation, the error due to possible insufficient tunings of the PYTHIA MPI should be smaller than the difference of the cone production rate between the PYTHIA MPI simulation and the PYTHIA default simulation.

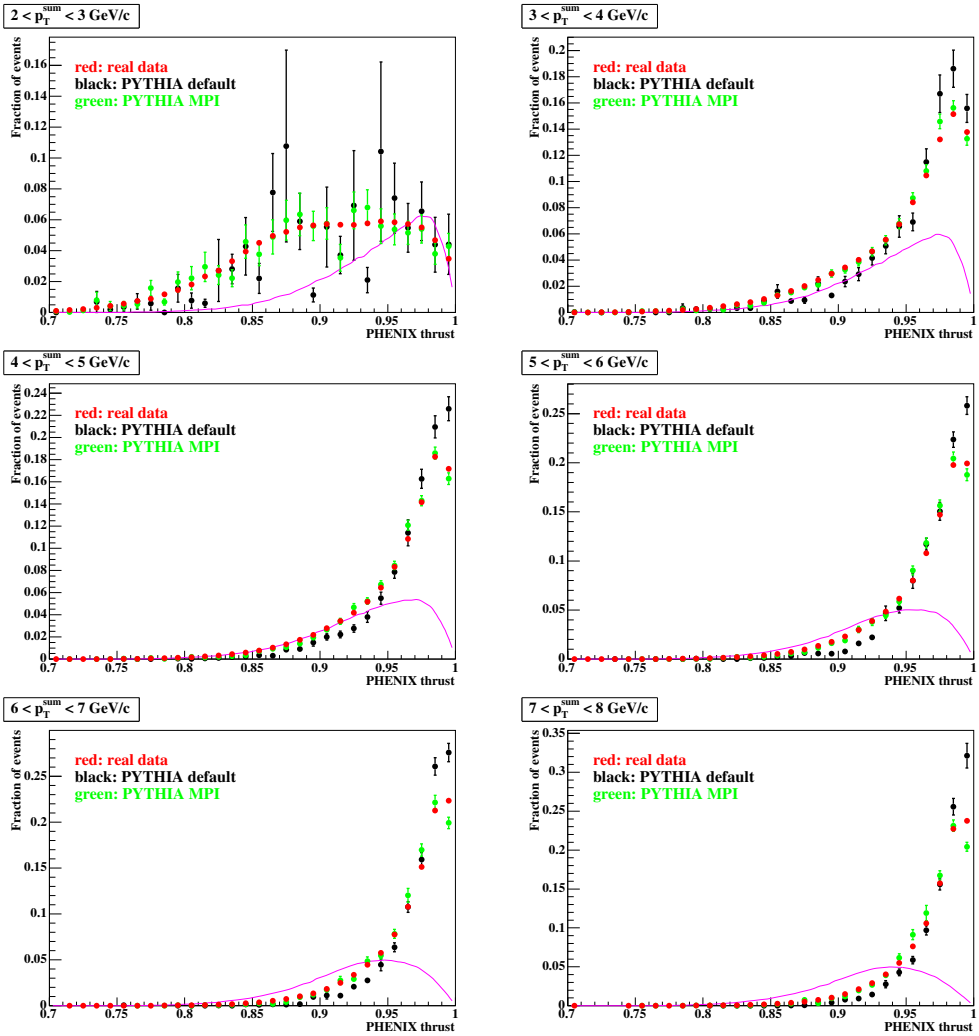

Figure 5.4: PHENIX thrust distribution in each $p_T^{\rm sum}$ bin. All distributions have been normalized so that their areas were equal to one another. The purple lines are the distributions of isotropic events in the acceptance of the PHENIX Central Arms, which are evaluated with Eq. 4.19.

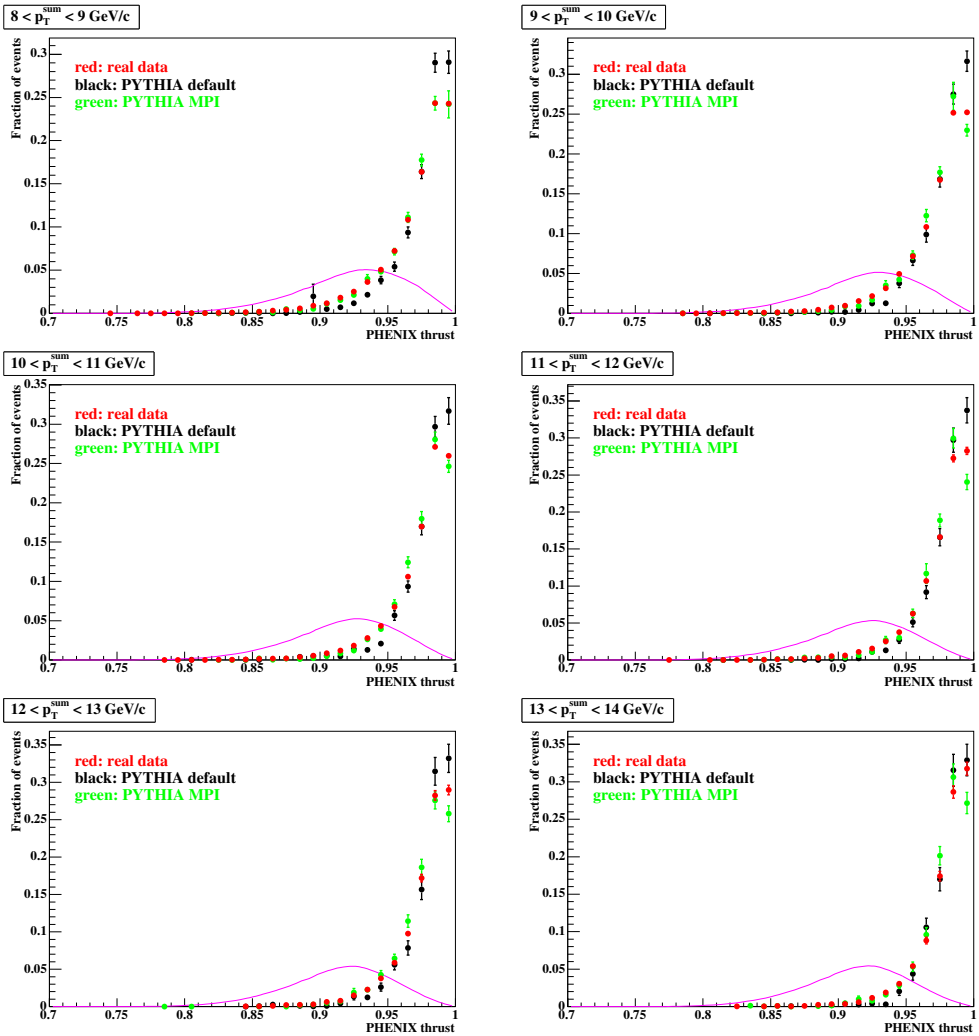

Figure 5.5: PHENIX thrust distribution in each p_T^{sum} bin (continued).

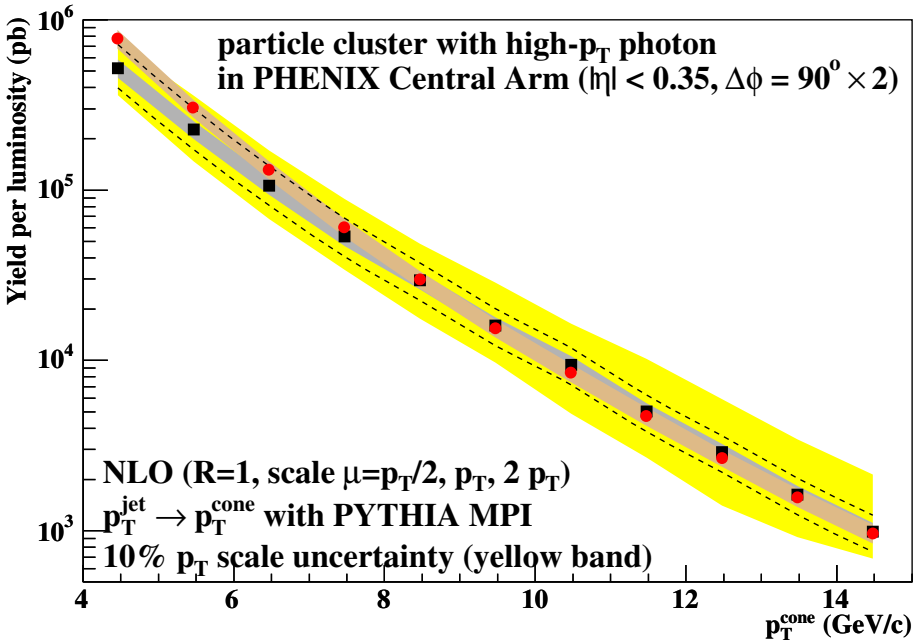

Figure 5.6: Cone production rate. **Red point**: Real data with systematic errors drawn as **pale red band**. **Black point**: Calculation with the PYTHIA MPI with systematic errors drawn as **gray band**. **Black dash line**: Calculation with a theory factorization scale of $p_T/2$ or $2p_T$. **Yellow band**: Variation caused by 10% p_T scale uncertainty.

Table 5.1: The sources of the systematic errors on cone event rate.

source	its error	error on event rate
Measurement		
BBC cross section	9.7%	9.7%
EMCal energy scale	1.5%	7∼6%
Tracking momentum scale	1.5%	0∼3%
Trig. eff. (ERTLL1_4x4c)	2.6%	2.6%
Trig. eff. (BBCLL1)	<1%	small
Calculation		
Jet-to-cone relation	-	10%
EMCal energy scale	1.5%	7∼6%
Tracking momentum scale	1.5%	0∼3%
Simulation stat. error	-	2∼5%
10% p_T scale uncertainty between measurement and calculation		

Table 5.2: Measured particle cluster A_{LL}.

$p_T^{\rm cone}$ range and mean (GeV/c)	A_{LL}	stat. error
4∼5, 4.42	-0.0014	0.0037
5∼6, 5.43	-0.0005	0.0059
6∼7, 6.43	0.0058	0.0089
7∼8, 7.44	0.0034	0.0132
8∼10, 8.79	0.0077	0.0152
10∼12, 10.81	-0.0181	0.0282

5.3 Single helicity asymmetry A_L

Figure 5.7 shows measured A_L. A_L has been measured for the blue beam polarization while the yellow beam was assumed to be unpolarized and vice versa. Measured A_Ls for the blue and yellow beam polarizations were averaged. No significant asymmetry was observed.

5.4 Double helicity asymmetry A_{LL}

Figure 5.8 shows measured $A_{LL}^{\rm cone}$ and four prediction curves. Table 5.2 shows the values of measured $A_{LL}^{\rm cone}$. The systematic error of the relative luminosity is much smaller than the statistical error and is negligible. On the prediction curves the systematic errors related to the relative yields of subprocesses are

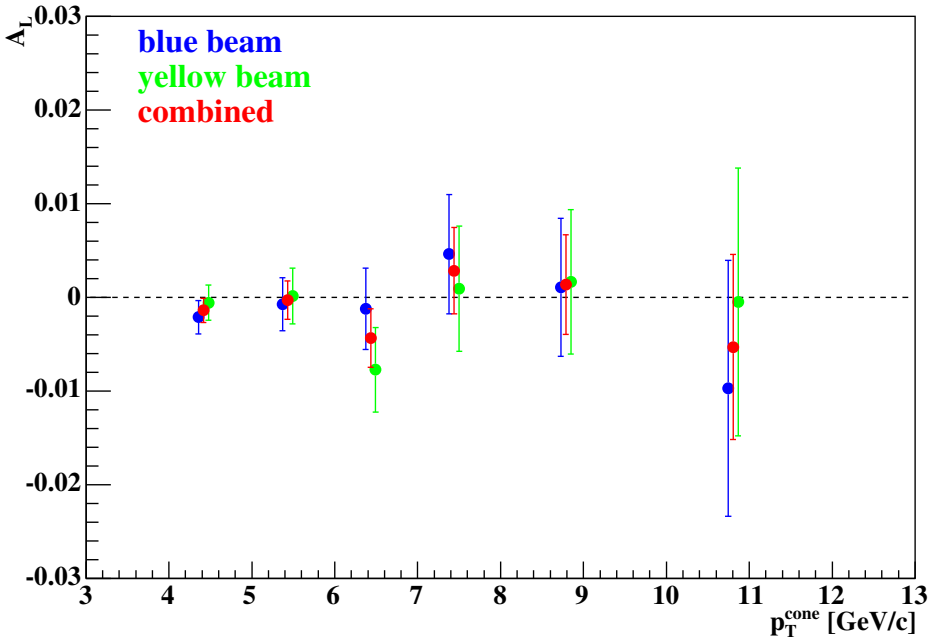

Figure 5.7: Particle cluster A_L as a function of p_T^{cone}. The blue, yellow, and red points correspond to the result with blue beam polarization, the result with yellow beam polarization, and the combined result.

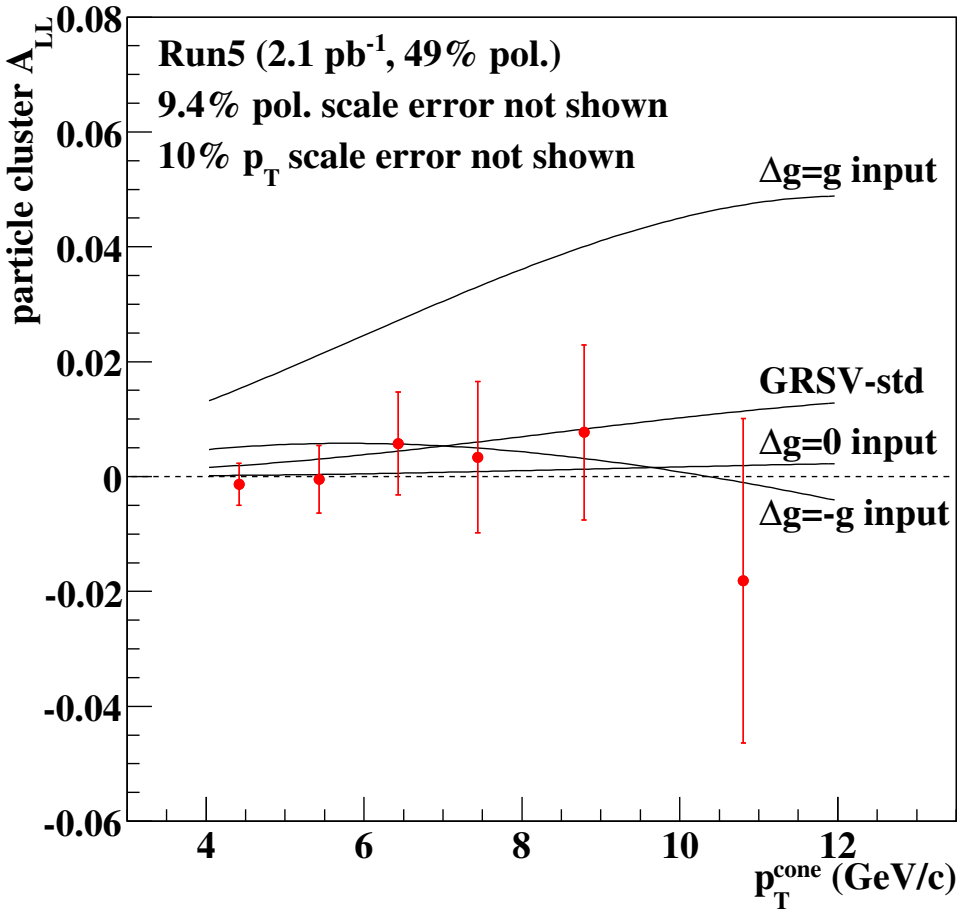

Figure 5.8: Particle cluster A_{LL} as a function of $p_T^{\rm cone}$. **Red point**: Measurement result with statistical error bars. **Black lines**: Calculation results based on four $\Delta g(x)$ functions and the PYTHIA MPI + GEANT simulation.

smaller than the 10% p_T scale uncertainty by roughly a order of magnitude. Therefore it is not included in this plot.

The statistical fluctuation of the data points seems smaller than the size of the statistical errors. One possible cause for this is an overestimate of the statistical errors, but the bunch shuffling analysis proved the statistical errors assigned to be correct. Another possible cause is an statistical correlation between the data points, but we could not find any origin of such correlation. Therefore we concluded that the small fluctuation of the data points happened statistically despite its small probability.

5.5 Constraint on Δg

5.5.1 Probed x_{gluon} range

To determine the range of x_{gluon} probed by this measurement, the PYTHIA MPI simulation without GEANT was used to obtain event-by-event x_{gluon} (one or two values per event) and $p_T^{\rm cone}$ (one or two values per event). Figure 5.9 shows x_{gluon} distributions for $p_T^{\rm cone}$ bins. The x_{gluon} values where yield is half maximum are $10^{-1.7} = 0.02$ at the lower side of the "$4 < p_T^{\rm cone} < 5$" distribution and $10^{-0.6} = 0.3$ at the upper side of the "$11 < p_T^{\rm cone} < 12$" distribution. Therefore we adopted a range of $0.02 < x_{gluon} < 0.3$ as the range probed by this measurement, although the definition of the 'range' is obviously not unique.

By way of parenthesis, Figure 5.10 shows Q^2 distributions for $p_T^{\rm cone}$ bins. Q^2 increases on average as $p_T^{\rm cone}$ increases, and this measurement probes a range of $5 < Q^2 < 300$ GeV^2.

5.5.2 χ^2 between measurement and calculation

The measured A_{LL} was compared with the calculated A_{LL}s which assumed various Δg values in order to estimate the constraint of the measured A_{LL} on Δg. The method of evaluating χ^2 between the measured A_{LL} and the calculated A_{LL} is as follows:

1. fix the integral value of $\Delta g(x)$ and fit the parameters of the polarized structure function to the DIS data, where the number of parameters in this fit is practically 11 because the integral of $\Delta g(x)$ is fixed,

2. calculate A_{LL} of jet in each subprocess (qq, qg and qq scatterings),

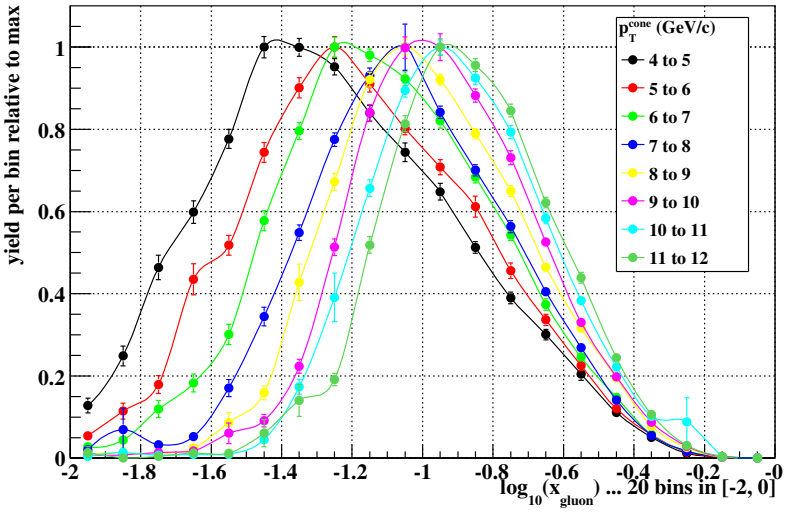

Figure 5.9: The distributions of x_{gluon} in events that include a particle cluster with $4 < p_T^{\text{cone}} < 12$ GeV/c. It has been estimated with the PYTHIA MPI simulation.

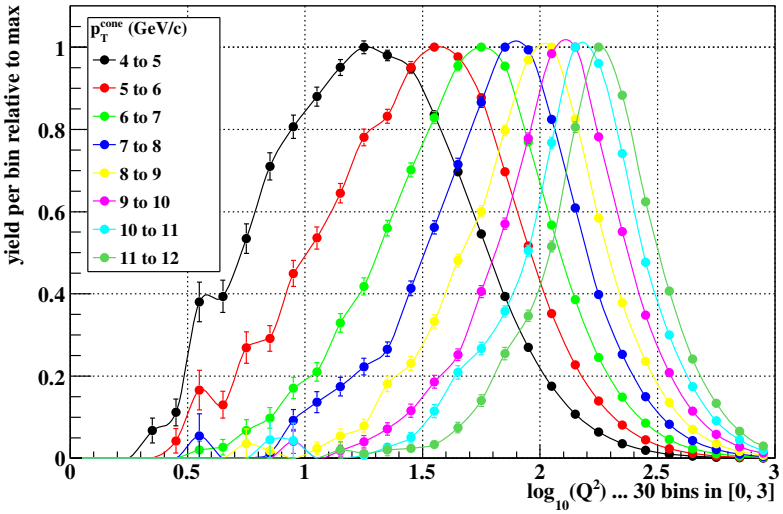

Figure 5.10: The distributions of Q^2 in events that include a particle cluster with $4 < p_T^{\text{cone}} < 12$ GeV/c. It has been estimated with the PYTHIA MPI simulation.

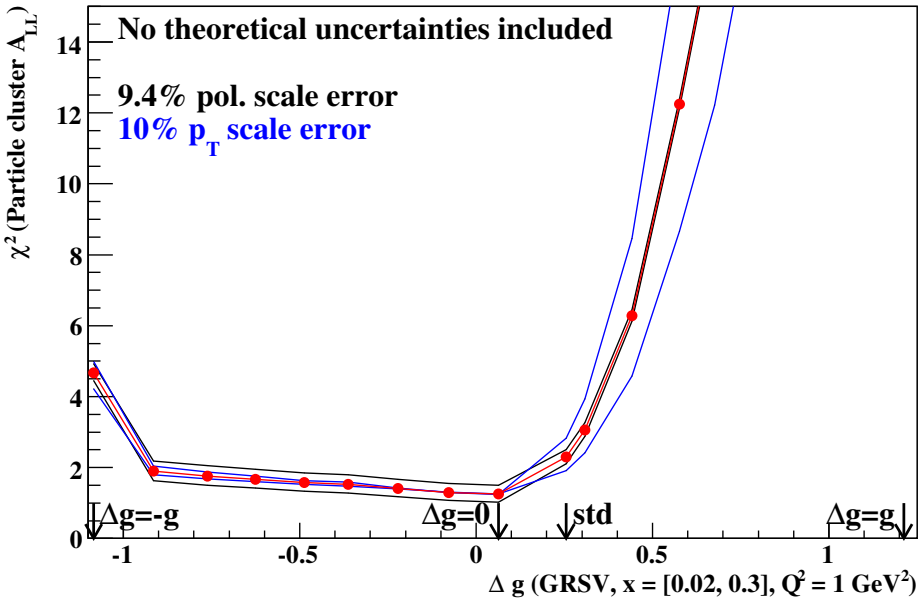

Figure 5.11: χ^2 between the measured A_{LL} and the calculated A_{LL} as a function of the integrated value of $\Delta g(x)$.

3. calculate A_{LL} of particle cluster using the A_{LL} of jet in (3) and the relation between $p_T^{\rm cone}$ and $p_T^{\rm jet}$ evaluated with the PYTHIA+GEANT simulation, and

4. evaluate χ^2 between the 6 data points and each calculated A_{LL} of particle cluster,

where 1 and 2 were provided by W. Vogelsang, and 3 and 4 were performed by myself. This way the χ^2 at different integral values of $\Delta g(x)$ are obtained. The method of calculating A_{LL} is described in Sec. 4.8.3 in detail.

Figure 5.11 shows the χ^2 between the 6 data points and the prediction curves as a function of the integral $\int_{0.02}^{0.3} dx \Delta g(x, Q^2 = 1)$ for each prediction curve. The value of Q^2 ($= 1$ GeV^2) has been arbitrarily chosen in order to show the value of the Δg integral in horizontal axis, and actual Q^2 used in the A_{LL} calculation varies event-by-event.

The minimum of the χ^2 is ~ 1.5 at $\Delta g = 0.07$, namely the GRSV $\Delta g = 0$ input. It is the most probable Δg value and the error limit is where the χ^2 increases from the minimum by 4 at 2σ level or by 9 for 3σ level. Therefore

we obtained

$$-1.1 < \int_{0.02}^{0.3} \Delta g^{GRSV}(x, Q^2 = 1) < 0.4 \quad (2\sigma \text{ level}) \tag{5.1}$$

$$\int_{0.02}^{0.3} \Delta g^{GRSV}(x, Q^2 = 1) < 0.5 \quad (3\sigma \text{ level}) \tag{5.2}$$

It should be noted that the GRSV model contains 12 parameters in total as shown in Eq. 2.43. In the assumptions of the present approach, the parameters in the u, d and antiquark distributions are well fixed with the DIS data. The shape of the gluon distribution (α_g, β_g) are also well fixed with the DIS data. Therefore, the only parameter to be fitted to the p+p collision data is the normalization parameter in $\Delta g(x)$. The correlations of error between the normalization parameter and the shape parameters in $\Delta g(x)$ are not included in the analysis. The effect of the shape parameters is discussed in the subsequent subsection.

5.5.3 Comparison with SIDIS results

Figure 5.12 shows the gluon polarization $\Delta g(x)/g(x)$ measured with the SIDIS experiments and ones calculated with pQCD at $Q^2 = 4$ GeV^2. In the pQCD calculation, $\Delta g(x)$ is one of the four GRSV polarized PDFs and $g(x)$ is the GRV98 unpolarized PDF.

The result of the SIDIS measurements indicates small Δg. The data points which are negative have large errors. It is consistent with the result of the particle cluster A_{LL} measurement. In the SIDIS measurements, the "HERMES (Method II)" and the "COMPASS ($Q^2 < 1$ GeV^2)" have the smallest uncertainty and disfavor both the GRSV $\Delta g = g$ input and the GRSV $\Delta g = -g$ input at a similar statistical significance. The particle cluster A_{LL} disfavors the former strongly but the latter weekly. It is because the particle cluster A_{LL} with the $\Delta g = -g$ input is as nearly small as that with the $\Delta g = 0$ input due to the cancellation between the large positive gg-subprocess A_{LL} and the large negative qg-subprocess A_{LL}.

5.5.4 Systematic uncertainty on theory calculation

The discussion above hasn't taken into account systematic uncertainties on the theory calculation. Particularly the uncertainty due to the assumed functional form is large because the measurement probed the limited range $0.02 < x_{gluon} < 0.3$. The uncertainty hasn't been quantitatively estimated yet, but can be partly discussed by comparing the GRSV parameterization with another parameterization, the GS (Gehrmann and Stirling) parameterization[79].

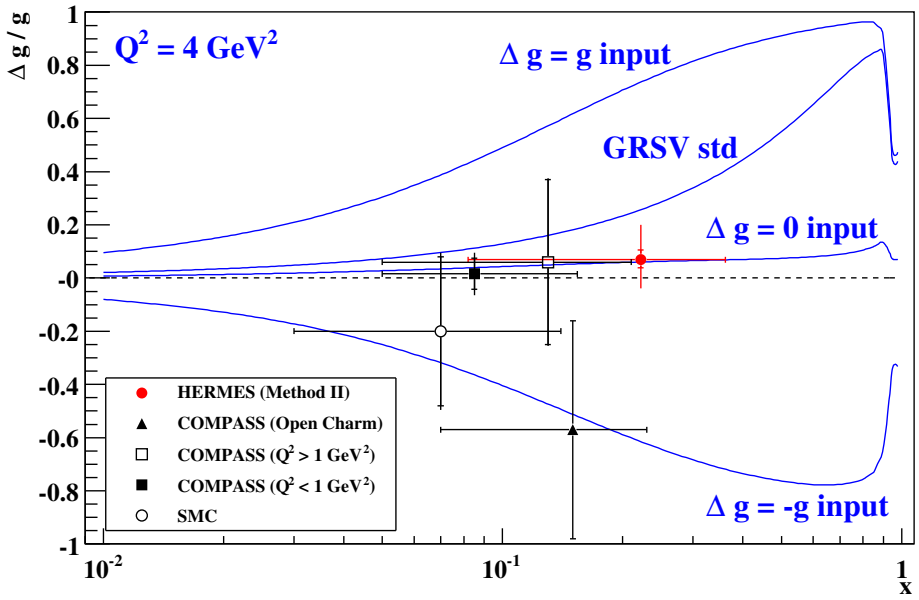

Figure 5.12: Gluon polarization at $Q^2 = 4$ GeV^2, where $\Delta g(x)$ is one of the four GRSV polarized PDFs and $g(x)$ is the GRV98 unpolarized PDF. Data points are identical to those in Fig. 2.10.

In the GS parameterization the PDFs are parameterized in the forms;

$$\begin{aligned}
x\Delta u_v(x, Q^2 = Q_0^2) &= \eta_u A_u x^{a_u}(1-x)^{b_u}(1+\gamma_u x + \rho_u x^{1/2}) \\
x\Delta d_v(x, Q^2 = Q_0^2) &= \eta_d A_d x^{a_d}(1-x)^{b_d}(1+\gamma_d x + \rho_d x^{1/2}) \\
x\Delta \bar{q}(x, Q^2 = Q_0^2) &= \eta_{\bar{q}} A_{\bar{q}} x^{a_{\bar{q}}}(1-x)^{b_{\bar{q}}}(1+\gamma_{\bar{q}} x + \rho_{\bar{q}} x^{1/2}) \\
x\Delta g(x, Q^2 = Q_0^2) &= \eta_g A_g x^{a_g}(1-x)^{b_g}(1+\gamma_g x + \rho_g x^{1/2}) \qquad (5.3)
\end{aligned}$$

where $Q_0^2 = 4$ GeV^2 is the initial scale, and A_f is the normalization factor that is a function of the free parameters (a_f, b_f, γ_f and ρ_f) and ensures that the first moment ($\int_0^1 dx \Delta f(x, Q^2 = Q_0^2)$) is given by n_f. The SU(3)-symmetric antiquark polarization is assumed, $\Delta\bar{q}(x, Q^2) = \Delta\bar{u}(x, Q^2) = \Delta\bar{d}(x, Q^2) = \Delta\bar{s}(x, Q^2)$. The $\Delta g(x, Q^2)$ was very weakly constrained only with DIS data, and thus the parameters in $\Delta g(x, Q^2)$ have been fixed in three ways;

$$\text{GS-A} : a_g = a_{\bar{q}},\ \gamma_g = 0,\ \rho_g = 0 \qquad (5.4)$$

$$\text{GS-B} : a_g = a_{\bar{q}},\ \gamma_g = -1,\ \rho_g = 2 \qquad (5.5)$$

$$\text{GS-C} : a_g = a_{\bar{q}},\ \gamma_g = 0,\ \rho_g = -3 \qquad (5.6)$$

The three scenarios have different functional forms as shown in Fig. 5.13 but have a similar χ^2 in the global fit.

When the GS-C parameterization is assumed, the A_{LL} is almost zero ($|A_{LL}| < 0.2\%$) and is consistent with the measured A_{LL}. It is probably because

$$\int_{0.02}^{0.3} \Delta g^{\text{GS-C}}(x, Q_0^2) \approx 0 \qquad (5.7)$$

The integration range is where the cone measurement probed. It is the same for the GRSV $\Delta g = 0$ input,

$$\int_{0.02}^{0.3} \Delta g^{\text{GRSV } \Delta g=0 \text{ input}}(x, Q_0^2) = 0 \qquad (5.8)$$

But the first moments of these two parameterizations are very different

$$\int_0^1 \Delta g^{\text{GS-C}}(x, Q_0^2) = 1.02 \qquad (5.9)$$

$$\int_0^1 \Delta g^{\text{GRSV } \Delta g=0 \text{ input}}(x, Q_0^2) = 0 \qquad (5.10)$$

because the contribution from small x region, namely at $x = 0.01$ and below, is large in the GS-C parameterization. The shape of the GS-C parameterization has a node at $x \sim 0.1$. The measurement has not quantitatively excluded this possibility yet. Therefore it is concluded that the $\Delta g(x)$ outside of the measured x range has not been constrained well.

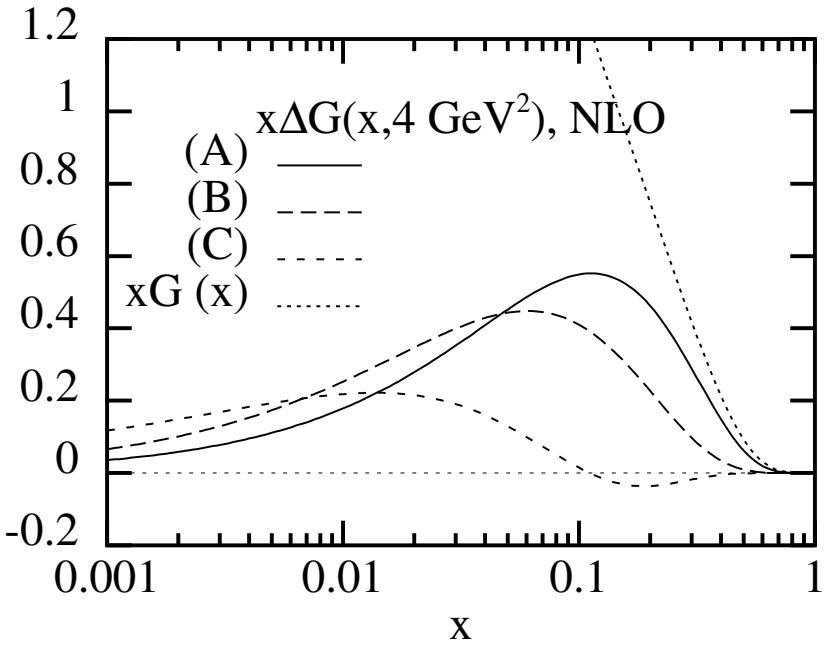

Figure 5.13: $\Delta g(x)$ with the GS NLO parameterization[79].

Chapter 6

Conclusion

In this thesis I presented the new method and result for the study of the gluon spin in the proton using particle clusters from jets in proton-proton collisions.

The contribution of the gluon spin to the proton spin was investigated in detail. The proton spin structure has been studied so far with deep inelastic scattering (DIS) experiments with high-energy lepton beams. In the measurement reported in this thesis, polarized proton-proton collision was used where direct gluon-quark collision can be observed. The method of measuring the particle clusters in the jet production process has been developed, and the first result was presented in this thesis.

The double helicity asymmetry (A_{LL}) of particle clusters from jet production process at a mid-rapidity $|\eta| < 0.35$ in longitudinally polarized proton-proton collision at $\sqrt{s} = 200$ GeV was measured. In 2005 at RHIC the PHENIX experiment took, with the high-energy ($\gtrsim 1.4$ GeV) photon trigger, collision data about 3.8 pb^{-1} in integrated luminosity with average beam polarizations $\langle P \rangle = 49\%$. I have performed the energy calibration of every EMCal module using π^0 invariant mass peak and the development of the high-energy-photon trigger (ERT). Not only the measurement of particle cluster but also all PHENIX measurements at mid-rapidity are based on the calibration and the development.

Photons and charged particles in jets were measured at $|\eta| < 0.35$ and $\Delta\phi = 90^\circ \times 2$ with the EMCal, the DC and the PC of the PHENIX Central Arm. Measured particles were clustered by the seed-cone algorithm with a cone radius $R = 0.3$. The sum of p_T of particles in cone ($p_T^{\rm cone}$) was related to the p_T of original jet ($p_T^{\rm jet}$) with the PYTHIA and GEANT simulation. To confirm the reproducibility of the simulation, the event structures and the cone production rate were measured and compared between the real data and the simulation outputs. The MPI-enhanced PYTHIA well agreed with

the real data in terms of the transverse momentum density as a function of the azimuthal angle from trigger photon and the thrust in the PHENIX Central Arm. Also the cone production rate of the real data agreed with that of the calculation based on the SCA jet cross section and the PYTHIA MPI simulation.

The A_{LL} of particle cluster was measured at $4 < p_T^{\rm cone} < 12$ GeV/c. The main systematic errors are a p_T scale uncertainty of 10% and a beam polarization uncertainty of 9.4%. The x_{gluon} range probed by the measurement of the particle clusters with $4 < p_T^{\rm cone} < 12$ GeV/c are mainly $0.02 < x < 0.3$ according to the simulation study. The measured A_{LL} was compared with the predicted values based on the GRSV parameterization, and the comparison imposed the limit $-1.1 < \int_{0.02}^{0.3} dx \Delta g^{GRSV}(x, Q^2 = 1) < 0.4$ at 2σ level or $\int_{0.02}^{0.3} dx \Delta g^{GRSV}(x, Q^2 = 1) < 0.5$ at 3σ level, and thus excluded large-Δg cases of the GRSV parameterization. This provides an important impact in understanding the gluon spin in the proton because a very large Δg (~ 4) was once theoretically suggested in order to explain the EMC result. This large Δg is not consistent with the present result. The result of the SIDIS $\Delta g(x)/g(x)$ measurements indicates small or even negative Δg, and is consistent with the result of the particle cluster A_{LL} measurement. Due to the uncertainty on the functional form in the theory calculation, the $\Delta g(x)$ outside of the measured x range has not been constrained well.

The new method of A_{LL} measurement with particle clusters which I started and developed provides a powerful tool to investigate the proton spin problem. As the luminosity of RHIC is increasing every year, further strong constraint will be obtained in coming years with this method.

Acknowledgement

I would like to thank Prof. Toshi-Aki Shibata, my supervisor. He demonstrated many interesting and important aspects of the spin physics to me, and provided the opportunity to participate in the PHENIX experiment. His advice throughout my graduate course was indispensable for this thesis.

I am obliged to Dr. Hideto En'yo, the chief researcher of the Radiation Lab at RIKEN, and Dr. Gerry Bunce, the leader of the experimental group in RIKEN BNL Research Center (RBRC), for their supports of my participation in the PHENIX experiment as well as physics discussions on this thesis. Their supports were the foundation of my experimental works and analyses at BNL.

All collaborators in the PHENIX experiment were, of course, essential to carry out such a massive experiment. I am obliged especially to the spokespersons—Dr. William A. Zajc and Dr. Barbara Jacak—, the convenors of the Spin Physics Working Group—Dr. Kiyoshi Tanida, Dr. Sasha Bazilevsky, Dr. Christine Aidala and predecessors—, and the members of the EMCal and ERT groups. They organized all operations necessary for experiments and analyses, and managed my activities. Dr. Yuji Goto, Dr. Yasuyuki Akiba and Dr. Kensuke Okada discussed with me the results of my analyses in depth. They really improved my understandings of the results.

I am grateful to the members of Shibata Lab at Tokyo Institute of Technology for their supports over many years. Particularly, Dr. Yoshiyuki Miyachi, the assistant professor, helped me in physics studies, computings and office works. Mr. Nobuyuki Kamihara, Dr. Takuma Horaguchi and Mr. Kouichi Sakashita helped me in various issues at BNL as well as at Shibata Lab.

I appreciate all smooth and heartful supports by the current and past secretaries at RIKEN, RBRC and Tokyo Institute of Technology. I could efficiently perform this research by the grace of them.

Concerning my daily life, I would thank the following persons. Dr. Yoshinori Fukao, Mr. Manabu Togawa, Mr. Kazuya Aoki and Mr. Seishi Dairaku shared long joyful time with me at the RIKEN Team Apartment inside BNL in addition to research activities. Mr. Johann Sebastian Bach and Mr. Helmut Walcha brought the beauty of eternity and strength to my mind when I

was weary with the paper writing. My parents, Shigetomi and Shizuko, kept encouraging me to perform the research.

I would again express my gratitude to all the persons. I could not have completed this thesis without their thankful supports.

Bibliography

[1] J. Ashman *et al.* [European Muon Collaboration], Phys. Lett. B **206**, 364 (1988).

[2] J. Ashman *et al.* [European Muon Collaboration], Nucl. Phys. B **328**, 1 (1989).

[3] G. Baum *et al.*, Phys. Rev. Lett. **51**, 1135 (1983).

[4] G. Altarelli and G. G. Ross, Phys. Lett. B **212**, 391 (1988).

[5] A. Airapetian *et al.* [HERMES Collaboration], Phys. Rev. D **75**, 012007 (2007) [Erratum-ibid. D **76**, 039901 (2007)] [arXiv:hep-ex/0609039].

[6] A. Adare *et al.* [PHENIX Collaboration], Phys. Rev. D **76**, 051106 (2007) [arXiv:0704.3599 [hep-ex]].

[7] J. D. Bjorken and E. A. Paschos, Phys. Rev. **185**, 1975 (1969).

[8] H. W. Kendall, Rev. Mod. Phys. **63**, 597 (1991).

[9] D. J. Gross and F. Wilczek, Phys. Rev. Lett. **30**, 1343 (1973).

[10] H. D. Politzer, Phys. Rev. Lett. **30**, 1346 (1973).

[11] D. J. Gross and F. Wilczek, Phys. Rev. D **8**, 3633 (1973).

[12] D. J. Gross and F. Wilczek, Phys. Rev. D **9**, 980 (1974).

[13] R. Brock *et al.* [CTEQ Collaboration], Rev. Mod. Phys. **67**, 157 (1995).

[14] W. M. Yao *et al.* [Particle Data Group], J. Phys. G **33**, 1 (2006).

[15] S. Chekanov *et al.* [ZEUS Collaboration], Eur. Phys. J. C **42**, 1 (2005) [arXiv:hep-ph/0503274].

[16] S. Chekanov *et al.* [ZEUS Collaboration], Phys. Rev. D **67**, 012007 (2003) [arXiv:hep-ex/0208023].

[17] A. D. Martin, R. G. Roberts, W. J. Stirling and R. S. Thorne, Eur. Phys. J. C **23**, 73 (2002) [arXiv:hep-ph/0110215].

[18] J. Pumplin, D. R. Stump, J. Huston, H. L. Lai, P. Nadolsky and W. K. Tung, JHEP **0207**, 012 (2002) [arXiv:hep-ph/0201195].

[19] V. N. Gribov and L. N. Lipatov, Sov. J. Nucl. Phys. **15**, 438 (1972) [Yad. Fiz. **15**, 781 (1972)].

[20] G. Altarelli and G. Parisi, Nucl. Phys. B **126**, 298 (1977).

[21] Y. L. Dokshitzer, Sov. Phys. JETP **46**, 641 (1977) [Zh. Eksp. Teor. Fiz. **73**, 1216 (1977)].

[22] M. Gluck, E. Reya and A. Vogt, Eur. Phys. J. C **5**, 461 (1998) [arXiv:hep-ph/9806404].

[23] B. Adeva *et al.* [Spin Muon Collaboration (SMC)], Phys. Lett. B **369**, 93 (1996).

[24] B. Adeva *et al.* [Spin Muon Collaboration], Phys. Lett. B **420**, 180 (1998) [arXiv:hep-ex/9711008].

[25] A. D. Martin, R. G. Roberts, W. J. Stirling and R. S. Thorne, Eur. Phys. J. C **4**, 463 (1998) [arXiv:hep-ph/9803445].

[26] D. J. Gross and C. H. Llewellyn Smith, Nucl. Phys. B **14**, 337 (1969).

[27] S. A. Larin, Phys. Lett. B **334**, 192 (1994) [arXiv:hep-ph/9403383].

[28] W. C. Leung *et al.*, Phys. Lett. B **317**, 655 (1993).

[29] S. L. Adler, Phys. Rev. **143**, 1144 (1966).

[30] D. Allasia *et al.*, Z. Phys. C **28**, 321 (1985).

[31] D. Allasia *et al.* [New Muon Collaboration (NMC)], Phys. Lett. B **249**, 366 (1990).

[32] M. Arneodo *et al.* [New Muon Collaboration], Nucl. Phys. B **487**, 3 (1997) [arXiv:hep-ex/9611022].

[33] A. Baldit *et al.* [NA51 Collaboration], Phys. Lett. B **332**, 244 (1994).

[34] E. A. Hawker *et al.* [FNAL E866/NuSea Collaboration], Phys. Rev. Lett. **80**, 3715 (1998) [arXiv:hep-ex/9803011].

[35] J. Speth and A. W. Thomas, Adv. Nucl. Phys. **24**, 83 (1997).

[36] J. D. Bjorken, Phys. Rev. **148**, 1467 (1966).

[37] P. L. Anthony *et al.* [E155 Collaboration], Phys. Lett. B **493**, 19 (2000) [arXiv:hep-ph/0007248].

[38] J. R. Ellis and R. L. Jaffe, Phys. Rev. D **9**, 1444 (1974) [Erratum-ibid. D **10**, 1669 (1974)].

[39] R. L. Jaffe and A. Manohar, Nucl. Phys. B **337**, 509 (1990).

[40] S. A. Larin, T. van Ritbergen and J. A. M. Vermaseren, Phys. Lett. B **404**, 153 (1997) [arXiv:hep-ph/9702435].

[41] X. D. M. Ji, Phys. Rev. Lett. **78**, 610 (1997) [arXiv:hep-ph/9603249].

[42] X. D. Ji, Phys. Rev. D **55**, 7114 (1997) [arXiv:hep-ph/9609381].

[43] P. Hoodbhoy, X. D. Ji and W. Lu, Phys. Rev. D **59**, 014013 (1999) [arXiv:hep-ph/9804337].

[44] M. Gluck, E. Reya, M. Stratmann and W. Vogelsang, Phys. Rev. D **63**, 094005 (2001) [arXiv:hep-ph/0011215].

[45] J. Bluemlein and H. Bottcher, Nucl. Phys. B **636**, 225 (2002) [arXiv:hep-ph/0203155].

[46] M. Hirai, S. Kumano and N. Saito [Asymmetry Analysis Collaboration], Phys. Rev. D **69**, 054021 (2004) [arXiv:hep-ph/0312112].

[47] A. Airapetian *et al.* [HERMES Collaboration], Phys. Rev. Lett. **84**, 2584 (2000) [arXiv:hep-ex/9907020].

[48] G. Bunce, N. Saito, J. Soffer and W. Vogelsang, Ann. Rev. Nucl. Part. Sci. **50**, 525 (2000) [arXiv:hep-ph/0007218].

[49] N. S. Craigie, K. Hidaka, M. Jacob and F. M. Renard, Phys. Rept. **99**, 69 (1983).

[50] G. Hanson *et al.*, Phys. Rev. Lett. **35**, 1609 (1975).

[51] F. Abe *et al.* [CDF Collaboration], Phys. Rev. D **45**, 2249 (1992).

[52] G. Arnison *et al.* [UA1 Collaboration], Phys. Lett. B **132**, 214 (1983).

[53] J. Muth *et al.*, "Proceedings 1990 Summer Study on High Energy Physics", ed. E. Berger, Singapore: World Scientific, 134 (1992).

[54] G. C. Blazey *et al.*, Proceedings of the Run II QCD and Weak Boson Physics Workshop (hep-ex/0005012)

[55] G. P. Salam and G. Soyez, JHEP **0705**, 086 (2007) [arXiv:0704.0292 [hep-ph]].

[56] SISCone web page, http://projects.hepforge.org/siscone/

[57] F. Aversa, M. Greco, P. Chiappetta and J. P. Guillet, Z. Phys. C **46**, 253 (1990).

[58] B. Jager, M. Stratmann and W. Vogelsang, Phys. Rev. D **70**, 034010 (2004) [arXiv:hep-ph/0404057].

[59] L. W. Anderson, Nucl. Instrum. Meth. **167**, 363 (1979).

[60] A. Zelenski *et al.*, Proceedings of PAC07, 3771 (2007).

[61] S. van der Meer, ISR-PO/68-31, KEK68-64.

[62] M. Bai *et al.*, Phys. Rev. Lett. **96**, 174801 (2006).

[63] E. D. Courant and R. Ruth, BNL Report No. BNL-51270, 1980 (unpublished).

[64] J. Tojo *et al.*, Phys. Rev. Lett. **89**, 052302 (2002) [arXiv:hep-ex/0206057].

[65] H. Okada *et al.*, Phys. Lett. B **638**, 450 (2006) [arXiv:nucl-ex/0502022].

[66] K. Adcox *et al.* [PHENIX Collaboration], Nucl. Instrum. Meth. A **499**, 469 (2003).

[67] A. Bazilevsky *et al.*, Phys. Lett. B **650**, 325 (2007) [arXiv:hep-ex/0610030].

[68] M. Allen *et al.* [PHENIX Collaboration], Nucl. Instrum. Meth. A **499**, 549 (2003).

[69] C. Adler, A. Denisov, E. Garcia, M. J. Murray, H. Strobele and S. White, Nucl. Instrum. Meth. A **470**, 488 (2001) [arXiv:nucl-ex/0008005].

[70] L. Aphecetche *et al.* [PHENIX Collaboration], Nucl. Instrum. Meth. A **499**, 521 (2003).

[71] K. Adcox *et al.* [PHENIX Collaboration], Nucl. Instrum. Meth. A **499**, 489 (2003).

[72] J. T. Mitchell *et al.* [PHENIX Collaboration], Nucl. Instrum. Meth. A **482**, 491 (2002) [arXiv:nucl-ex/0201013].

[73] PYTHIA Webpage, http://www.thep.lu.se/~torbjorn/Pythia.html

[74] CERNLIB Webpage, http://cernlib.web.cern.ch/cernlib/

[75] R. Field, Proc. A1, 34th International Symposium on Multiparticle Dynamics

[76] S. S. Adler *et al.* [PHENIX Collaboration], Phys. Rev. Lett. **91**, 241803 (2003) [arXiv:hep-ex/0304038].

[77] G. Alexander *et al.* [OPAL Collaboration], Phys. Lett. B **265**, 462 (1991).

[78] R. Akers *et al.* [OPAL Collaboration], Z. Phys. C **68**, 179 (1995).

[79] T. Gehrmann and W. J. Stirling, Phys. Rev. D **53**, 6100 (1996) [arXiv:hep-ph/9512406].